Spring 1-1-2012

Characterization and causes of multi-timescale sea level and thermocline depth variability in the tropical southern Indian Ocean

Laurie Leah Trenary
University of Colorado at Boulder, laurie.trenary@colorado.edu

Characterization and causes of multi-timescale sea level and thermocline depth variability in the tropical southern Indian Ocean

by

Laurie Leah Trenary

B.S., Chemical Engineering

Colorado State University, 2000

M.S., Atmospheric Science

Colorado State University, 2003

A thesis submitted to the

Faculty of the Graduate School of the

University of Colorado in partial fulfillment

of the requirement for the degree of

Doctor of Philosophy

Department of Atmospheric and Oceanic Sciences

2012

This thesis entitled:
Characterization and causes of multi-timescale sea level and thermocline depth variability in the tropical southern Indian Ocean
written by Laurie Leah Trenary
has been approved for the Department of Atmospheric and Oceanic Sciences

_____
Dr. Weiqing Han

_____
Dr. Michael Alexander

Date_____

The final copy of this thesis has been examined by the signatories, and we find that both the content and the form meet acceptable presentation standards of scholarly work in the above mentioned discipline.

Trenary, Laurie Leah (Ph.D., Atmospheric and Oceanic Science)

Characterization and causes of multi-timescale sea level and thermocline depth variability in the tropical southern Indian Ocean

Thesis directed by Associate Professor Weiqing Han

In this study a hierarchy of numerical models and a suite of diagnostic numerical experiments are used to characterize the spatial and temporal structure of sea level and thermocline depth variations in the southern Indian Ocean. The key physical processes responsible for driving the multi-timescale variability are then identified. Particular emphasis is placed on the Thermocline Ridge of the Indian Ocean (TRIO), a region in the southwestern tropical Indian Ocean where variations in thermocline depth are suggested to affect sea surface temperature and thus climate.

On seasonal-to-decadal timescales, the key physical processes that contribute to variability of the TRIO are timescale dependent and largely arise from wind forcing acting on the Indian Ocean. Seasonally, variability of the TRIO results from a combination of local Ekman pumping and the arrival of Rossby waves forced by winds east of region. Interannually, variability is associated with westward-propagating Rossby waves forced by the Ekman pumping velocities east of the ridge. Remote oceanic forcing from the Pacific has significant influence on the seasonal and interannual thermocline variability in the eastern basin, but a weak impact in the tropical ocean interior. On decadal timescales, sea level and thermocline depth variability peaks in the southwestern Indian Ocean in both the tropics and subtropics. Prior to the early 1990s, low frequency variations in sea level and thermocline depth in the tropics, can be described as a baroclinic Sverdrup balance, forced by windstress acting on the Indian Ocean. Beginning in the early 90’s, decadal variability of the equatorial Pacific trade winds forces thermocline variations that modify the sea level and thermocline depth across the entire tropical southern Indian Ocean

basin. Farther south, nonlinearities of the flow appear to dominate the low frequency variability in the ocean interior. On multi-decadal timescales, the TRIO has experienced a shoaling trend spanning 1961-2000. This shoaling is consistent with regional enhanced upward Ekman pumping velocity and spin-up of the southern Indian Ocean subtropical cell.

Acknowledgments

This work would not have been possible without the support and guidance of my advisor Dr. Weiqing Han. She has challenged me to think deeply and helped me realize the value of independent thought. With her patience, I have become a better scientist. To my committee members: Dr. Michael Alexander, Dr. Baylor Fox-Kemper, Dr. Jerry Meehl, Dr. Balaji Rajagopalan, and Dr. Jeffrey Weiss, I am grateful to each of you for your willingness to serve on my committee and the time that has been so generously invested in my future.

My family has always been my shelter during the times that I needed it most. While I have gained knowledge from *years* of schooling, I have gained wisdom from all of you. From my mother Dorothy, I have learned to be introspective and from my father Chris the ability to laugh; the former most certainly requires the latter. My sister Chloe has been my biggest champion and is my dearest friend, through you I have moved from cynic to optimistic realism. My brothers Ryan and Josh bring levity to any situation and have taught me that it is always best to not to take yourself too seriously. For all the love and encouragement, this thesis is just as much yours as it is mine.

For years, my friend Victoria has given me unwavering encouragement, thoughtful advice, and has always taken me as I am, thank you. My graduate school cohorts, Rachel, Richard, and Eric, have helped to make the ups and downs all that much better, thank you for the conversations, the laughs, and the hugs.

Contents

Chapter

Tables

Table

Figures

Figure

Chapter 1

Introduction

The unique geometry of the Indian Ocean has profound implications on the ocean circulation and regional and global climate. Unlike the two other major ocean basins, the Pacific and Atlantic, flows within the Indian Ocean are restricted to latitudes south of 25^{o}N. The presence of the Asian continent prevents the northward export of heat. The excess heat gain in tropics is necessarily exported southward across the equator by the wind driven cross-equatorial cell (Schoenfield and Schott, 2006). Further, the intrusion of the Asian landmass into the lower latitudes, leads to differential heating of the land-sea surface, in turn producing large seasonal changes in the winds and precipitation. Also, the rising branch of the equatorial Walker circulation is anchored to the maritime continent; consequently there are no steady equatorial easterlies in the Indian Ocean. As a result, climatological equatorial upwelling along the eastern boundary is absent in the Indian Ocean; rather upwelling occurs along the northwest coast of Somalia and Oman, the tip of India, and in the open ocean in the southwestern Indian Ocean. Lastly, the Indian Ocean is the only ocean to have a gappy eastern boundary. Accordingly, variations originating in the Pacific can transmit through the Indonesian archipelago and contribute to variability within the Indian Ocean.

One of the principal goals of this work is to quantify the timescale dependent impact of remote forcing from the Pacific on sea level and thermocline depth variability of the southern Indian Ocean. In the following sections I will describe the mean circulation of the Indian Ocean (section 1.1) and the corresponding distribution of sea level and thermocline depth (section 1.2). Once the mean state has been described, we will discuss the sea level and thermocline depth

variability of the Indian Ocean sorted by time scale (section 1.3). Lastly, we will consider the theoretical arguments and simple modeling studies which document transmission of energy from the Pacific to Indian Ocean (section 1.7).

1.1 The mean circulation of the Indian Ocean

The ocean circulation north of 10^{o}S is dominated by the strong seasonality of atmospheric flows. The Somali current, the mid-basin monsoon currents, and the west/east India coastal currents experience a complete reversal from January-February (Northeast monsoon; Fig. 1.1) to July-August (Southwest monsoon, Fig. 1.2). During the northeast monsoon (or winter monsoon), the Somali current flows southward, converging with the East Africa Coastal Current (EACC), and supplying the waters for the South Equatorial Counter Current (SECC). The East Indian Ocean Coastal Current (EICC) flows southward, feeding the northeast monsoon current, which turns northward into the Arabian Sea and flows along the western coast of India. During the southwest monsoon, the Somali current flows northward and is feed by the South Equatorial Current (SEC). The coastal current on the western coast of India now moves southward, feeding the southwest monsoon current, which moves northward along eastern coast of India. During the transition months, May and October, westerlies develop along the equator and the flow is characterized by the strong eastward flowing Wyrtki jets (Wyrtki, 1971). The complete reversal of the currents is accomplished by remotely and locally forced tropical and coastally trapped waves.

The ocean circulation south of 10^{o}S is fairly steady, with little year-to-year variations. The circulation of the tropical southern Indian Ocean is characterized by the westward SEC, which is primarily feed by waters from the Indonesian Throughflow (ITF). Near the eastern coast

of Madagascar, the SEC splits, forming the North East Madagascar Current (NEMC) and the South East Madagascar Current (SEMC). The NEMC feeds both the northward flowing EACC and the southward flow within the Mozambique Channel. Instability of the SEMC produces eddies that propagate westward toward the east coast of Africa. Additionally, it is believed that some portion of the SEMC retroflects and feeds the northeast flowing South Indian Counter Current, which extends across the subtropics from 22°S-26°S. The western boundary current is made up of a complex set of currents, including the Agulhas Current, the Mozambique Current eddies, and the SEMC. In turn the Agulhas current system feeds the upper branch of the Atlantic meridional overturning circulation and is a key component of the global ocean circulation (Neal et al. 2011 and references therein).

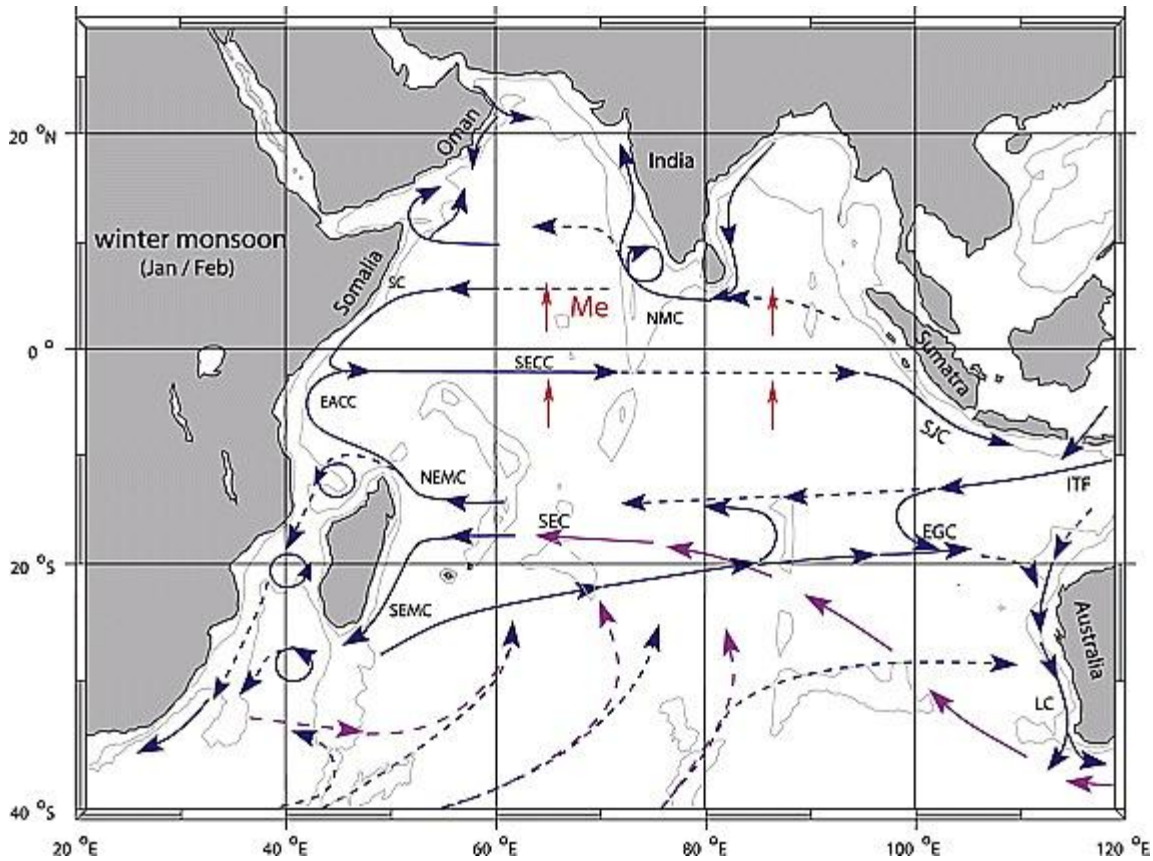

Figure 1.1: Schematic diagram showing the direction of the mean currents during the winter monsoon. The labeled currents are the South Equatorial Current (SEC), the Northeast and Southeast Madagascar Currents (NEMC and SEMC), East African Coastal Current (EACC), Somali Current (SC), Northeast Monsoon Current (NMC), South Java Current (SJC), East Gyral Current (EGC), and the Leeuwin Current (LC). The subsurface current of the

supergyre is shown in magenta. The red vectors (Me) show the direction of Ekman transport and the Indonesian Throughflow is indicated by ITF. Image adapted from Schott et al. 2009.

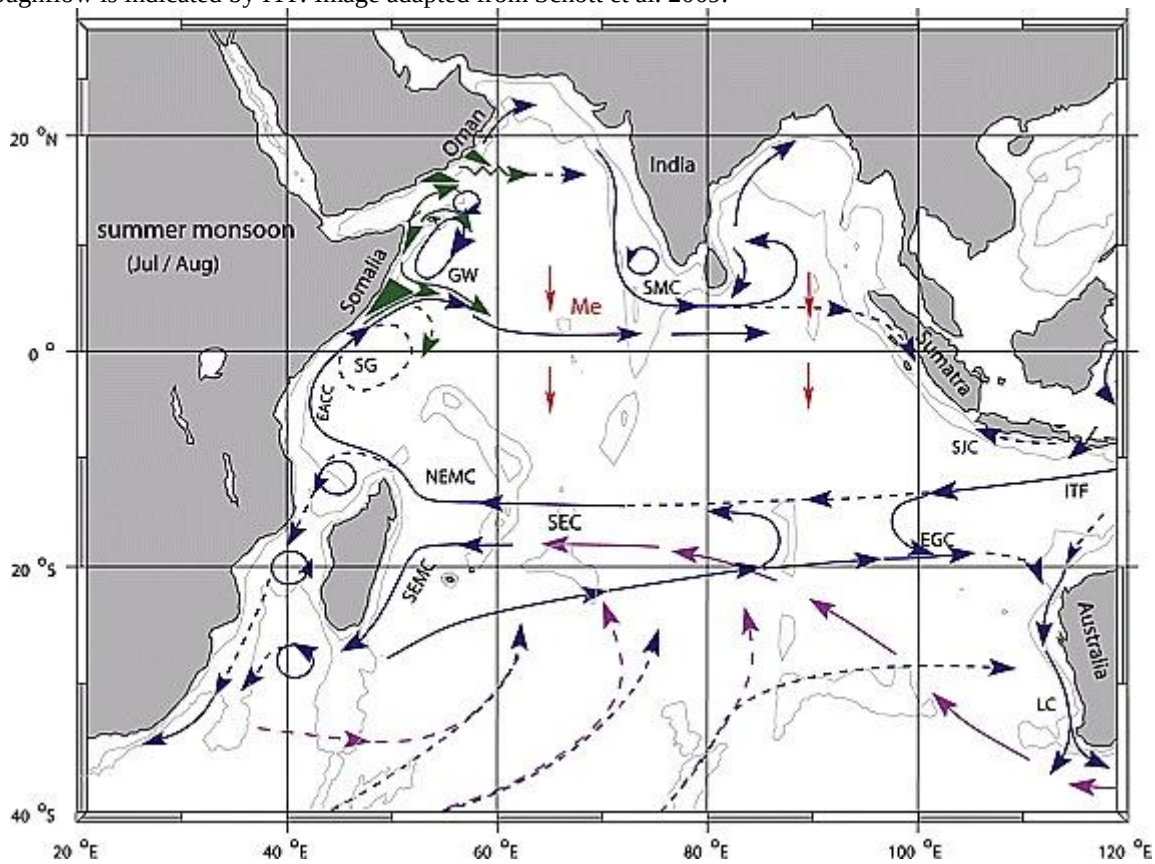

Figure 1.2: Same as in Fig. 1.1, but for the summer monsoon. Currents present during the summer monsoon include the Southeast Monsoon Current (SMC), Southern Gyre (SG) and Great Whirl (GW) and associated upwelling wedges (green shades). All other current systems are identically labeled as in Fig. 1. Image adapted from Schott et al. 2009.

1.2 Climatological structure of sea level and thermocline depth

Sea level and thermocline depth are dynamically linked to the windstress convergence and divergence of the upper ocean Ekman transport. The Ekman transport is the net wind driven transport of the upper ocean and is given by $\vec{M}_E = \left(\frac{1}{\rho}\right)\hat{k}\times\left(\frac{\vec{\tau}}{f}\right)$, where ρ is the density of sea water, $\hat{k}$ is the unit vector in the vertical, $\vec{\tau}$ is the windstress vector , and f is the Coriolis parameter. The divergence of the Ekman transport, $-\nabla\bullet\vec{M}_E = \left(\frac{1}{\rho}\right)\hat{k}\bullet\nabla\times\left(\frac{\vec{\tau}}{f}\right)$, is equivalently the Ekman pumping velocity (w_e). Negative w_e is associated with convergence of the Ekman

transport ($\bar{M}_e$) and sea level rise and thermocline deepening. The converse is true for positive w_e. Winds blowing parallel to continental boundaries similarly force a shoaling/deepening of the thermocline through convergence/divergence of the wind driven transport.

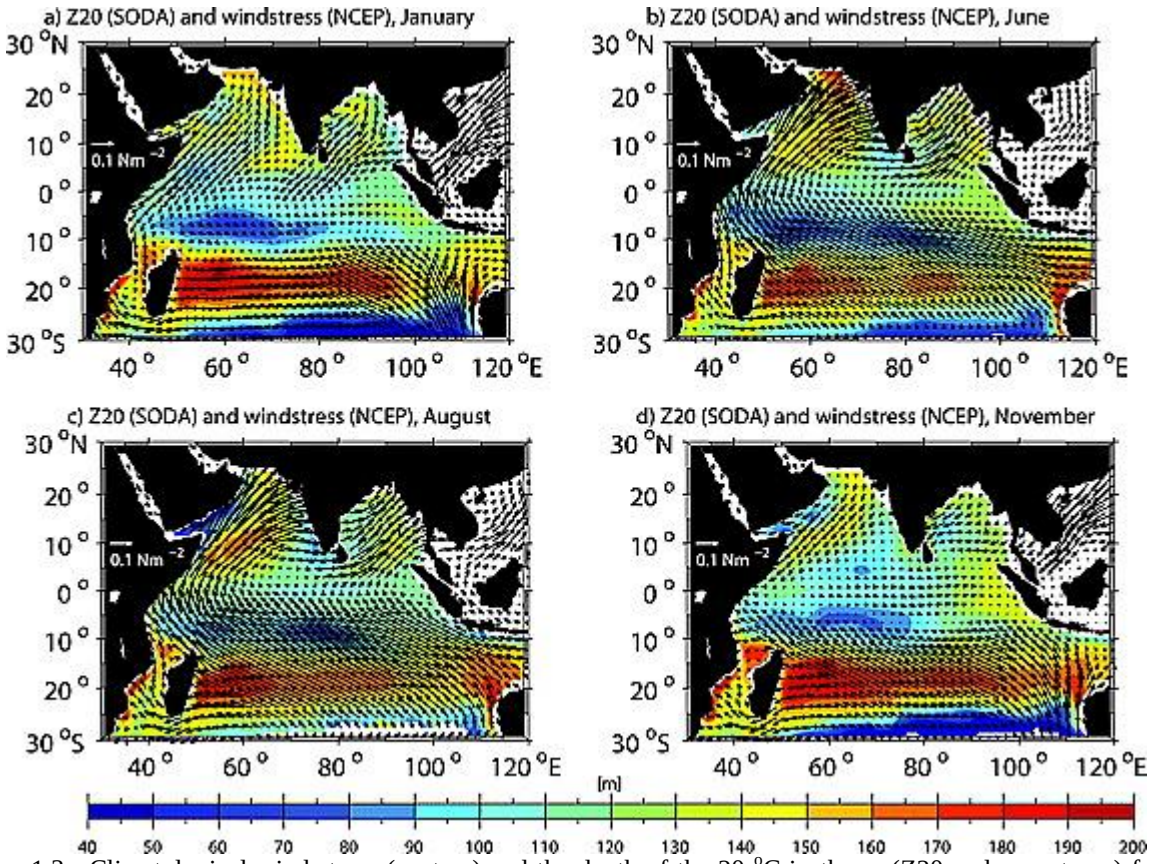

Figure 1.3: Climatological wind stress (vectors) and the depth of the 20 °C isotherm (Z20, color contours) for (a) January, (b) June, (c) August, and (d) November. The wind stress data comes from the National Centers for Environmental Prediction (NCEP) for the period 1990-1998. The Z20 data is from the Simple Ocean Data Assimilation product and spans the period 1992-2001. Image taken from Schott et al. 2009.

In the southern hemisphere, the climatological depth of the 20°C isotherm (Fig. 1.3), a common measure of thermocline depth, identifies regions of persistent shoaling (5°S-12°S) and deepening (south of 10°S). The region characterized by a relatively shallow thermocline is commonly referred to as the Thermocline Ridge of the Indian Ocean (TRIO), and owes its existence to the overlying mean negative wind stress curl associated with the northward

weakening of the southeasterly trades (Fig. 1.3; McCreary et al. 1993). Farther south, the perpetually deep thermocline is maintained by positive wind stress curl and is associated with the subtropical gyre. During boreal summer, alongshore winds force upwelling along the Java/Sumatra coasts, a process that is important for the Indian Ocean Dipole (IOD; Webster et al. 1999, Saji et al. 1999).

Climatically, thermocline depth variations are most relevant in regions of upwelling, where vertical displacement of the thermocline may profoundly impact sea surface temperature (SST). In the Indian Ocean, SST variability is linked to thermocline depth in the open ocean upwelling zone (TRIO; 5^{o}S-12^{o}S) and off the Sumatran coast. Given the potential for strong dynamic coupling between thermocline depth and SST in TRIO, this study will primarily focus on understanding the cause(s) of thermocline depth variability in this region.

1.3 Sea level and thermocline depth variability of the southern Indian Ocean

Dynamically, linear off equatorial thermocline and sea level variability is caused by local divergence of the Ekman transport (i.e. w_e) and propagation of remotely forced Rossby waves. Generally, the Rossby waves may be forced by windstress curl imposed upon the open ocean, or may radiate from the eastern boundary. In the southern Indian Ocean, the presence of a low latitude gappy boundary to the east allows for an energy flux between the tropical Pacific and southern Indian Ocean. When non-linear dynamics are retained, thermocline depth variability may also result from baroclinic or barotropic instabilities. Below we will review observations and modeling studies which document the structure and causes of intraseasonal-to-multi-decadal sea level and thermocline depth variations in the southern Indian Ocean.

1.3.1 Intraseasonal variability

On intraseaonal timescales, large amplitude sea level and thermocline depth variability exists in various regions of the Indian Ocean. Strong variability off the Sumatran coast is related to the poleward propagation of equatorial Kelvin waves forced by tropical zonal winds (Sprintall et al. 1999; Han 2005; Drushka et al. 2010; Schiller et al. 2010; Zhou and Murtugudde 2010). In the TRIO region, the westward-propagating intraseasonal Rossby waves forced by intraseasonal winds east of region are suggested to affect the sea surface height (SSH) and SST (Han et al. 2007). In the southeast tropical Indian Ocean, large amplitude intraseasonal variability has been attributed to both baroclinic (Feng and Wijffels 2002) and mixed baroclinic and barotropic (Yu and Potemra 2006; Ogata and Masumoto 2010; Ogata and Masumoto 2011) instabilities of the SEC. Oceanic instabilities are also believed to be important in causing intraseasonal variability near the Indian Ocean western boundary region (e.g., Kindle and Thompson 1989; Woodberry et al. 1989; Tsai et al. 1992; Jochum and Murtugudde 2005; Han et al. 2007).

1.3.2 Seasonal and interannual variability

On interannual and seasonal timescales, sea level and thermocline depth variability in the southern Indian Ocean has largely been attributed to Rossby wave propagation (e.g., Woodberry et al. 1989; Périgaud and Delecluse 1992, 1993; Matsumoto and Meyers 1998; Yang et al. 1998). While some studies suggest that the Rossby waves are caused by thermocline anomalies along the eastern Indian Ocean boundary (Périgaud and Delecluse 1992), others indicate that the waves are forced in the open ocean by windstress curl (e.g., Woodberry et al. 1989; Matsumoto and Meyers 1998; Yang et al. 1998; Birol and Morrow 2001; Wang et al. 2001; Rao and Behera 2005). In a recent modeling study, Tozuka et al. (2010) suggests that interannual thermocline

variability of the TRIO is driven by the combination of local Ekman pumping over the region and the arrival of Rossby waves. Origins of the Rossby waves, however, are not discussed in detail. On seasonal timescales, oscillations of the TRIO region thermocline depth are no longer seen to be primarily associated with the arrival of Rossby waves. Rather, the strong semi-annual winds over the northern portion of the TRIO region are important in forcing the thermocline variability (Hermes and Reason 2008, 2009; Yokoi et al. 2008).

1.3.3 Decadal and multi-decadal variability

To date, there are very few studies which have focused on the decadal variability in the Indian Ocean, and much of what is known about the low frequency variations come from SST records. Analysis of observations and coupled climate model solutions reveal a global scale ENSO-like decadal variability in SST that shows heavy loading over the Indian Ocean basin (Meehl et al. 1998). Decadal variations in SST have been linked to low-frequency variations in the amplitude of the Indian Ocean Dipole (Tozuka et al. 2007) and thermocline depth (Ashok et al. 2004). During the era of satellite altimetry data (1993-2006), coherent decadal trends in sea level have been documented over much of the much of the tropical Indo-Pacific basin (Lee and McPhaden 2008; Feng et al. 2011). Observations shows a drop in sea level in the tropical southwestern Indian Ocean accompanied by rising sea level in the eastern Indian Ocean for 1993-2000. The sign of the trend in SSH reverses during 2000-2006. Decadal changes in sea level in the interior of the Indian Ocean are linked to large scale changes in the regional windstress curl, while changes in tropical Pacific trade winds are linked to sea level variations in the eastern Indian Ocean (Lee and McPhaden 2008).

Multi-decadal changes in the vertical structure of temperature in the Indian Ocean shows

a complex pattern of near-surface warming accompanied by thermocline-cooling in the tropical southern Indian Ocean (Han et al. 2006, Alory et al. 2007, Trenary and Han 2008). This intricate pattern of temperature variability is consistent with the distinct spatial patterns of sea level trends found over the Indian Ocean since the 1960s, where sea levels fall in the southwestern Indian Ocean is accompanied by a rise elsewhere (Han et al. 2011). It's suggested that changes in the Indian Ocean Walker Circulation associated with warming of the Indo-Pacific warm pool is the primary forcing responsible for this pattern of sea level change (Han et al. 2011). The changing winds manifest as strengthening of the westerlies in the tropical Indian Ocean and the southeasterly trades in the subtropics, the result is an increase in upward Ekman pumping over the southwestern tropical Indian Ocean (Han et al. 2006) and is consistent with spin-up of the southern subtropical cell (Trenary and Han 2008). The aforementioned processes attribute the subsurface cooling to regionally wind forced shoaling of the thermocline. Long term subsurface temperature variability has also been attributed to changes in the Indonesian Throughflow transport (Wainwright et al. 2008) and energy flux from the Pacific, via the ITF, in the form of long Rossby waves (Alory et al. 2007, Cai et al. 2008). Proxy reconstructions have also linked decadal variability of western Indian Ocean SST to decadal variations in the Pacific (Cole et al. 2002, Cobb et al. 2001). Decadal modulation of the character of ENSO, i.e. the meridional extent and amplitude of the events, has also been linked to transmission efficiencies of Pacific Rossby wave into the southern Indian Ocean, such that transmission efficiencies increased post-1980 (Shi et al. 2007). Changes in the transmission efficiency in turn provide a potential for the Pacific to exert a multi-decadal control on the variability in the southern Indian Ocean via the oceanic bridge.

1.4 The oceanic bridge and Indian Ocean variability

The ITF serves as a low latitude connection between the Indian and Pacific Ocean basins, allowing for interbasin exchange of heat, freshwater, and mass. It has also been suggested that potential energy is transferred between the basins in the form of Rossby waves transmitted via the throughflow region. Consequently, variability of Indian Ocean surface and subsurface temperature, may not be solely the result of atmospheric forcing, but may also be influenced by the "oceanic bridge", such that variability in the Pacific is transmitted to the southern Indian Ocean through wave prorogation and transport changes associated with the ITF.

1.4.1 Rossby wave transmission

In addition to the Indian Ocean origins, thermocline variability of the southern Indian Ocean is influenced in part by the transmission of remote wave energy from the Pacific. Upon reaching the western boundary, a portion of the energy from the Pacific equatorial Rossby waves is transmitted through the passage and travels poleward along the western Australian continent. Equatorward of the turning latitude (McCreary and Kundu 1987), the coastally trapped signals can radiate westward as Rossby waves into the interior southern Indian Ocean (Fig. 1.4). The portion of wave energy that can transmit from the Pacific into the southern Indian Ocean appears to be timescale dependent.

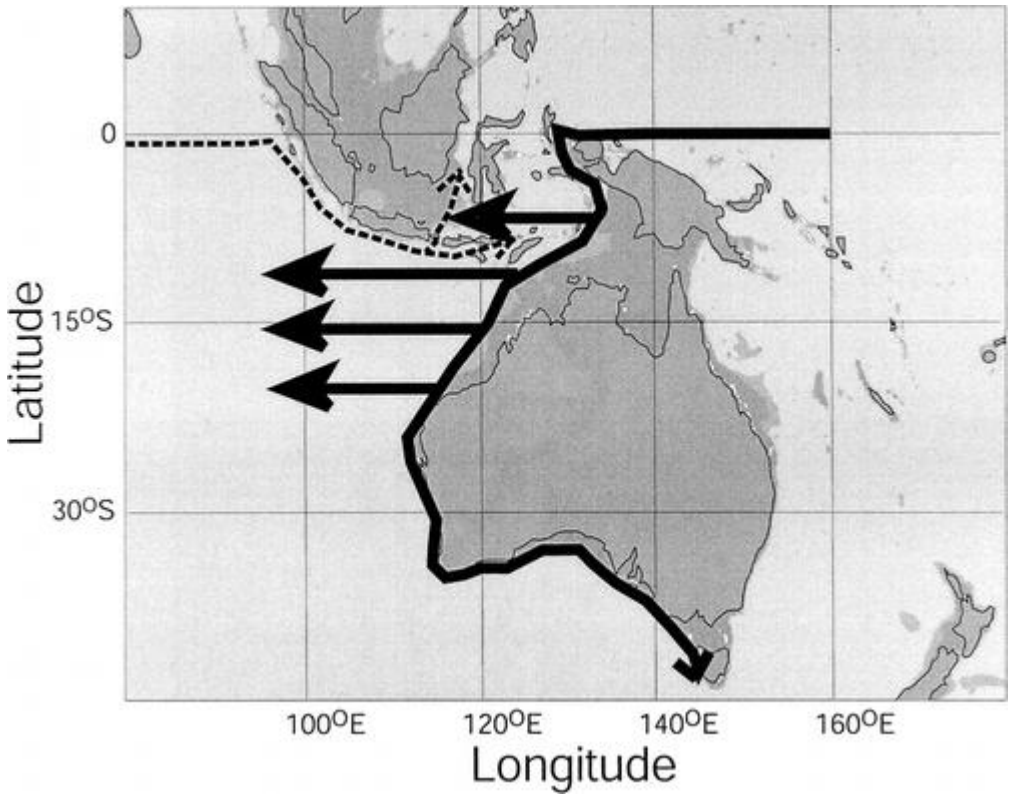

Figure 1.4: Schematic diagram showing the confluence of the tropical Pacific and Indian Ocean wave guides. The black solid lines represent the wave pathway for anomalies of Pacific origin traveling down the coast of Australia and radiating westward into the Banda Sea and the southern Indian Ocean. The dotted line represents the Indian Ocean wave guide and shows the transmission of signals into the internal seas through the Lombok and Ombai passages. Image adapted from Wijffels and Meyers (2004).

Early analytical studies that focus on reflection efficiencies from a straight meridional wall found reflection to be strongly dependent upon the frequency of the incipient Rossby wave (Clarke 1983). The reflected energy flux decreases with increasing frequency, and the reflected high frequency wave energy becomes trapped to the western boundary in the form of short Rossby waves. Inclusion of a gappy western Pacific boundary leads to a theoretical estimate of 5-10% interannual energy flux into the southern Indian Ocean (Clarke 1991; Spall and Pedlosky 2005). Consistent with the theoretical results, model solutions of Potemra (2001) show that interannual Rossby waves in the equatorial Pacific are primarily reflected at the western boundary, with a small percentage of energy propagating into the Indian Ocean. On seasonal timescales, however, there is a significant amount of energy flux that enters the Indian Ocean,

accounting for about 80% of the annual Rossby wave energy near the northwestern coast of Australia and 10% offshore. At periods shorter than 60 days, essentially no energy propagates into the Indian Ocean.

1.4.2 Numerical modeling studies with an open and closed Indonesian passage

Results from ocean model experiments with open and closed Indonesian passages suggest that sea level and thermocline depth of the Indian Ocean are most impacted by the ITF south of 12^{o}S and along the west coast of Australia (Hirst and Godfrey 1993; Verschell et al. 1995; Schneider 1998; Lee et al. 2002; McCreary et al. 2007). Verschell et al. (1995) concluded that at periods longer than ½ year, the presence of the ITF enhances southern Indian Ocean variability through transmission of Rossby waves. In contrast, Lee et al. (2002) found that thermocline variability was larger as a result of shallower thermocline when the Indonesian passage was closed. Observational studies also show that interannual variability of sea level and thermocline depth in the equatorial Pacific can affect the ITF region and the western coast of Australia (Meyers 1996; Wijffels and Meyers 2004). Aside from wave transmission, variability of the southern Indian Ocean thermocline can also be affected by temperature and salinity advection via the ITF.

1.5 Present research goals

This study intends to bridge the gap in our understanding of the relative roles of local versus remote oceanic forcing in driving sea level and thermocline depth variability of the southern Indian Ocean. Previous studies point to the existence of transmitted signals from the Pacific in the eastern Indian Ocean, but the extent to which the remote forcing causes or interacts with locally forced variations is unclear. To this end, diagnostic model experiments will be

performed and systematically analyzed for the purpose of quantification of local verses remote oceanic forcing on intraseasonal-to-decadal variations of sea level and thermocline depth of the southern Indian Ocean. Specifically, variability of the Pacific Ocean will be removed by setting the forcing over the basin to a fixed mean. Further, experiments will be performed using a hierarchy of models, including a forced ocean general circulation model (OGCM) and a linear continuously stratified ocean model. The dynamics captured in the 'simplest' model are driven solely by the winds, while the more complex model captures nonlinearities of the flow and responds to all surface forcing. To this end, the goals of this thesis are to use diagnostic numerical experiments to isolate the effects and impacts of remotely forced variability via the oceanic bridge on the intraseasonal, seasonal, interannual, and decadal variability within the southern Indian Ocean, and secondly to determine the role of long term wind changes on the thermocline structure of the southern Indian Ocean. As noted above, this region of Indian Ocean is important climatically because SSTs over the thermocline ridge and off the coast of Sumatra are linked to the displacement of the thermocline.

The questions that this study will address are as follows:

(1)What are the key physical mechanisms driving sea level and thermocline depth variability in the tropical southern Indian Ocean on intraseasonal, seasonal, and interannual timescales? Is the dynamical response of the ocean timescale dependent? What is the relative role of Indian versus Pacific oceanic forcing on the strength of the ITF?

(2)Does remote forcing from the Pacific, via the oceanic bridge, enhance, diminish, or have no effect on variability in the southern Indian Ocean? If so, what are the spatial and temporal characteristic of the remote Pacific forcing?

(3)There is a pronounced decadal signal superimposed on the multi-decadal cooling trend of subsurface temperature in the southern Indian Ocean. What are the relative contributions of regional atmospheric wind forcing and remote oceanic forcing in driving subsurface temperature variations?

(4)What is the contribution of long-term changes in local wind forcing to the observed subsurface cooling trend of the Indian Ocean and what physical process describe the multi-decadal ocean response?

This work is presented as follows:

Chapter 2: Describes the models and datasets analyzed as part of this study. To demonstrate the validity of the model solutions, results are presented which compare model results with observations. The model-data comparison is conducted for the timescales of interest for this study. Experiment design is also discussed in this section.

Chapter 3: The spatial patterns characterizing intraseasonal-to-interannual sea level and thermocline depth variability are described and the timescale dependent evolution of the anomalies discussed. The causes(s) of variability and the impact of remote forcing from the Pacific are presented and sorted by timescale. The relative roles of Indian versus Pacific control on the strength of ITF are also discussed.

Chapter 4: The spatial-temporal characteristics of decadal scale sea level and thermocline depth variability are described and the forcing responsible for the variability discussed.

Chapter 5: Defines the pattern of multi-decadal trends in the upper ocean thermal structure and relates the changes to thermocline movement. A physically consistent mechanism connecting long-term changes in regional winds to subsurface temperature variability is also discussed.

Chapter 6: Provides a summary of general conclusions and discussion of future work.

Chapter 2

Numerical ocean models, experiment design, datasets, and validation

Observational evidence in combination with numerical modeling results suggest that energy is fluxed from the Pacific to the Indian Ocean via the Indonesian passage. Quantification the impacts of remote forcing from the Pacific on sea level and thermocline depth variability in the ocean interior, necessarily requires the use of numerical models. Model selection for this study was largely determined by the model's ability to simultaneously capture flow within the vicinity of complex topography (i.e., the Indonesian passage) and fluid motion within the thermocline. The appropriate model would, therefore employ a vertical coordinate that exploits a terrain following coordinate near topography and an isopyncal coordinate in the ocean interior. One such model is the Hybrid Coordinate Ocean Model (HYCOM); it poses a hybrid vertical coordinate and the capability to simulate fluid motion near coasts and in the interior of the ocean. Moreover, it is of interest to understand the degree to which the ocean response is captured by linear wind-driven processes, as such a linear ocean model is also used. Relative to the other major ocean basins, the Indian Ocean is grossly under-sampled. In order to gain any understanding of the cause(s) of long-term variability within the basin, requires numerical modeling experiments. In what follows, the numerical models used as part of this study are described (sections 2.1.1-2.1.2) and the experiment design explained (section 2.1.3). This is followed by descriptions of observations and reanalysis data (section 2.3) used for model/data comparison (section 2.4).

2.1 Models

2.1.1 The Hybrid Coordinate Ocean Model (HYCOM)

HYCOM is a primitive equation ocean general circulation model consisting of five prognostic equations: two horizontal momentum equations, a mass continuity equation (layer thickness tendency equation), and two conservation equations (temperature and salinity or salinity and density). The model employs a hybrid coordinate in the vertical, which is isopycnic in the open ocean, transitioning to a z-coordinate in the weakly stratified mixed layer, and a terrain following sigma coordinate in very shallow waters. The prognostic equations expressed for a Cartesian horizontal coordinate (*x*,*y*) and a general vertical coordinate *s*, are given as follows:

$$\begin{aligned}&\frac{\partial \vec{v}}{\partial t_s}+\nabla_s\frac{\vec{v}^2}{2}+(\zeta+f)\hat{k}\times\vec{v}+\left(\dot{s}\frac{\partial p}{\partial s}\right)\frac{\partial \vec{v}}{\partial p}+\nabla_s M-p\nabla_s\alpha\\&=g\frac{\partial \tau}{\partial p}+\left(\frac{\partial p}{\partial s}\right)^{-1}\nabla_s\bullet\left(\vec{v}\frac{\partial p}{\partial s}\nabla_s\vec{v}\right)\end{aligned} \tag{2.1}$$

$$\frac{\partial}{\partial t_s}\left(\frac{\partial p}{\partial s}\right)+\nabla_s\bullet\left(\vec{v}\frac{\partial p}{\partial s}\right)+\frac{\partial}{\partial s}\left(\dot{s}\frac{\partial p}{\partial s}\right)=0 \tag{2.2}$$

$$\frac{\partial}{\partial t_s}\left(\frac{\partial p}{\partial s}\theta\right)+\nabla_s\bullet\left(\vec{v}\frac{\partial p}{\partial s}\theta\right)+\frac{\partial}{\partial s}\left(\dot{s}\frac{\partial p}{\partial s}\theta\right)=\nabla_s\bullet\left(\nu\frac{\partial p}{\partial s}\nabla_s\theta\right)+H_\theta \tag{2.3}$$

In the above, $\vec{v}$ is the horizontal velocity vector, $\zeta=\frac{\partial v}{\partial x_s}-\frac{\partial u}{\partial y_s}$ is the relative vorticity, *f* is the Coriolis parameter, $\hat{k}$ is the unit vector in the vertical, *p* is pressure, θ is any thermodynamic variable in the model, $M\equiv gz+p\alpha$ is the Montgomery potential, $\alpha=\rho_{pot}^{-1}$ is the potential specific volume, *g* acceleration due to gravity, τ is the wind and/or bottom drag induced vertical

shear vector, ν is the variable eddy viscosity/diffusivity, H_θ is the sum of the diabatic source term, including diapyncnal mixing. The prognostic equations are integrated in time using a Mode-splitting technique, in which the barotropic response is computed separately from the slower baroclinic response. The prognostic equations are accompanied by a set of diagnostic equations, including: the hydrostatic equation $\left(\frac{\partial M}{\partial \alpha} = p\right)$, an equation of state relating temperature, salinity and pressure to the specific potential volume, and an equation that prescribes the vertical mass flux through a surface *s.*

The K-Profile Parameterization (KPP) mixing scheme is employed in the boundary layer (Large et al. 1994). In the interior, diapycnal mixing coefficient is set to $(1x10^{-7}\ m^2\ s^{-2})N^{-1}$, where N is the buoyancy frequency. The diapycnal mixing values averaged for 5^oS-20^oS of the Indian Ocean range from 2.1 $cm^2\ s^{-1}$ at 2038 m depth to 0.066 $cm^2\ s^{-1}$ at 128 m depth, and are within the range of observational estimates (Kunze et al. 2006). Isopycnal diffusivity and viscosity values are formulated as $u_d\Delta x$, where Δx is the local horizontal mesh size and u_d is 0.03 m s^{-1} for momentum and 0.015 m s^{-1} for temperature and salinity. In regions of large shear, isopycnal viscosity is set proportional to the product of mesh-size squared and total deformation (Bleck 2002).

2.1.1.1 Model grid

In the horizontal, HYCOM employs a staggered Arakawa-C grid (Fig. 2.1). The horizontal grid is staggered such that variables *M, p, H,T,* and *S* are placed at the center of the grid and velocity/vorticity are located at the west/east and north/south edges of the cell. Basically, the properties at the center of the grid are evaluated between points where the currents are available.

The vertical coordinate is general and varies from an isopycnal coordinate in the open

ocean, transitioning to a terrain following sigma coordinate shallow waters, to a z-level coordinate in near-surface well-mixed waters. For details please refer to Bleck et al. 2002.

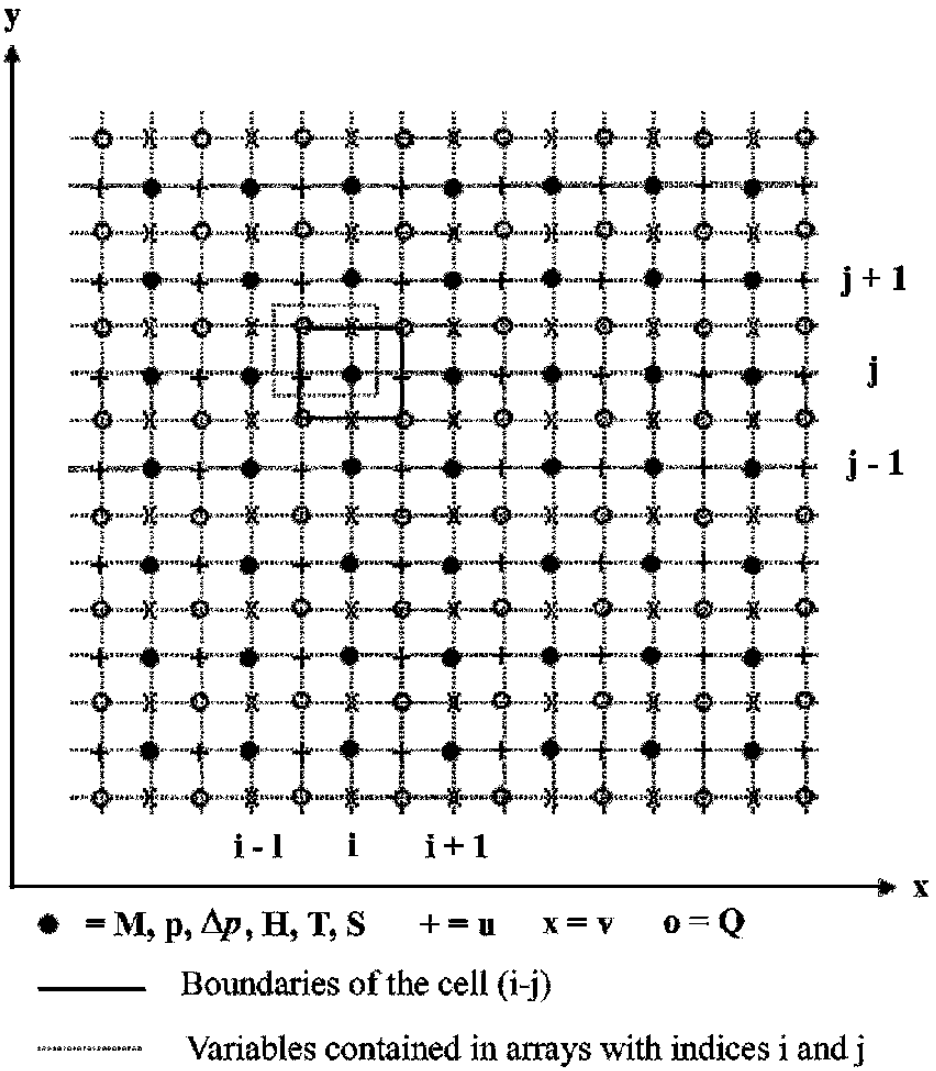

Figure 2.1: Arakawa C-grid used in horizontal discretization of variables in HYCOM. Image adapted from the HYCOM user manual (www.hycom.org).

2.1.1.2 Atmosphere and ocean exchange

Exchange at the air-sea interface includes radiative exchange, turbulent latent and sensible heat transfer, and the transfer of mechanical energy by the winds. Standard bulk formulas are used to compute the upper ocean heat balance and turbulent transfer of momentum follows the classic diffusion model.

2.1.2 Linear Ocean Model (LOM)

A linear continuously stratified ocean model is used to study the wind-driven response of the Indo-Pacific basin. This version of the LOM has been previously applied to a number of different studies of the Indian Ocean (McCreary et al. 1996; Han et al. 2004; Han 2005), as well as the Atlantic (Han et al. 2008). The model is linearized about a background density state, yielding the following set of governing equations:

$$u_t - fv + p_x = F + (\nu u_z)_z + \nu_h \nabla^2 u \tag{2.4}$$

$$v_t + fu + p_y = G + (\nu v_z)_z + \nu_h \nabla^2 v \tag{2.5}$$

$$u_x + v_y + w_z = 0 \tag{2.6}$$

$$\rho_t - \frac{N_b}{g} w = (\kappa \upsilon_z)_z \tag{2.7}$$

$$p_z = -\rho g \tag{2.8}$$

where, *u*, *v*, and *w* are the zonal, meridional and vertical velocity anomalies, respectively. *p* and ρ are the pressure and density anomalies, *g* is the acceleration due to gravity, *f* is the Coriolis parameter, ν and κ are coefficients of eddy viscosity and eddy diffusivity. Lastly, the terms *F* and *G* represent the zonal and meridional components of wind forcing. The eddy coefficients are assumed to be inversely proportional to the square of Brunt-Vaisala frequency (N^2_b), such that: $\nu = \frac{A}{N_b^2}$ $\kappa = \frac{A}{N_b^2}$ and *A* is a constant equal to 0.00013 cm^2 s^{-3}. The choice of the vertical mixing coefficients ensures that the solutions to the governing equations can be expressed in terms of vertical modes. The system (2.5-2.8) can expressed by the eigenfunctions $\psi_n(z)$, which satisfy

the differential equation $\psi_{nz} = \frac{N_b^2}{c_n^2}\int_{-D}^{0}\psi_n dz$, subject to the boundary condition $\frac{1}{c_n^2}\int_{-D}^{0}\psi_n dz = 0$.

Solutions to the equations (2.5-2.8) are:

$$u_n = \sum_{n=1}^{\infty} u_n\psi_n, \qquad v_n = \sum_{n=1}^{\infty} v_n\psi_n, \qquad p_n = \sum_{n=1}^{\infty} p_n\psi_n, \tag{2.9}$$

Where the expansion coefficients are functions of *x,y,* and *t* only. The equations governing the expansion coefficients are:

$$u_{nt} - fv_n + p_{nx} = F_n - \frac{A}{c_n^2}u_n + \nu_h\nabla^2 u_n \tag{2.10}$$

$$v_{nt} + fu_n + p_{ny} = G_n - \frac{A}{c_n^2}v_n + \nu_h\nabla^2 v_n \tag{2.11}$$

$$p_{nt} + u_n + v_n = -\frac{A}{c_n^2}\frac{p_n}{c_n^2} \tag{2.12}$$

The wind stress enters as a body force and acts on each mode as follows:

$$F_n = \frac{\tau^x(x,y,t)}{\int_{-D}^{0}\psi_n^2 dz}, \quad G_n = \frac{\tau^y(x,y,t)}{\int_{-D}^{0}\psi_n^2 dz} \tag{2.13}$$

Details of the LOM are discussed extensively in McCreary (1985).

2.1.3 POP-Hindcast

Simulations were constructed using the ocean component of the Community Climate System model (CCSM3) and were made available through the National Center of Atmospheric Research (NCAR). The ocean model is based on POP version 1.4.3 created at Los Alamos National laboratories. The model was configured with a zonal resolution of 1.12 ^{o} and variable meridional scale. The meridional resolution is ~0.26^{o} near the equator and increases to 0.53^{o} north of 30^{o}. The model has a z coordinate, where depth ranges from 5m to 5375m, the vertical

resolution is greatest in the upper levels of the ocean and decreasing with depth. The model is forced by the National Center for Environmental Prediction (NCEP) atmospheric reanalysis from 1958-2000. The observational dataset was based on reanalysis data of winds, air temperature, and specific humidity, supplemented by satellite observations of cloud cover, surface insolation, and precipitation. Long-term monthly climatologies of radiation fluxes and precipitation were used during periods when satellite data was not available. Air sea fluxes are calculated from the data using standard bulk formulas and model SSTs. The model is spun up over four 43-yr forcing cycles using NCEP reanalysis data. The last 43 years of post processed annual mean data were used for analysis (Doney et al, 2007).

2.2 Model configuration and experiment design

2.2.1 HYCOM

HYCOM is configured to the Indo-Pacific basin with 0.3°x0.3° horizontal grids, 20 vertical layers and realistic bottom topography with 2°x2° smoothing. The model domain extends zonally from 30°E to 290°E and meridionally from 55°S to 55°N (Fig. 2.2a). Near the southern and northern non-continental boundaries, sponge layers of 5° are applied to relax model temperature and salinity fields to climatology (Levitus and Boyer 1994; Levitus et al. 1994), and no-slip boundary conditions are applied along continental boundaries. Initial runs were carried out using a 0.5°x0.5° horizontal resolution and 22 vertical layers. Results from this coarser resolution run are used to study the long-term trends of the Indian Ocean.

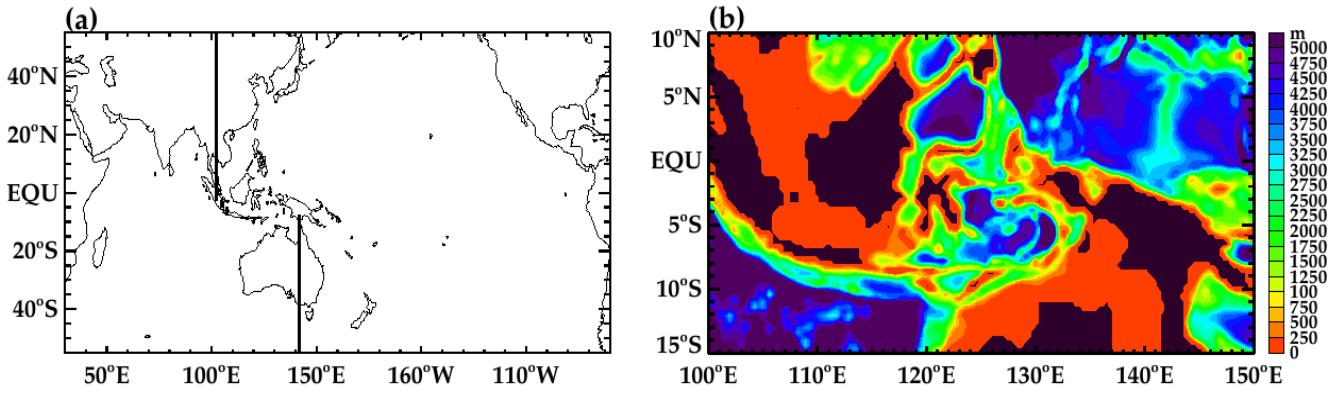

Figure 2.2: Basin map for HYCOM experiments. In experiment HYCOM-INDOPAC, the entire basin is forced by ERA40 reanalysis fields. In experiment HYCOM-IND, regions east of the vertical lines are forced by the 1958-2001 mean fields. Forcing fields near the vertical lines are smoothed by interpolating the ERA40 fields from 2.5°x2.5° grids to 1/3°x1/3° HYCOM grids. (b) Topography of the Indonesian passage used in HYCOM experiments. A 2°x2° topography smoothing is applied, and landmasses of the model are shown in black.

2.2.2 LOM

The LOM is configured for the Indo-Pacific basin (30°E - 290°E, 45°S-45°N) with the same 0.3°x0.3° resolution as HYCOM. This version of the LOM has been previously applied to a number of different studies of the Indian Ocean (McCreary et al. 1996; Han et al. 2004; Han 2005; Han et al. 2010) and the Atlantic (Han et al. 2008). The model equations are linearized about a state of rest and background stratification is calculated from the Levitus temperature and salinity (Levitus and Boyer 1994; Levitus et al. 1994) averaged over the Indo-Pacific basin from 20°S-20°N. The model has a flat ocean bottom, with all straits and islands being represented as vertical walls. This restriction is necessary for the LOM solutions to be represented as the sum of a set of vertical normal modes. The sum of the first 15 modes is well converged and thus is used to represent the total SSH. The northern and southern boundaries are closed and a damping is applied in a 5° band near the non-continental boundaries to reduce zonal velocities to zero. No-slip boundary conditions are applied along continental boundaries.

2.2.3 Forcing fields

The 0.3°x0.3° horizontal resolution version of HYCOM is spun–up from a state of rest for 30 years, using the Comprehensive Ocean-Atmosphere Dataset (COADS) monthly climatology dataset. Restarting from the spun-up run, HYCOM is integrated forward in time using 3-day-mean European Centre for Medium-Range Weather Forecasts (ECMWF) Re-Analysis (ERA-40) forcing fields, including winds, precipitation, air temperature, specific humidity, shortwave and longwave radiation, for 1958-2001. The coarser version with 0.5°x0.5° horizontal resolution is spun-up for 20 years using the same forcing, and similarly integrated forward in time using the ERA-40 fields.

To allow for comparisons between HYCOM solutions and the best available observations of the ITF and satellite observed sea level trends, the HYCOM experiment is extended for the 2000-2008 period. The extended run is initialized by the model output of January 1st, 2000 from the HYCOM-INDOPAC experiment, and integrated forward in time using 3-day-mean QuikSCAT winds, NCEP I air temperature and specific humidity (Kalnay et al. 1996), and Climate Prediction Center (CPC) Merged Analysis of Precipitation (CMAP) pentad data (Xie and Arkin 1996), which is interpolated to a 3-day-mean resolution. Net long and shortwave radiative fluxes are obtained from the International Satellite Cloud Climatology Project flux data (ISCCP-FD; Zhang et al. 2004). Our analyses focus primarily on the 1970-2001 period. The solutions obtained from the extended run for the period of 2004-2006 are used to compare the model ITF transport and hydrographic properties with the INSTANT and Argo observations, respectively. Model sea level trends from the 2000-2008 periods are compared with satellite altimetry data.

2.2.4 Experiment design

To isolate the contribution of remote forcing from the Pacific, two parallel experiments are performed using HYCOM. In the first, the model is forced by ERA40 fields from 1958 to 2001 over the entire Indo-Pacific basin. This solution is complete and includes the effects of both the Indian Ocean and Pacific forcing, and we refer to this experiment as HYCOM-INDOPAC. In the second experiment, which is referred to hereafter as HYCOM-IND, the forcing fields over the Indian Ocean are allowed to evolve as in HYCOM-INDOPAC, while the forcing over the Pacific is fixed to the 1958-2001 mean (see Fig. 2.2). This solution excludes the Indian Ocean variability that results from Pacific forcing, and primarily estimates the effects of Indian Ocean forcing on the variability of sea level and thermocline. The difference solution, (INDOPAC – IND), measures the influence of the Pacific forcing, and we refer to this solution as HYCOM-DIFF.

As for HYCOM, the LOM is spun up for 30 years using COADS monthly wind-stress climatology. Restarting from year 30, the model is integrated forward for the period 1958-2001 using ERA40 wind stress. Similarly, experiments LOM-INDOPAC and LOM-IND are performed from 1958 to 2001. These experiments will help us to identify the role played by wind-driven, linear wave dynamics versus oceanic instabilities due to nonlinearity of the oceanic system.

Experiment Name	***Forcing***	***Resolution***
INDOPAC* (1961-2001)	3-day-mean over Indian and Pacific Basin: ERA-40: Winds, specific humidity, air temperature, precipitation, net shortwave and longwave radiation	Horizontal: 0.3^{o}x0.3^{o} Vertical: 20 layers
INDOPAC-CR (1961-2001)	3-day-mean over Indian and Pacific Basin: ERA-40: Winds, specific humidity, air temperature, precipitation, net shortwave and longwave radiation	Horizontal: 0.5^{o}x0.5^{o} Vertical: 22 layers
INDOPAC (2000-2008)	3-day-mean over Indian and Pacific Basin: NCEP: Specific humidity, air temperature: CMAP: Precipitation ISCCP: Net shortwave and longwave radiation QuikScat: Winds	Horizontal: 0.3^{o}x0.3^{o} Vertical: 20 layers
IND* (1961-2001)	3-day-mean over Indian, Pacific Basin forced by 1961-2001 mean: ERA-40: Winds, specific humidity, air temperature, precipitation, net shortwave and longwave radiation	Horizontal: 0.3^{o}x0.3^{o} Vertical: 20 layers
IND (2000-2008)	3-day-mean over Indian, Pacific Basin forced by 2000-2008 mean: NCEP: Specific humidity, air temperature: CMAP: Precipitation ISCCP: Net shortwave and longwave radiation QuikScat: Winds	Horizontal: 0.3^{o}x0.3^{o} Vertical: 20 layers
Climatology (29-50)	3-day climatology over Indian Ocean: COADS: Winds, specific humidity, air temperature, precipitation, net shortwave and longwave radiation	Horizontal: $0..25^{o}$x$0..25^{o}$ Vertical: 30 layers

Table 2.1: Summary of the HYCOM experiments: forcing, resolution, and duration. The * indicates model configurations that were also used for the LOM.

2.3 Data

2.3.1 Satellite altimetry

To detect sea level variability and to validate HYCOM solutions, SSH anomalies (SSHA) are obtained from the merged satellite product based on two satellites Jason-2/Envisat, Jason-1/Envisat or Topex/Poseidon/ERS, which is the "Reference" version with data quality homogeneous in time. The merged product is produced by the French Archiving, Validation, and Interpretation of Satellite Oceanographic data (AVISO) project using the mapping method of Ducet et al. (2000). The SSHA data are interpolated onto a global grid of 1/3° resolution, archived weekly, and computed relative to a 7-yr mean from January 1993 to December 1999.

2.3.2 SODA-POP

Thermocline depth, which are represented by the depth of 20°C isotherm (D20), and SSH data derived from the Simple Ocean Data Assimilation – Parallel Ocean Program (SODA-POP) version 2.0.2 (Carton and Giese 2008) are also analyzed and compared with HYCOM results. SODA-POP is a global ocean retrospective analysis which uses output from the numerical model POP as a first guess of the ocean state and assimilates observations every 10 days (Carton and Giese 2008). The assimilated data includes historical archives of hydrological profiles, ship intake measurements, moored observations, and satellite remotely-sensed SST. Sea level data are not assimilated; rather it is calculated prognostically using a linearized continuity equation. Model corrections are based on error estimates contained within the model and error associated with differences between the model forecast and observations. These corrections are introduced incrementally every time step to ensure that geostrophy is maintained. It should be noted that there are limited observations in the southern Indian Ocean, and therefore the results are strongly constrained by the model performance. Nevertheless, SODA-POP provides a

measure of the subsurface variability. The output is in monthly averaged form and mapped onto a uniform 0.5° × 0.5° × 40-level grids. The model is forced by daily wind stresses and heat fluxes from ERA40 reanalysis from 1 January 1958 to 31 December 2001. Extended SODA-POP (version 2.0.4) solutions for the period 2000-2007 are also used. SODA-POP version 2.0.4 is identically configured to version 2.02, with the exception that QuikSCAT winds are used to force the model and erroneous Argo data have been corrected.

2.3.3 INSTANT

Exchange between the Pacific and Indian Ocean in HYCOM is validated against the ITF estimated from the International Nusantara STratification ANd Transport (INSTANT) observations. It is only recently that multi-year measurements of the ITF transports at each of the major ITF passages (Lombok Strait, Ombai Strait and Timor Passage) have been collected simultaneously. The INSTANT field program began in August 2003 and ended December 2006, and provides the most comprehensive dataset of the multi-timescale properties and transport of the ITF to date (Sprintall et al. 2004, 2009). The observed ITF data are daily from January 11, 2004 to December 5, 2006. Here, the transport is computed as the sum of the total depth transport through the Lombok, Ombai, and Timor passages.

2.3.4 Argo

To validate HYCOM's ability to simulate the variability of the ITF water properties, a time series is constructed for the mean upper ocean monthly salinity and temperature fields and averaged over the (100^{o}E-120^{o}E, 9^{o}S-20^{o}S) region near the ITF entrance. Identical spatial and temporal criteria are used to construct a time series from Argo profiles. Both the observed and modeled temperature and salinity time series are demeaned relative to 2004-2006. While there is some intrusion of the South Indian Central Water (Wijffels et al. 2002) at the southern boundary

of this region, the region effectively captures the mixture of ITF water masses, and meanwhile allows for inclusion of a sufficient number of observations. Given that the ITF water is mainly advected into the Indian Ocean in the thermocline (Gordon et al. 1999; Fieux et al. 1996; Wijffels et al. 2002), the mean of the upper 500m is chosen for the model/data comparison.

2.3.5 WOD05

Annual mean temperature observations obtained from the World Ocean Database 2005 (WOD05) are used in evaluating the model performance in simulating decadal temperature variations in the Indian Ocean. The 5-year mean (pentadal) gridded data is used for comparison of the long term trends in the HYCOM model for the period 1960-2000. WOD05, an oceanographic objective analysis dataset uses an optimal interpolation scheme to grid historical records of temperature, salinity, dissolved oxygen, and dissolved inorganic nutrients. Historical observations include temperature profiles from bottle samples, Mechanical Bathythermographs (MBT), ship deployed conductivity-temperature-depth (CTD), expendable Bathythermograph (XBT), profiling floats, moored and drifting buoys, gliders, and undulating oceanographic recorder. XBT profile drop-rates errors have been corrected in this dataset. All data are vertically interpolated to standard depths level and $1^{o}x1^{o}$ resolution in the horizontal.

2.4 Model/data comparison

2.4.1 Sea level and thermocline depth

The realism of the simulated SSHA is assessed by comparing the distribution of the standard deviation of SSHAs with altimeter data (Figs. 2.3a and 2.3b). The model captures all large scale features shown in the data, including the large amplitude variability in the south tropical Indian Ocean ($5^{o}S$-$15^{o}S$), off the coasts of southern Sumatra and Java, in the Somali current region, and along the Indian coasts. Notable variability also occurs along the north and

west coasts of Australia, which accompanies a region of low variability immediately off the coasts. The model, however, systematically underestimates the amplitudes of variability throughout the Indian Ocean basin. This basin-wide underestimation may result, at least partly, from errors in the ERA40 forcing fields. For example, assimilation of satellite data since the late 1970s improves the ERA40 surface wind fields over the south tropical Indian Ocean from 1979 to 2001 (Brodeau et al. 2009). The wind and therefore wind-driven SSH variability may be underestimated especially for the period prior to 1979. In addition, HYCOM has only 20 vertical layers, which may not be sufficient to accurately represent the oceanic stratification and thus contribute to the systematic SSH underestimation.

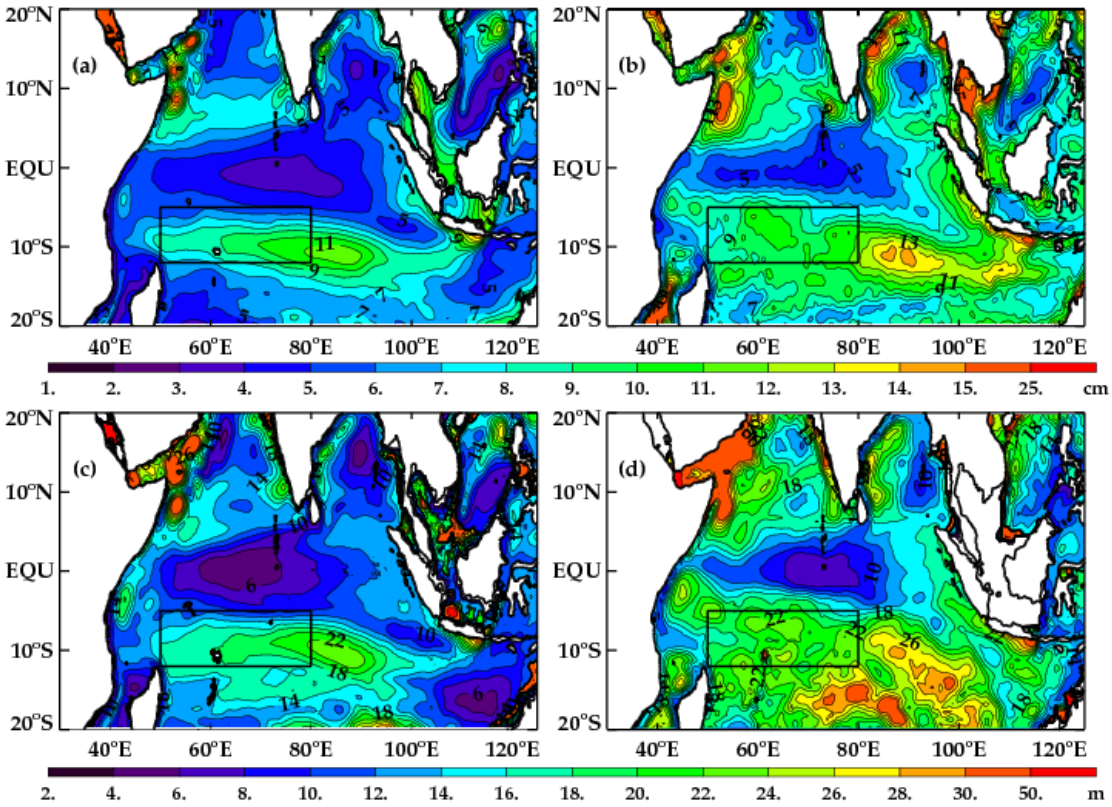

Figure 2.3: (a) Standard deviation (STD) of SSHA (cm) from HYCOM-INDOPAC experiment computed from the 3-day output for the period 1993-2001. The pattern of variability includes contributions from intraseasonal, seasonal and interannual SSHAs, which are the demeaned and detrended 3-day mean HYCOM SSH. (b) Same as (a) but for AVISO weekly SSHA. (c) STD of HYCOM-INDOPAC D20A (m) computed from the monthly-mean temperature field for the same period. The pattern of variability comprises seasonal and interannual variability. (d) Same as (c) but for SODA-POP D20A. The box-enclosed region is 50°E-80°E, 5°S-12°S and denotes the TRIO region.

Model/data differences also exist in resolving some detailed structures of SSHA. For example, the modeled SSHA is more zonal in the south tropical Indian Ocean and weaker in amplitude comparing with satellite observations (Figs. 2.3a and 2.3b). Altimeter data show larger amplitudes of SSHA associated with the bifurcation of the South Equatorial Current in the southwest Indian Ocean, which extends westward to 40^{o}E at 5^{o}S and southwestward toward Madagascar. These regions, together with the Mozambique Channel and the region of enhanced variability near 12^{o}S, 110^{o}E, are associated with significant eddy activity (Schott et al. 1988; Kindle and Thompson 1989; Feng and Wijffels 2002; Yu and Potemra 2006; Zhou et al. 2008; Ogata and Matsumoto 2010; Ogata and Matsumoto 2011). Given the relatively coarse resolution of our model (coarse resolution eddy resolving models, at a minimum, employ a 0.25^{o} horizontal resolution), it is not surprising that our results underestimate the amplitude of variability in regions of high eddy activity.

The spatial pattern associated with the thermocline variability, which is measured by the D20 anomaly (D20A), is consistent with that of SSHA (Compare Figs. 2.3a and 2.3c). This is because in the tropical oceans, SSH variability generally mirrors that of the thermocline (e.g., Fu 2001). Both HYCOM (Fig. 2.3c) and SODA-POP (Fig. 2.3d) consistently capture the regions of enhanced variability detected by SSHA. Near 15^{o}S and 80^{o}E, large amplitude variability is present in SODA-POP D20A, but is not shown in either the HYCOM solution or altimetry data. This is likely a bias in the SODA-POP product in under-sampled regions.

Quantitatively, the modeled and observed monthly SSHAs, which includes both the seasonal cycle and interannual variability, in the TRIO region (Fig. 2.3, box) are in good agreement, with a correlation of 0.88 for HYCOM and AVISO SSHA during 1993-2001, and 0.77 for HYCOM and SODA-POP during 1970-2001 (Fig. 2.4a). The correlation between

HYCOM and SODA-POP D20A is 0.83 (not shown). After the seasonal cycle is removed, the correlation coefficients for interannual SSHA between HYCOM and AVISO (Fig. 2.4b) and HYCOM and SODA-POP D20A (not shown) remain virtually unchanged. Seasonal and interannual SSH variability in the TRIO region is simulated reasonably well when only the wind driven linear response is considered (Figs. 2.4a-2.4b, black dashed lines), with a correlation of 0.78 between HYCOM and LOM SSHA. The thermocline anomalies are strongly correlated with SSHA (Figs. 2.4c-2.4d), with a high SSH corresponding to a deepened thermocline. This indicates that SSHA can serve as a good proxy for thermocline variability in the region. Note that the spatial averaging for the TRIO region smoothes out the point-to-point differences between the model and observations, and thus we are comparing the large scale signals.

Because HYCOM outputs have a 3-day interval whereas AVISO data are weekly, intraseasonal variability is only qualitatively verified by comparing horizontal patterns of variability, which are computed as the standard deviation of the 28-105-day bandpass filtered SSHA using the Lanczos digital filter (Duchon 1979). The HYCOM solution and AVISO data show similar regions of enhanced intraseasonal variability, such as the tropical southern Indian Ocean between 10°S-15°S, the coasts of Sumatra and Java, the Somali coast, Mozambique Channel and to a lesser degree, the tropical southern Indian Ocean between 2°S-6°S. The SSHA amplitudes, however, are systematically underestimated by HYCOM, as are its seasonal and interannual components.

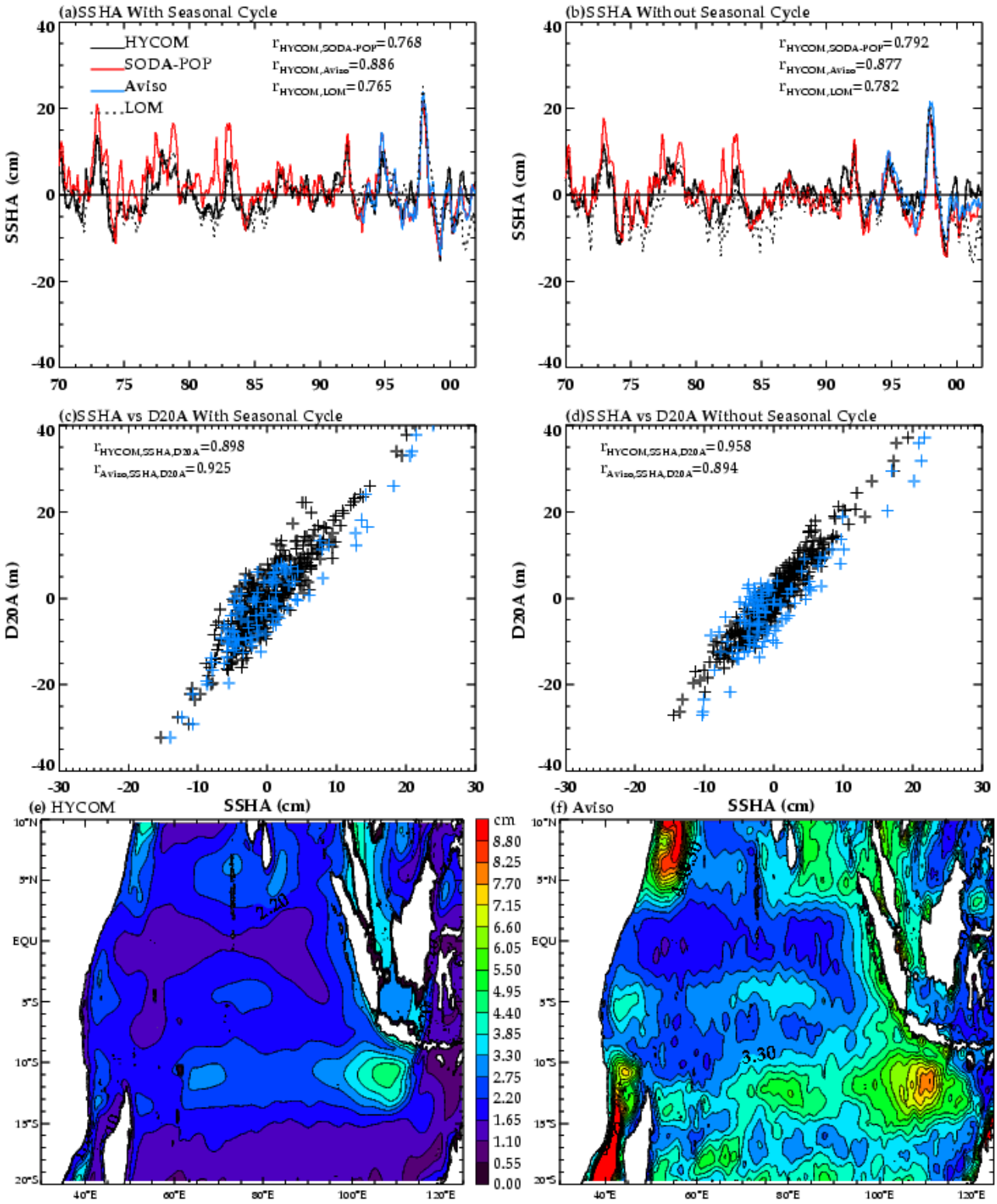

Figure 2.4: (a) Time series of monthly SSHA (cm) averaged in the TRIO region (boxed region of Figure 2) with the seasonal cycle retained from HYCOM-INDOPAC (black), SODA-POP (red), and LOM (black-dashed) for 1970-2001 and AVISO (blue) for 1993-2001. All anomalies are computed relative to the 1993-1999 mean. (b) Same as (a) but for monthly SSHA with the first three harmonics of the seasonal cycle removed. (c) One-to-one scatter plot of monthly SSHA (cm) and D20A (m) with seasonal cycle retained from HYCOM-INDOPAC (black), and AVISO

SSHA and HYCOM D20A (blue). (d) Same as (c) but with the first three harmonics of the seasonal cycle removed. (e) STD of the 28 to 105 day bandpass filtered SSHA (cm) from HYCOM-INDOPAC during 1993-2001. (f) Same as (e) but for AVISO SSHA.

2.4.2 Indonesian throughflow

To provide a reliable estimate of the Pacific impact on the southern Indian Ocean, it is necessary to verify the HYCOM performance in simulating the inter-basin exchange between the Indian and the Pacific Oceans. The export of water into the southern Indian Ocean is represented by the ITF, which is the sum of the transports from the Lombok Strait, Ombai Strait and Timor Passage. Since HYCOM has 0.3°x0.3° resolution and 2°x2° smoothing of topography, narrow individual channels, such as the Lombok Strait, cannot be resolved. As a result, the ITF transport in HYCOM is computed as the total zonal volume transport through the entire column along 115^{o}E from 20^{o}S to 9^{o}S, as in Capotondi et al. (2005). Indeed, it is the impacts of total ITF that we are interested in. The correlation coefficient between the modeled and observed ITF transport is 0.61 for 3-day resolution and 0.70 for the monthly mean (Figs. 2.5a-2.5b). The simulated standard deviation of ITF is 3.84 Sv, which is close to the observed 4.00Sv.

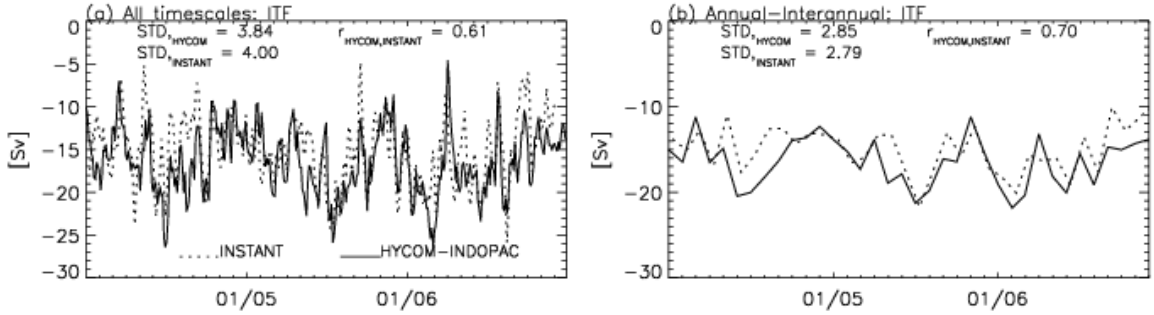

Figure 2.5: (a) Comparison between 3-day mean ITF transport (Sv) from INSTANT data and 3-day snapshot from HYCOM. (b) Same as (a) but for monthly mean.

Both the observed and simulated upper ocean temperature variability exhibits a strong annual cycle, with peak warming occurring from March to May and peak cooling from August to September (Fig. 2.6). The variability of the upper ocean ITF salinity (Fig. 2.6b) is also

dominated by a distinct annual cycle, with the lowest salinity occurring from April to June and highest salinity from November to January. Interested readers may see Sprintall et al. (2003) and Atmadipoera et al. (2009) for detailed discussions on the variability of ITF salinity. HYCOM reasonably captures the strong annual cycles of the temperature and salinity near the ITF entrance region. Both properties associated with the ITF are difficult to simulate by ocean models.

The source water that feeds the ITF is largely composed of North Pacific water characterized by a salinity maximum in the thermocline and a salinity minimum in the lower thermocline (Gordon and Fine 1996; Ilahude and Gordon 1996). The South Pacific water makes only a minor contribution to the characteristics of the ITF water (Gordon and Fine 1996). As the water travels through the Indonesian Seas, the source water is modified by air-sea interaction and strong mixing. When it enters the Indian Ocean, the ITF water is characterized by nearly homogenous salinity in the upper 1000m (e.g., Ffield and Gordon 1992; Fieux et al. 1996; Coatanoan et al. 1999; Wijffles et al. 2002; Fieux et al. 2005). Generally, the HYCOM T-S relation agrees with the Argo observation near the ITF entrance (Fig. 2.6c). The ITF water in HYCOM, however, is somewhat fresher throughout the upper 1000m, with a maximum difference of 0.2 psu in the upper thermocline. One possible reason for this systematic freshening is the excessive ERA40 precipitation in the tropical Indian Ocean during the 1990s (Yamanaka 2008).

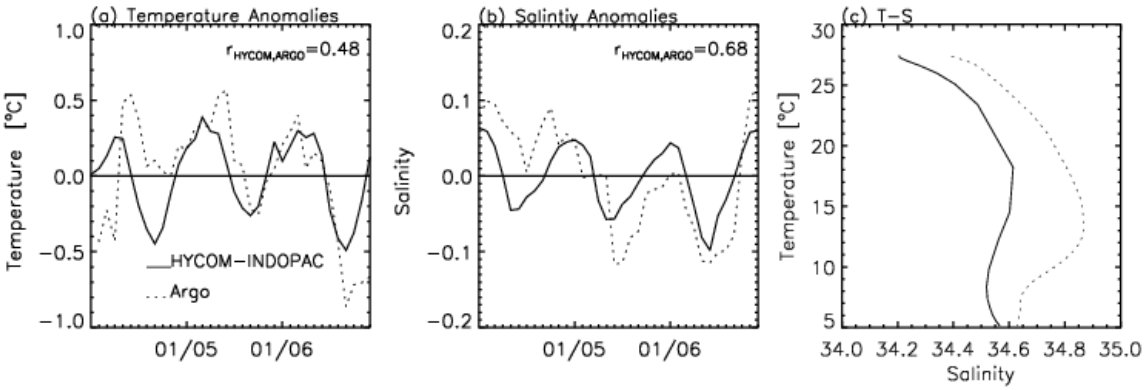

Figure 2.6: Time series of the Argo (dashed line) and HYCOM (solid line) upper ocean (0-500m mean) monthly temperature (a), and monthly salinity (b) anomalies averaged over (100°E-120°E, 9°S-20°S) region. The mean temperature and salinity values for 2004-2006 are removed. (c) Temperature-Salinity diagram for the upper 1000 m for the same region from HYCOM-INDOPAC (solid) and Argo (dashed).

2.5 Summary

These comparisons demonstrate that HYCOM does a reasonable job in simulating the large scale sea level and thermocline variability within the Indian Ocean at intraseasonal, seasonal, interannual timescales, even though the model underestimates the magnitude. The total ITF transport and its temporal variability, as well as the temperature and salinity properties near the ITF entrance region from HYCOM compare favorably with the observations. The HYCOM, however, cannot resolve the narrow Lombok Strait, as discussed above. This may result in somewhat overestimated ITF impacts at lower latitudes, including the TRIO. As we shall see in the following sections, HYCOM solutions show weak ITF effects in the TRIO region and stronger effects in the east and further south, suggesting that this model deficiency likely does not affect our major conclusions.

Chapter 3

Interannual, seasonal, and intraseasonal variability

Historically, interest in wave transmission from the Pacific to the Indian Ocean, was focused on the western boundary Rossby wave reflection and the termination of El Niño Southern Oscillation (ENSO) events (Battisti 1988). The decomposition of satellite observed SSH into the incident Rossby waves and reflected Kelvin waves, has proven to be difficult and the conclusion vary. Boulanger et al. (2003) find a Rossby wave reflection efficiency of 40-45% at the western Pacific boundary, while Zang et al. (2002) conclude that only about 30% of the incident energy is reflected. Analytical studies which used idealized (but realistic) configurations, predict a 35% reflection efficiency at the western Pacific boundary (Clarke 1991; Du Penhoat and Cane 1991), with a transmission efficiency into the southern Indian Ocean of 5-10% (Clarke 1991; Spall and Pedlosky 2005).

This chapter aims to identify the primary forcing mechanisms responsible for interannual, seasonal, and intraseasonal SSH and thermocline variability of the southern Indian Ocean. To estimate the relative importance of regional forcing over the Indian Ocean – which includes local forcing over the region and Rossby waves forced by winds to the east - and remote forcing from the Pacific via the ITF, analyses are carried out by performing various diagnostic experiments using an ocean general circulation model and a linear ocean model. Particular emphasis is placed on the TRIO region, where thermocline variability is suggested to affect sea surface temperature and thus climate. Following from historical precedence, this chapter will begin with interannual timescales.

3.1 Interannual variability

3.1.1 Horizontal pattern of variability

Consistent with previous studies (Chambers et al. 1999; Rao et al. 2002; Feng and Meyers 2003; Shinoda et al. 2004; Rao and Behera 2005; Huang and Shukla 2007a, b), the spatial structures of interannual SSHA and D20A in the southern Indian Ocean show large amplitude variability off the Java coast and near 10^{o}S with the maximum amplitude occurring near 70^{o}E, including the TRIO region. The modeled interannual SSHA and D20A with (Figs. 3.1a,d) and without (Figs. 3.1b,e) a time-varying Pacific forcing, equivalently capture the enhanced interannual variability in the south tropical Indian Ocean centered near 10^{o}S and off the coast of southern Sumatra and northern Java. Evidently, forcing over the Indian Ocean is the primary driver of SSH and thermocline variability north of 12^{o}S, while the Pacific influence appears to occur further south (Figs. 3.1c,f). The LOM-INDOPAC (Fig. 3.1g) and LOM-IND (Fig. 3.1h) further indicate that large scale interannual variability in the tropical southern Indian Ocean is forced mainly by winds over the Indian Ocean, and the processes can be largely described by linear dynamics.

3.1.2 Forcing and ocean adjustment

Forcing by winds over the Indian Ocean can result from local Ekman pumping velocity over a region, $w_e = \frac{\partial}{\partial x}(\frac{\tau^y}{\rho f}) - \frac{\partial}{\partial y}(\frac{\tau^x}{\rho f})$, and westward-propagating Rossby waves, as suggested by previous studies (Woodberry et al. 1989; Matsumoto and Meyers 1998; Birol and Morrow 2001; Wang et al. 2001; Rao and Behera 2005). In the above, w_e is the Ekman pumping velocity, τ^x and τ^y are the zonal and meridional surface wind stress components, ρ is the density of sea water and f is the Coriolis parameter. In turn, the Rossby waves can be forced by thermocline

anomalies along the eastern boundary or by Ekman pumping velocity associated with large scale wind stress curl to the east of the region.

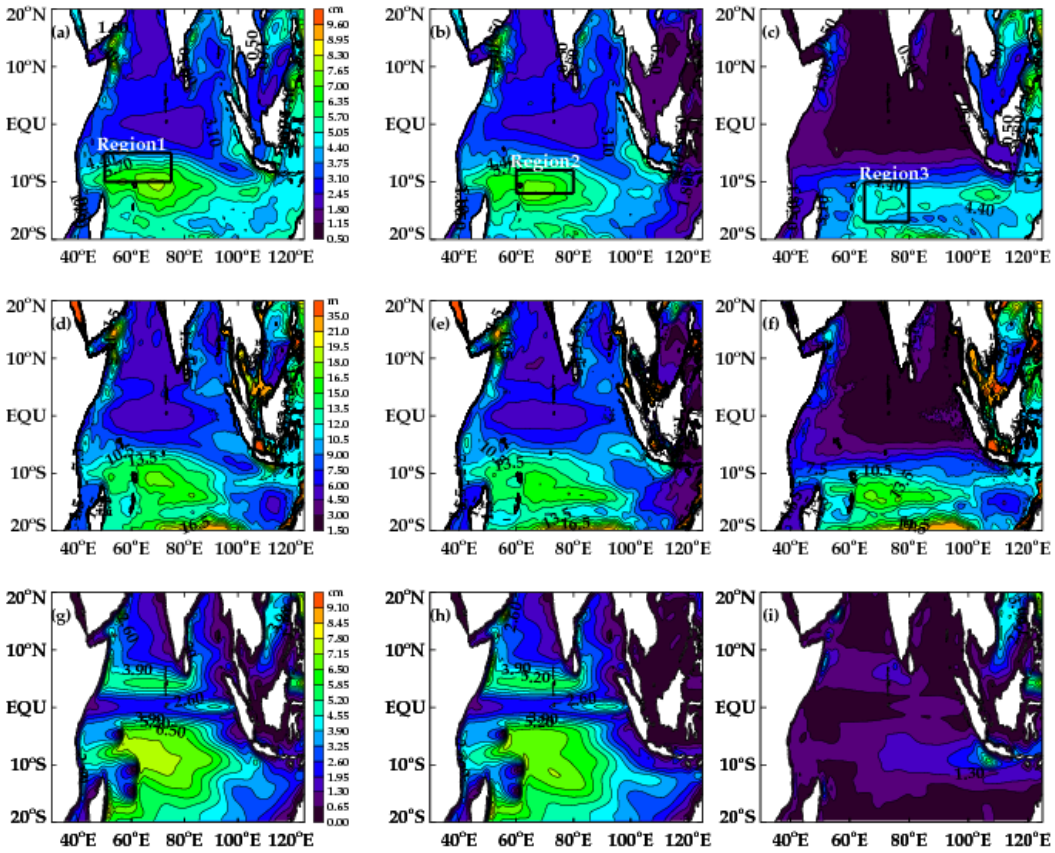

Figure 3.1**:** (a) STD of interannual SSHA (cm) from HYCOM-INDOPAC for the 1970-2001 period. The interannual SSHAs are calculated from the detrended and demeaned monthly mean SSH, with the first three harmonics of the seasonal cycle for the 1970-2001 period removed. (b) Same as in (a) but for experiment HYCOM-IND. (c) Same as in (a) but for the difference (HYCOM-DIFF). (d) Same as in (a) but for HYCOM-INDOPAC D20A (m). (e) Same as in (d) but for HYCOM-IND D20A. (f) Same as in (d) but for difference (HYCOM-DIFF) D20A. (g) STD of LOM-INDOPAC SSHA (cm) for the period 1970-2001. The SSHA is computed as the sum of the first fifteen vertical modes. (h) Same as in (g) but for LOM-IND. (i) Same as in (g) but for the difference (LOM-DIFF). The causes of thermocline variability of the boxed regions 1,2, and 3 are analyzed using Figure 3.2. Note that along the western Australian coast, significant SSHA exists in HYCOM-DIFF (panel c), whereas very little variability is shown in LOM-DIFF (panel i). These difference likely results from the limitations of the LOM.

To identify the relationship between thermocline anomalies in the west and w_e to the east, we perform lead-lad correlation analysis between the monthly values of D20A averaged in a region and the mean w_e to the east, referred to as w_{east}, which is the w_e averaged from the east edge of a boxed region to the eastern boundary of the Indian ocean. Note that the lead time between w_{east} and D20A in the west is not necessarily the propagation time of the Rossby waves.

Rather, it shows the lead time when the mean w_{east} is the strongest. However, it does provide a measure of the deterministic relationship between the leading eastern southern Indian Ocean w_e and the lagging western D20A, which demonstrate the Rossby waves' impacts in the western basin (the three boxed regions in Fig. 3.1). The northern box (Region 1, Fig. 3.1a) is selected because it surrounds the region of the annual mean minimum thermocline depth – the TRIO region (Hermes and Reason 2008; Yokoi et al. 2008; Tozuka et al. 2009). Region 2 encloses the area of greatest interannual variability, which is also within TRIO region (Fig. 3.1b; Xie et al. 2002). Region 3 encloses the area where SSHA and D20A are large and the Pacific Ocean forcing makes a significant contribution (Fig. 3.1c). Given the co-evolution of SSHA and D20A, only analysis of the latter is presented here.

In Region 1 and Region 2, interannual D20As are primarily forced by winds over the Indian Ocean, and the Pacific contributions to the amplitude and phase are weak (Figs. 3.1a, 3.1b and 3.1c). In Region 1, the correlation coefficient between the D20A of HYCOM-INDOPAC and HYCOM-IND is 0.95 at a 95% significance level. The D20A STD of HYCOM-INDOPAC is 9.82m, comparing to 8.91m from HYCOM-IND (Fig. 3.2a). In contrast, the correlation between D20A of HYCOM-INDOPAC and HYCOM-DIFF is 0.44 at a 95% significance level, and the STD of D20A from solution HYCOM-DIFF is 3.91m. In Region 2, the correlation between the D20A from HYCOM-INDOPAC and HYCOM-IND remains large (0.90). There is an overall increase in D20A variability for both solutions, and forcing over the Indian Ocean still dominates the variability (Figs. 6 and 7b). D20As from experiments HYCOM-IND and HYCOM-DIFF are essentially uncorrelated in both regions, with correlation coefficients of 0.12 in Region 1 and 0.05 of Region 2.

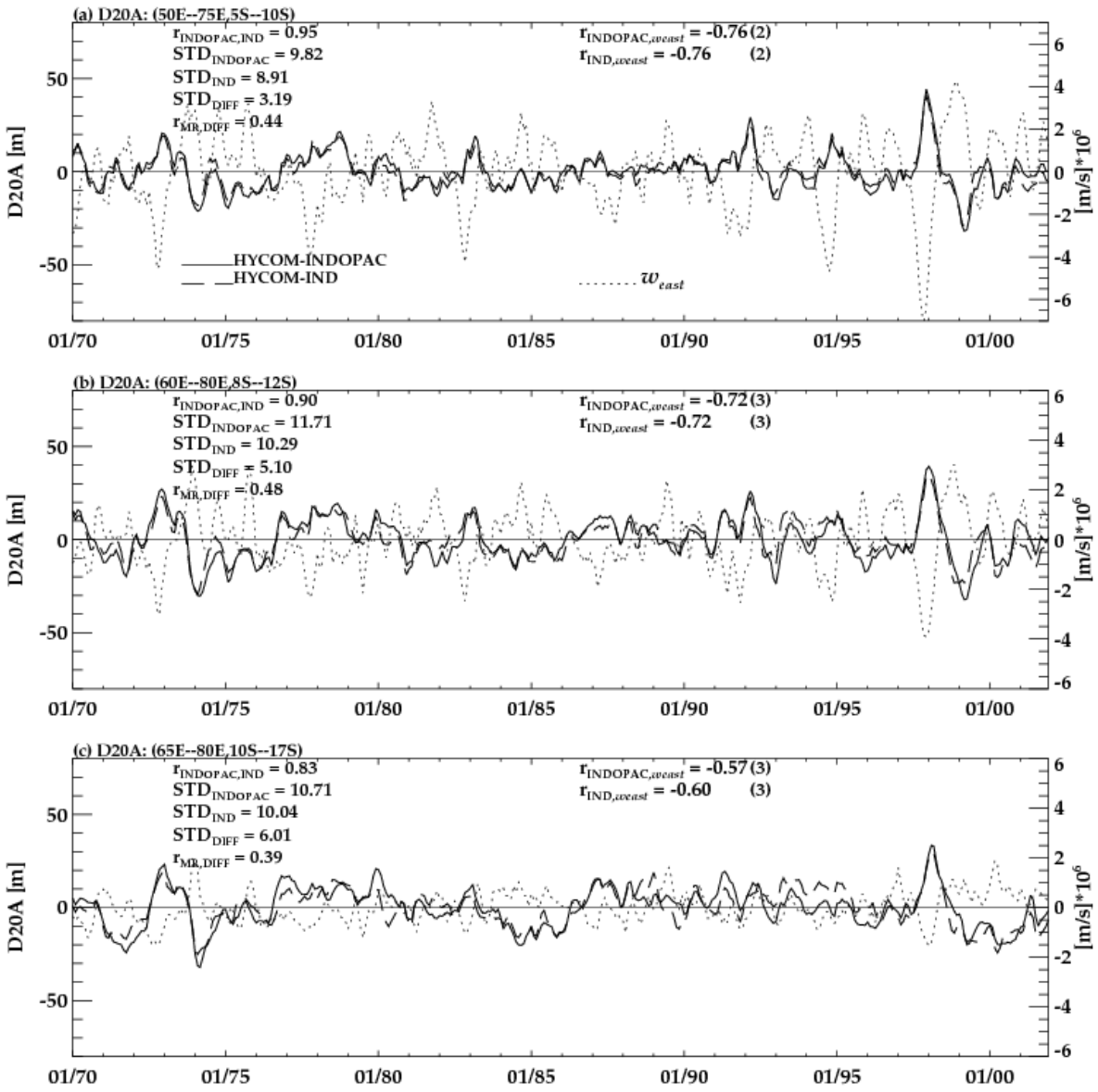

Figure 3.2: Time series of interannual D20A (m) from HYCOM-INDOPAC (black), HYCOM-IND (dashed), and area averaged Ekman pumping velocity (w_{east}, dotted, $ms^{-1}x10^{-6}$) averaged in regions (a) (5^oS-10^oS, 50^oE-75^oE) with w_{east} computed from 100^oE to 75^oE; (b) (8^oS-12^oS, 60^oE-80^oE) with the w_{east} computed from 105^oE to 80^oE; and (c) (10^oS-17^oS, 65^oE-80^oE) with w_{east} computed from 120^oE to 80^oE.

This suggests that thermocline anomalies forced by winds over the Indian Ocean can interfere constructively or destructively with those forced by winds over the Pacific, and there is no deterministic phase relations between the two. The D20A are most impacted by the Pacific forcing south of 12^oS (Region 3), even though the effects of Indian Ocean forcing is still larger (Fig. 3.2c). The

correlation between the D20As of HYCOM-INDOPAC and HYCOM-IND is 0.83, and the STD of D20A is ~10.71m, 10.04m, and 6.01m from HYCOM-INDOPAC, HYCOM-IND, and HYCOM-DIFF, respectively.

In all three regions, local Ekman pumping over the region (time series not shown) is not the direct cause of interannual D20A, as evidenced by the weak correlations between the regionally-averaged w_e and D20A, which are 0.1, 0.2, and 0.1 for Region 1, 2, and 3, respectively. In contrast, D20A is strongly correlated with w_{east}, indicating that Rossby waves generated by interior Indian Ocean winds are the primary cause. North of 12^{o}S, both HYCOM-INDOPAC and HYCOM-IND D20As are strongly correlated with w_{east}, with the maximum correlation of -0.76 in Region 1 when w_{east} leads D20A by 2 months, and -0.72 in Region 2 when w_{east} leads D20A by 3 months. These results are confirmed by the LOM solutions, which show both the dominance of the Indian Ocean forcing and the westward enhancement of SSHA (Figs. 3.1g-3.1i). The correlation between LOM-INDOPAC and LOM-IND (not shown) is 0.98 in both Regions 1 and 2. This result is consistent with Masumoto and Meyers (1998), who concluded that the amplitude and structure of the southern interannual Rossby wave is determined by the large scale open ocean w_e acting on the Indian Ocean.

In Region 3, the D20As from HYCOM-INDOPAC and HYCOM-IND obtain the highest correlation of ~0.6 when w_{east} leads by ~3months, indicating that Rossby waves forced by the Indian Ocean winds are important for this region, although the Pacific forcing becomes more important than Regions 1 and 2 (Fig. 3.1). Similar conclusions also hold for the LOM solutions (Figs. 3.1g-3.1i). Note that even though the LOM produces similar large-scale SSHA structures in the tropical southern Indian Ocean as those of HYCOM, there are apparent differences between the two solutions. For example, the relative SSH maximum near 20°S of the central basin from 60°E-100°E in HYCOM-DIFF is absent from the LOM-DIFF solution. A few

possible reasons may contribute to the differences. Firstly, the LOM has no nonlinear terms, and thus advection by the background flow is not represented. Secondly, the LOM has a flat ocean bottom, and thus straits and islands are represented as vertical walls. This limitation eliminates the effects of topographic slope, which is important for trapping the Leeuwin current to the west Australian coast (Julian P. McCreary, person. commu. 2011) and may amplify the SSHA response near the topographic region, such as Region 3. Thirdly, the LOM blocks the connection between the Indian and Pacific Ocean south of Australia. This could affect the SSHA simulation in the subtropical and midlatitude southern Indian Ocean. Lastly, the LOM does not include the barotropic mode. Despite these limitations, the LOM is still a useful tool to help understand the processes associated with the ITF influence (e.g., McCreary et al. 2007), and to identify linear versus nonlinear processes. Physically, the HYCOM/LOM difference near 20°S may partly arise from oceanic instabilities. Observations and modeling studies indicate that the southern Indian Ocean is rich in eddy activities (Ogata and Matumoto 2011; Jia et al. 2011).

3.1.3 Negative event composite

To further discern the effects of local w_e forcing, Rossby waves forced by winds to the east of the region within the Indian Ocean, and remote forcing from the Pacific, composites of the horizontal structure of thermocline anomalies and w_e are constructed for both positive and negative thermocline anomaly events. Event identification is based on the average D20A in the region 60^oE-80^oE; 8^oS-12^oS (Region 2, Fig. 3.1a). An event is considered positive if the magnitude of the D20 anomaly exceeds 1 standard deviation for at least three consecutive months. Using similar criteria, an event is classified as negative if the standardized anomaly exceeds -1 for three consecutive months. The peak in the magnitude for both positive and

negative events occurs in boreal winter to early spring (Fig. 3.3). Based on the above criteria, four events were identified as positive (1972-1973, 1982-1983, 1991-1992, and 1997-1998) and four events were identified as negative (1971-1972, 1973-1974, 1992-1993, and 1998-1999). The four positive events are either associated with positive IOD, El Niño, or both. The negative events are associated with negative IOD, La Niña, or both (Fig. 3.3). The correlation between the D20A index and Dipole Mode Index (DMI) is 0.57 when DMI leads the D20A index by 4 months. The maximum correlation between the D20A index and NINO3.4 index is 0.61 when NINO3.4 leads by 3 months. These events are somewhat different from those of Tozuka et al. (2010).

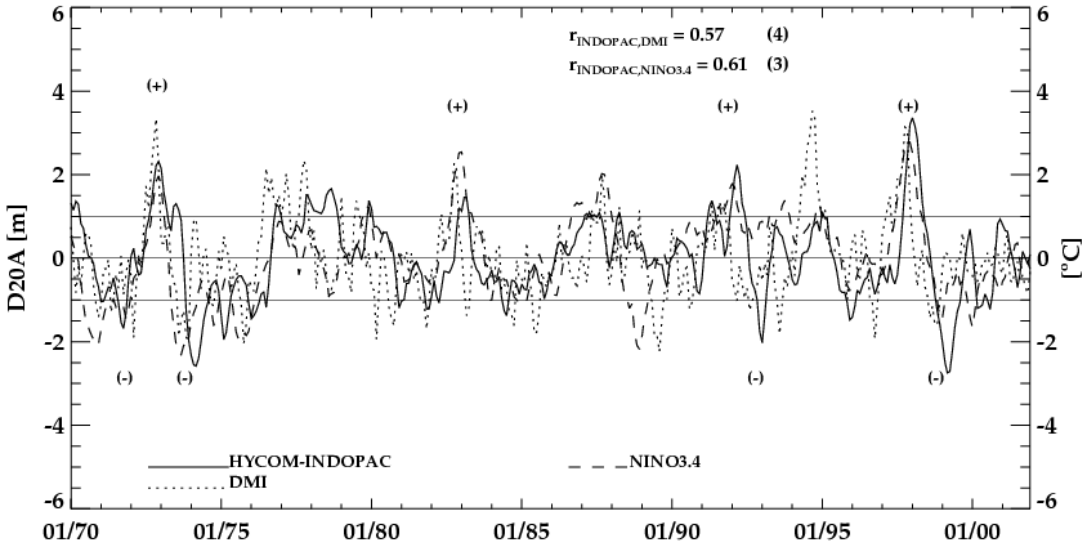

Figure 3.3: Time series of normalized interannual D20A (black) averaged for (8°S-12°S, 60°E-80°E), which is Region 2 of Fig. 6, the normalized Dipole Mode Index (DMI, dotted), and normalized NINO3.4 index (dashed) from HYCOM-INDOPAC. The horizontal lines at ± 1 (°C and m) denote departures of one standard deviation. The "+" and "-" indicate the events that are used to construct composite events, when D20As exceed one standard deviation for three consecutive months.

Even if we use the same index as Tozuka et al. (2010), the events are not exactly the same. This may in part be due to the fact that Tozuka et al. (2010) simulate a different time period (1980-2007), use a coarser resolution version of Modular Ocean Model, and use NCEP forcing fields.

The negative events are associated with the arrival of upwelling Rossby waves, which are forced by large scale anomalous positive Ekman pumping velocity in the eastern southern Indian Ocean during boreal summer-fall (Fig. 3.4a), as suggested by Tozuka et al. (2010). Near the eastern boundary of the equatorial Indian Ocean, the positive D20A develops in association with anomalous equatorial westerlies that cause equatorial Ekman convergence and an eastward-propagating downwelling Kelvin wave, in addition to coastal downwelling forced by anomalous southward longshore winds. These winds, however, generate positive w_e anomalies in the eastern tropical southern Indian Ocean, which force the thermocline to shoal (negative D20A). By December of year 0, the positive w_e in the south tropical Indian Ocean reaches its peak, and the upwelling Rossby wave propagates westward with an enhanced amplitude, obtaining its peak strength in the TRIO region (Fig. 3.4b). By March of year 1, the Rossby wave progresses further westward with a weakening w_e to the east (Fig. 3.4c). By August of year 1, the upwelling Rossby wave reaches the western boundary with apparently weakened amplitude, concurrent with the weak w_e (Fig. 3.4d, left). Comparing to the Indian Ocean forcing, contribution from the Pacific forcing is weak in the TRIO region (right column, Fig. 3.4), a result that is not addressed by Tozuka et al. (2010). These results demonstrate that interannual variability of sea level and thermocline in the TRIO region is largely caused by Rossby waves driven by the Indian Ocean winds to the east of the region, consistent with the time series analysis presented above.

The westward propagating Rossby wave signals are more clearly seen in the longitude-time plot of HYCOM D20A and LOM SSHA for the composite negative events (Fig. 3.5). Along 7^{o}S-8^{o}S, both HYCOM-INDOPAC and HYCOM-IND show westward-propagating Rossby waves that originate from the east and enhance toward the west, obtaining their maxima in the TRIO region (Fig. 3.5a). The corresponding LOM solutions show remarkably similar

propagating patterns (Fig. 3.5b), suggesting that the linear wind-driven wave dynamics determine the SSH and D20 variability in TRIO region. Forcing from the Pacific has significant amplitudes in the eastern basin and has little influence on the TRIO region (right panels of Figs. 3.5a-3.5b). This further confirms the previous assertion that the Pacific contributes little to the variability equatorward of Indonesian Passage (Figs. 3.1c, 3.1f).

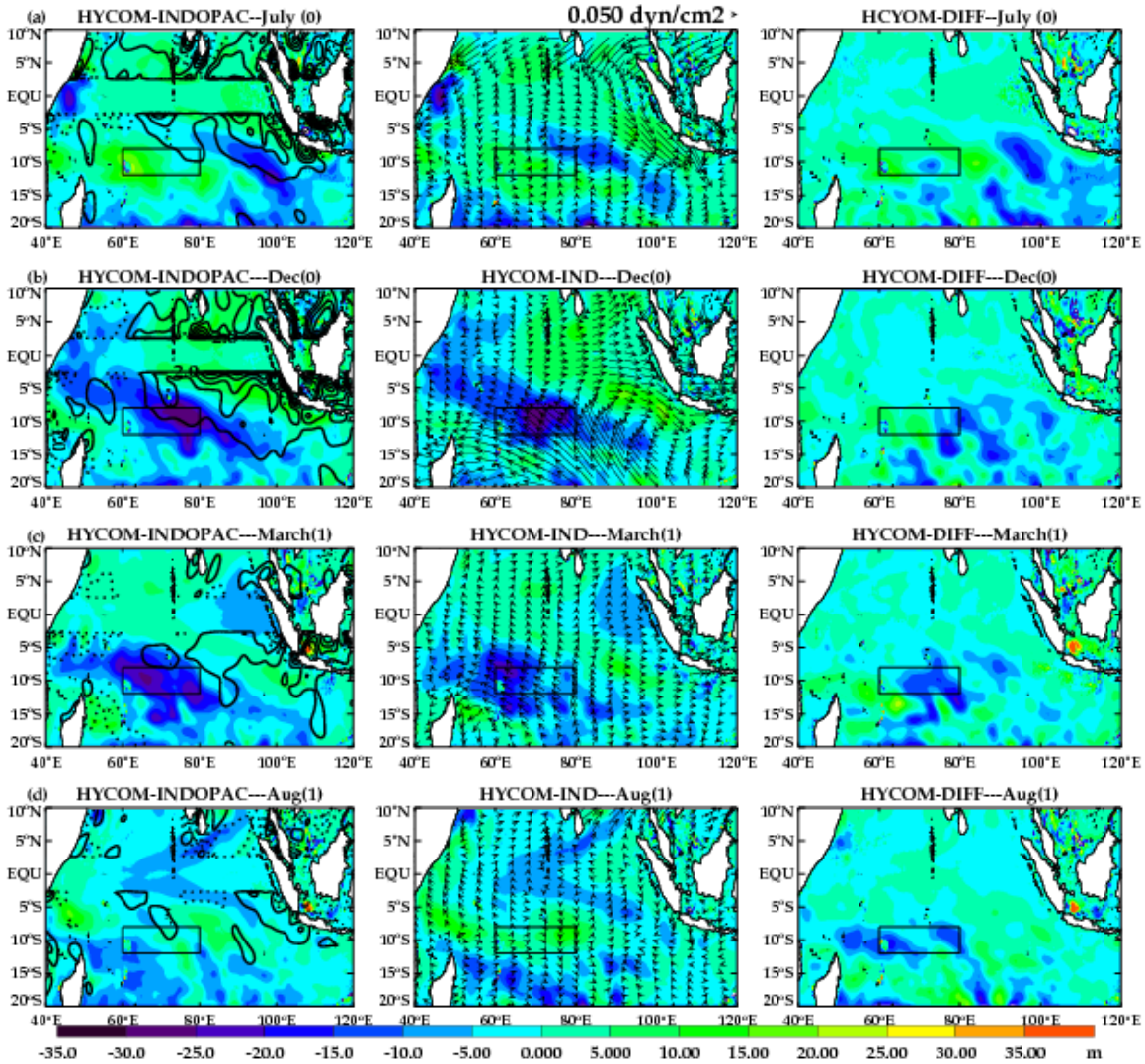

Figure 3.4: Horizontal maps showing the evolution of D20A (m), w_e ($ms^{-1}x10^{-6}$), and surface wind stress (dyn cm^{-2}) for the composite of four negative events indentified in Figure 3.3 based on the D20A index averaged in the TROI region (The boxed region of Fig. 3.4, which is Region 2 of Fig. 3.1). (a) July of year 0, (b) December year 0, (c) March of year 1, which indicates the following year, and (d) August of year 1. D20A and w_e composites from HYCOM-INDOPAC experiment are shown in the left column, those from HYCOM-IND experiment are shown in the middle, and their differences (HYCOM-DIFF) are shown in the right column. D20As are represented by the color contours, anomalous interannual Ekman pumping velocities (w_e) by lined contours in the left column, and anomalous interannual surface wind stress by vectors in the middle column. The w_e contour increment is $1.5*10^{-6}$ m s^{-1}.

In both the HYCOM and LOM solutions, Rossby waves are getting progressively slower and shorter with the increase of latitude toward the south (Figs. 3.5c-3.5f), as expected from the Rossby wave phase speed equation and dispersion relation. Differences between HYCOM and LOM solutions increase with the increase of latitude, indicating that nonlinearity of oceanic system becomes more important in subtropical ocean than in the tropics.

Note that Rossby waves generated by the Ekman pumping velocity anomalies near the eastern boundary during boreal summer propagate into the TRIO region in about 4-5 months. This propagation time is longer than the approximate travel time of the linear 1^{st} baroclinic mode Rossby wave. The Rossby wave speeds of the 1^{st} baroclinic mode, estimated from the 5^{o}S-20^{o}S HYCOM density profile, are ~56 cm s^{-1} in the middle of Region 1 (7.5^{o}S) and ~31 cm s^{-1} in the middle of Region 2 (10^{o}S). These phase speeds predict a travel time of 2 months for Region 1 and 3 months for Region 2. The speed of the Rossby waves in HYCOM is also slower than the combined effect of the 1^{st} and 2^{nd} baroclinic modes in the LOM especially along 7°S-8°S. The apparent slowing down of Rossby waves in HYCOM could be due to nonlinear effects and changes of stratification along the Rossby waves' path.

3.1.4 Positive event composite

The positive events are associated with the arrival of downwelling Rossby waves. As was the case for the upwelling Rossby wave, the downwelling Rossby wave is forced by large scale Ekman pumping velocity in the southeastern Indian Ocean during boreal summer-fall (Fig. 3.6a). This wave continues to propagate westward under downwelling favorable winds, obtaining its peak amplitude during December of year 0 – January of year 1 (Fig. 3.6b). By August of year 1, the deepened thermocline associated with the arrival of the downwelling Rossby wave

essentially disappears in the TRIO region due to the abatement of the negative w_e and transition to positive w_e in the eastern basin (Fig. 3.6d). The Pacific contribution to thermocline variability of the TRIO region is weak, with significant D20A confined to the eastern basin (right panels of Fig. 3.6).

Along 7^oS-8^oS, both HYCOM-INDOPAC and HYCOM-IND show westward-propagating positive D20As that originate from the east and enhance toward the west, obtaining peak amplitude in December of year 0 in the TRIO region (Fig. 3.7a). The LOM solutions show similar westward-propagating signals that are dominated by the Indian Ocean forcing. Remote forcing from the Pacific has significant amplitude in the eastern basin, which radiates westward as Rossby waves and strengthens the positive D20A in the TRIO region. Its amplitude, however, is weak comparing to the D20A generated by the Indian Ocean forcing. Further south, Rossby waves are progressively slower and wavelengths are shorter in both HYCOM and LOM, and the differences between HYCOM and LOM solutions increase (Figs. 3.7c-3.7f). Consistent with our discussion for the negative events, in the lower latitudes of the tropical southern Indian Ocean, interannual SSHA and D20A are primarily determined by wind-driven, linear wave dynamics, and nonlinearity of oceanic system becomes more apparent with the increase of latitude.

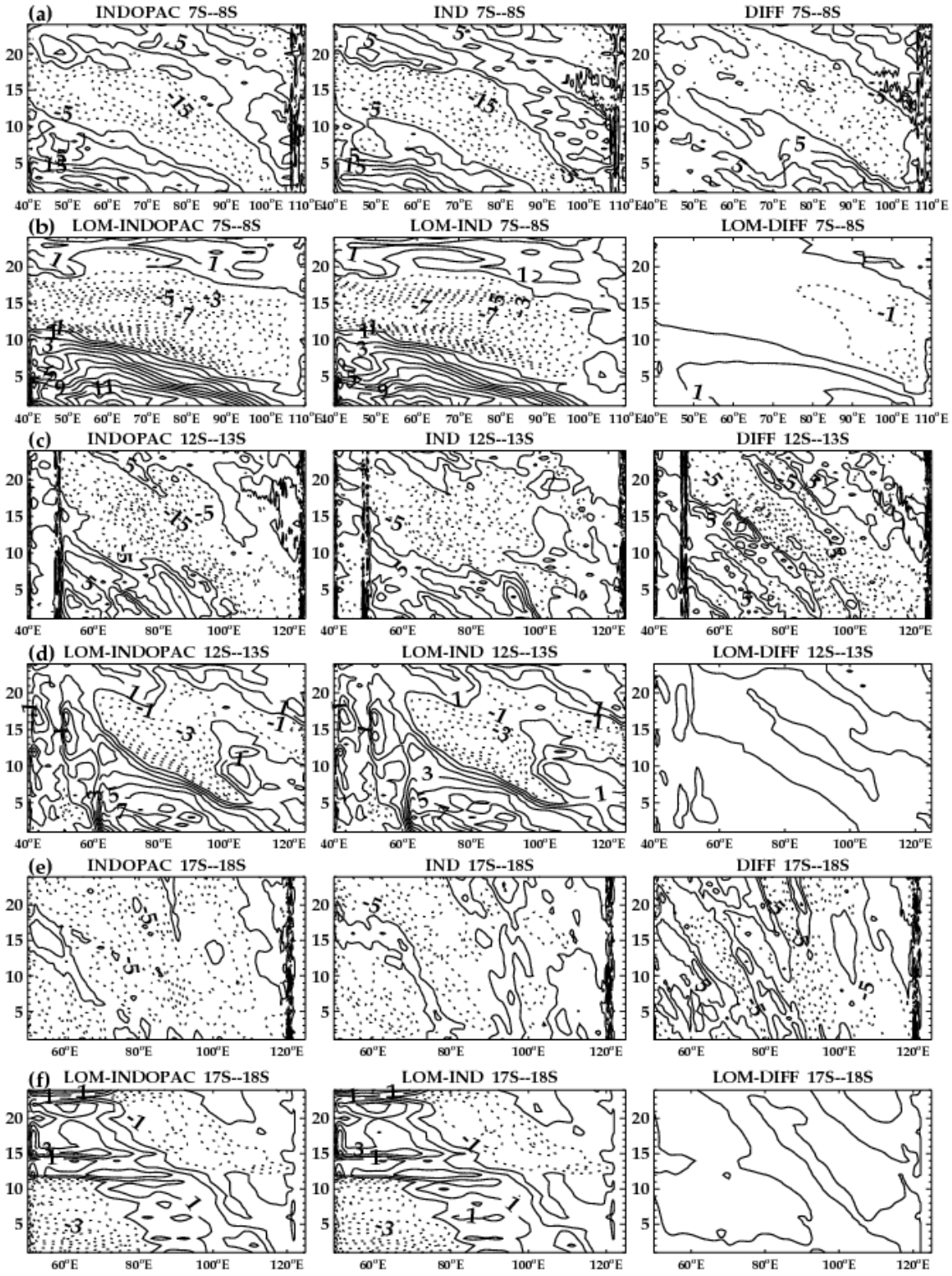

Figure 35: (a) Longitude-time plots of the composite D20A (m) based on the negative events shown in Fig. 3.3 averaged over the 7°S-8°S latitude band from HYCOM-INDOPAC (left), HYCOM-IND (middle) and HYCOM-DIFF (right); (b) Same as (a) but for LOM SSHA (cm) from the sum of the 1st and 2nd baroclinic modes; (c) Same as (a) but averaged over 12°S-13°S band; (d) Same as (c) but for LOM SSHA; (e) Same as (a) but averaged over the 17°S-18°S band; (f) Same as (e) but for LOM SSHA. Negative values (dashed contours) indicate a shoaling thermocline, and positive values (solid contours) depict a deepening thermocline, with an interval of 5m. Similarly,

positive SSHAs from the LOM are solid and negative ones are dashed, with an interval of 1 cm. Time is given in months (vertical axis), where 1 corresponds to January of year 0, 13 to January of year 1, and so on.

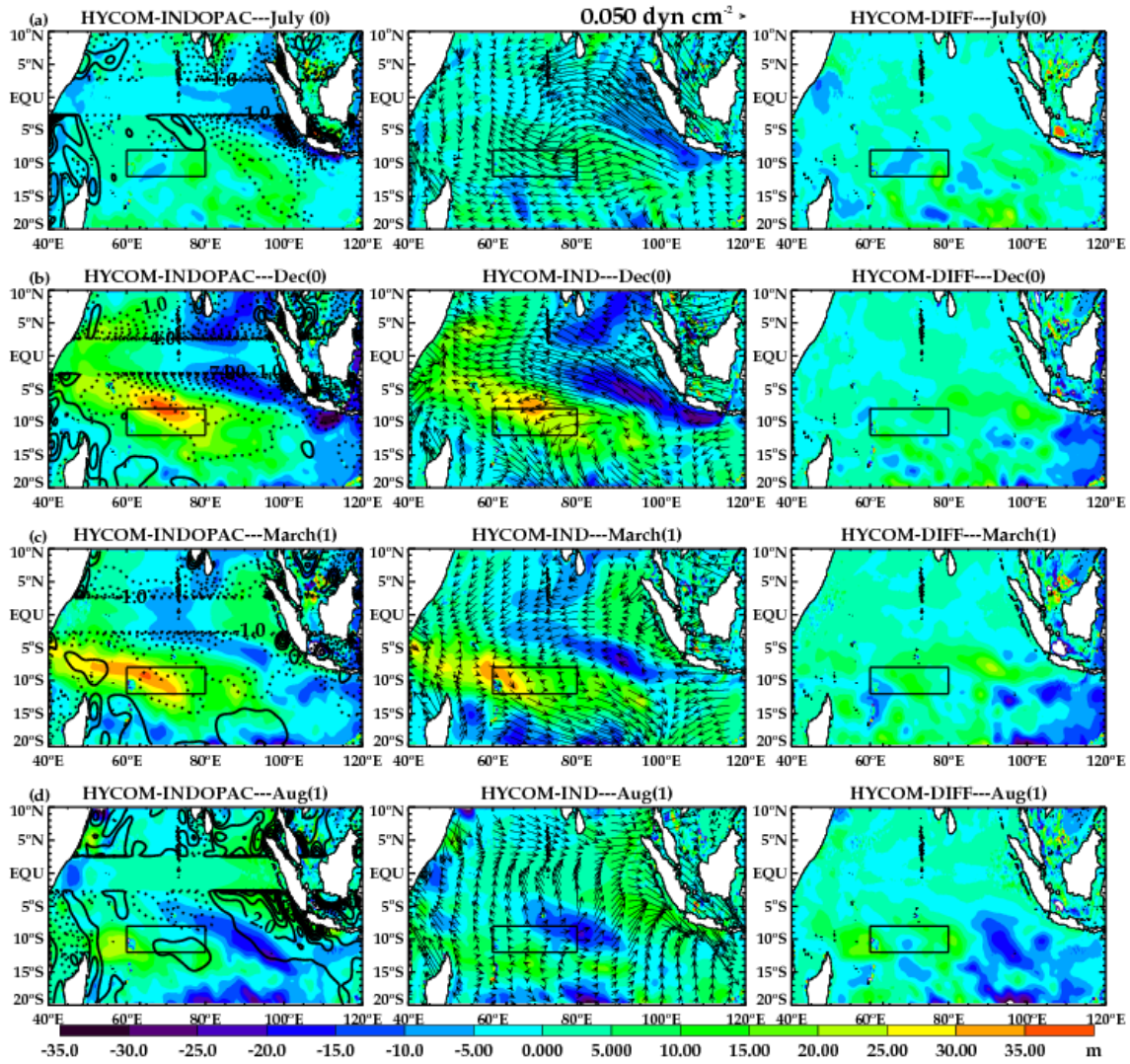

Figure 3.6: Same as in Fig. 3.4 but for the composite of the four positive D20A events.

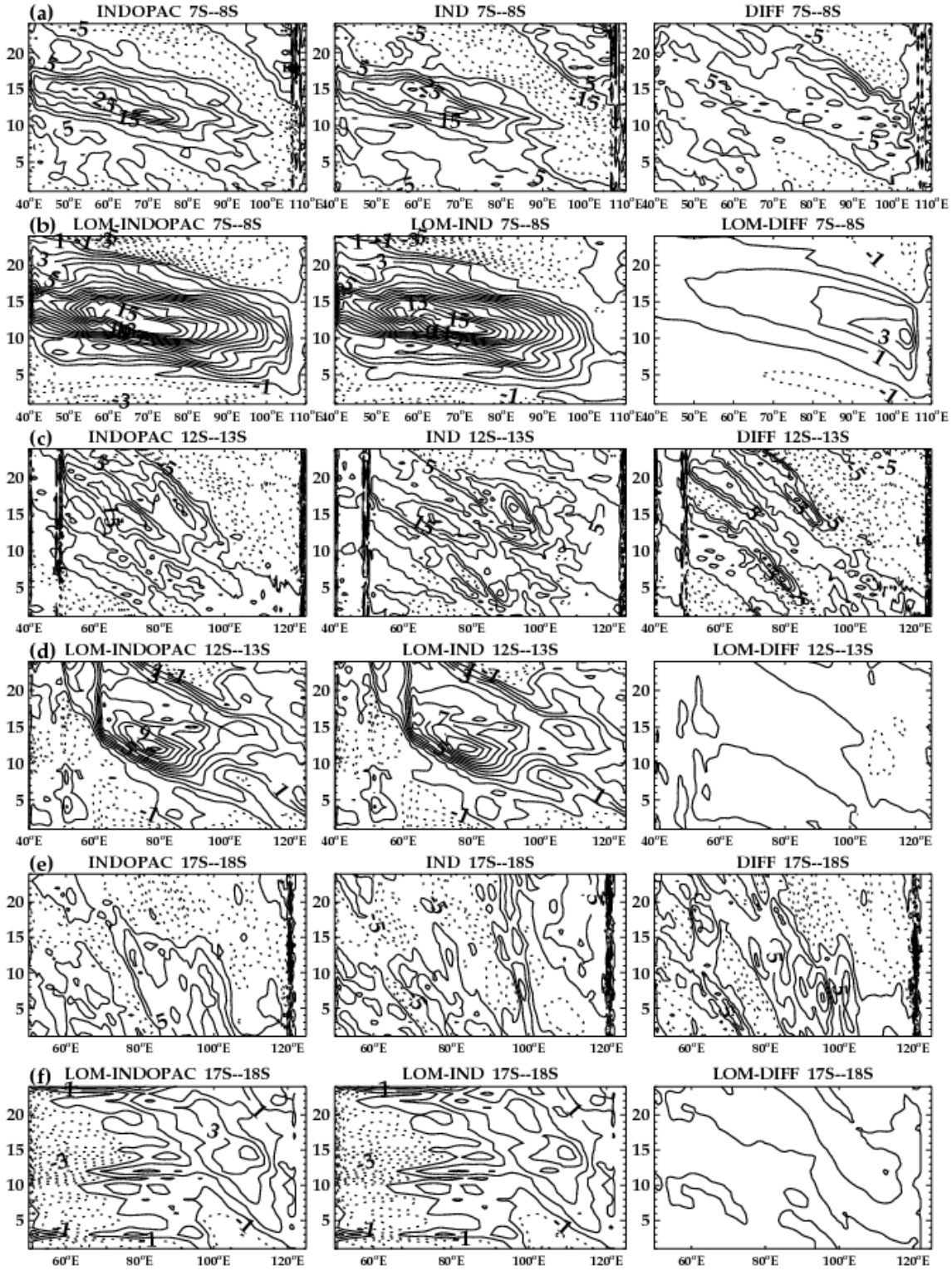

Figure 3.7: Same as in Fig. 3.5 but for the composite of the four positive D20A events identified in Fig. 3.3

3.2 Seasonal variability

A strong semiannual cycle of D20A is detected in Region 1 (Fig. 3.8a), and an annual cycle is shown in Region 2 (Fig. 3.8b) from HYCOM solutions. In Region 1, both the HYCOM-INDOPAC and HYCOM-IND experiments show that D20A is deepest in February and September and shallowest in May and December, in agreement with Hermes and Reason (2008) and Tozuka et al. (2010). The good agreement between HYCOM-INDOPAC and HYCOM-IND suggests that seasonal variability of D20 in this region is primarily forced by winds acting on the Indian Ocean. Further, the LOM results (Fig. 3.8c) demonstrate that the contributing dynamics are fundamentally linear and dominated by the first two modes, even though there are quantitative differences between HYCOM and LOM solutions. The results are essentially unchanged when all of the fifteen modes are retained in the LOM solutions (not shown). To estimate the relative contributions of local w_e forcing and Rossby waves forced by winds to the east of the region, we estimate the total vertical velocity of D20 from solution HYCOM-IND, with $w_{total} = -\frac{\partial(D20A)}{\partial t}$. Based on this definition, $w_{total} = w_e + w_{IO\_Rossby,}$ where w_{IO_Rossby} is the vertical velocity of D20 caused by Rossby waves generated by winds east of the region.

In Region 1, the largest discrepancies between the local w_e (Fig. 3.8a, dotted line) and w_{total} (Fig. 3.8a, dash-dotted line) occur during the first part of the year (January –May), indicating the importance of Rossby wave influence. Indeed, influences of Rossby waves for this period of time are clearly seen from Fig. 3.9a and Fig. 3.9b (left and middle panels). During the second half of the year especially from July to October, the local w_e dominates over w_{total}, as evidenced by their good agreement. The dominance of local forcing for this period is also suggested by Figs. 3.9a and 3.9b, when the local D20A maximum is separated from the westward propagating features,

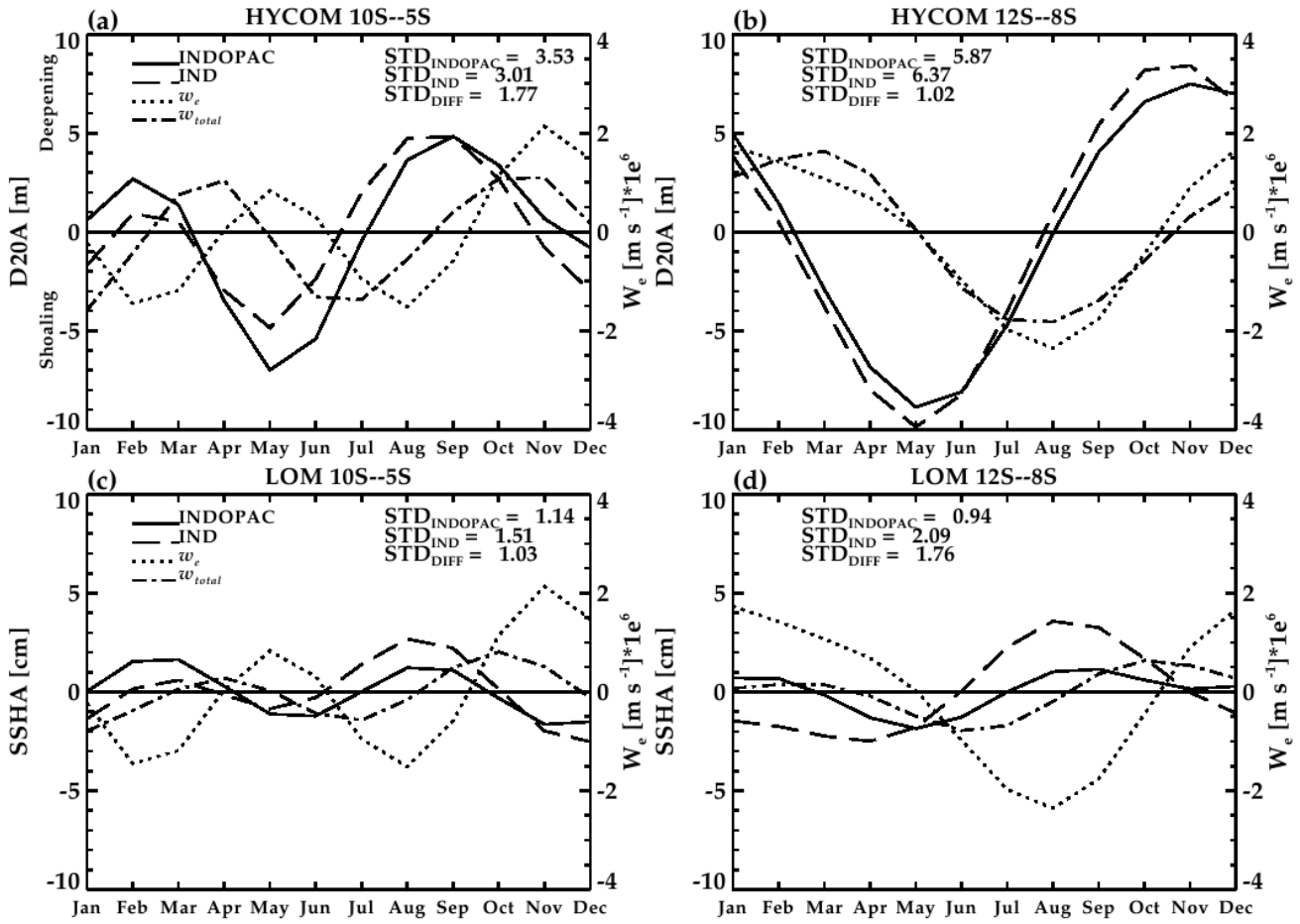

Figure 3.8: Time series of the monthly seasonal cycle of D20A (m) from HYCOM-INDOPAC (black), HYCOM-IND (dashed), local Ekman pumping velocity (w_e, dotted, $ms^{-1}x10^{-6}$), and estimated total vertical velocity of D20 from HYCOM-IND (w_{total}, dash-dotted, $ms^{-1}x10^{-6}$) averaged over region (a) 5^oS-10^oS; 50^oE-75^oE; and (b) 8^oS-12^oS; 60^oE-80^oE; Note that a positive w_{total} corresponds to a "shoaling D20", and a negative w_{total} corresponds to a "deepening D20". (c) Same as (a) but for LOM SSHA (cm) from the sum of the 1st and 2nd baroclinic modes; (d) same as (c) but for 8^oS-12^oS; 60^oE-80^oE region. The seasonal cycle is calculated by first removing the 1970-2001 mean of D20, and then formed by the first three harmonics of the seasonal cycle.

even though Rossby waves may also have some contribution (Fig. 3.8). In agreement with Wang et al. (2001), it appears that local forcing in the west and Rossby waves in the east contribute to the double maximum structure in D20A during July-November (Fig. 3.9a, left and middle). The Pacific forcing has large amplitude in the eastern basin, with part of its energy radiating westward as Rossby waves and contributing to the D20A in Region 1. Its amplitude, however, is rather weak comparing to the D20A forced by the Indian Ocean winds. Constructive interference with the Indian Ocean forced signals occurs during the first half and destructive interference for the second half of the year. Negative D20As from the Pacific enter the southern Indian Ocean

during boreal winter-spring, and positive ones during boreal fall (Fig. 3.9a, right column). The constructive and destructive interference from the Pacific forcing is further confirmed by the LOM solutions (Figs. 3.9c and 3.9b).

The propagation and influence of Rossby waves discussed above are evident in Fig. 3.10. An upwelling Rossby wave forced by positive w_e in the eastern basin during boreal winter (3.10a, left and middle panels) propagates westward and contributes to the boreal summer thermocline shoaling in Region 1 (Fig. 3.8a). It reaches 55^{o}E by June (Fig. 3.9a, left and middle), with a phase speed of ~56 cm s^{-1} (Fig. 3.9a, left and middle). On the other hand, a downwelling Rossby wave is generated by negative w_e during boreal fall near 100^{o}E (Fig. 3.10c, left and middle panels). As the Rossby wave propagates westward, it is first enhanced by the negative w_e to the west (Fig. 3.10c, left and middle), and then damped by the positive w_e anomalies in December (Figs. 3.10d and 3.10a, left).

In Region 2 (the southern edge of TRIO), thermocline variability exhibits a strong annual cycle, obtaining a minimum depth in May and a maximum depth in November (Fig. 3.8b). The phase of the annual cycle is identically captured by HYCOM-INDOPAC and HYCOM-IND, indicating that Indian Ocean forcing is the major driver. The good agreement between w_e and w_{total} demonstrate the dominance of local forcing on D20A in the region. There are, however, noticeable differences between w_e and w_{total} (Fig. 3.8d), suggesting that Rossby waves can also make significant contributions. For example, the arrival of an upwelling Rossby wave from May to September (Figs. 3.10b and 3.10c) reduces the speed of the deepening thermocline caused by local w_e (Figs. 3.8b and 3.10c). In contrast, the arrival of a downwelling Rossby wave in December (Fig. 3.10d, left and middle) reduces the speed of the shoaling thermocline driven by local w_e (Figs. 3.8b and 3.10d).

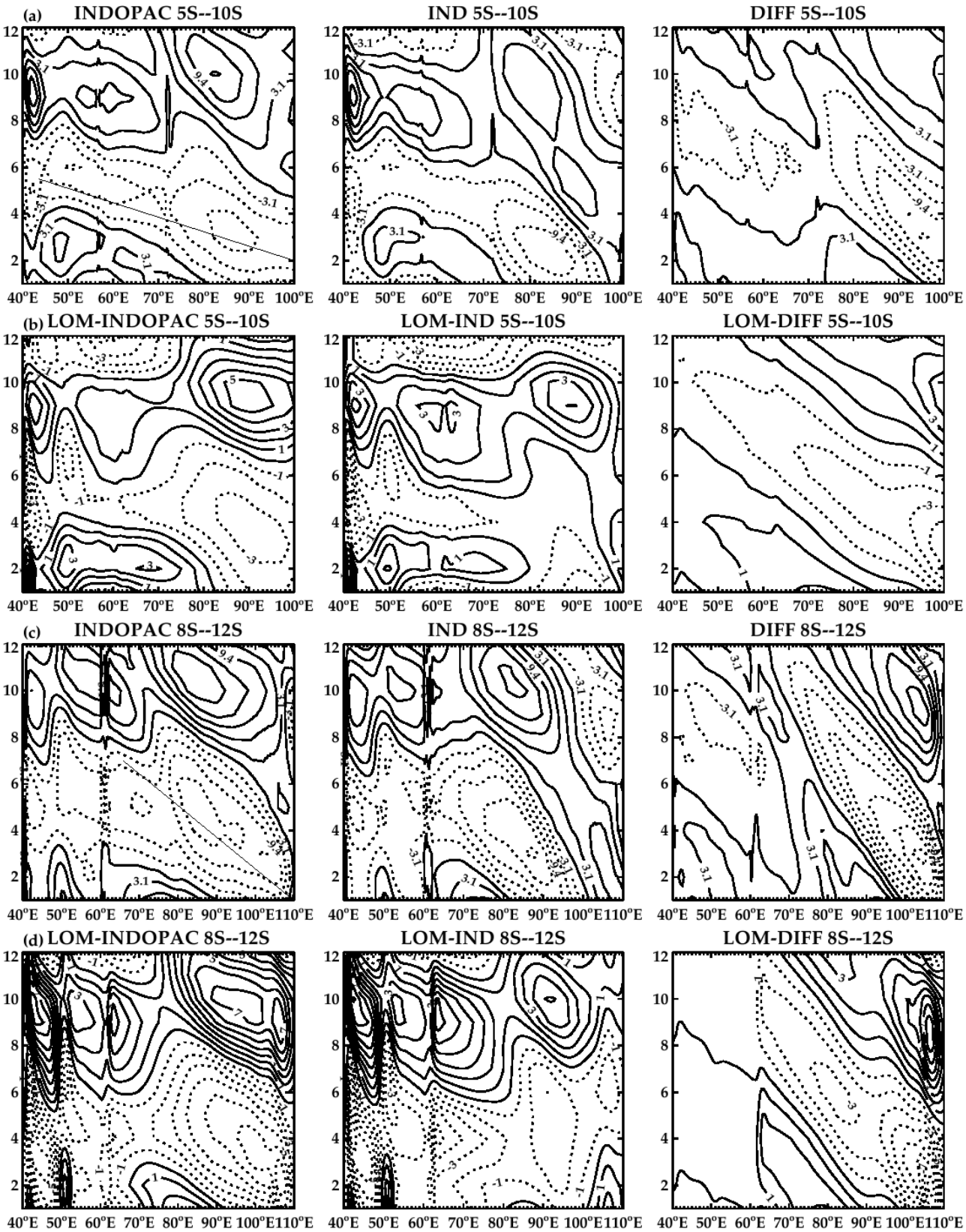

Figure 3.9: (a) Longitude-time plots of the seasonal thermocline anomalies (m) in the southern Indian Ocean for HYCOM-INDOPAC (left), HYCOM-IND (middle) and HYCOM-DIFF (right) for the latitude bands (a) 5^{o}S-10^{o}S;

the straight line shows the Rossby wave phase line; (b) Same as in (a) but for the LOM SSHA (cm) from the sum of the 1st and 2nd baroclinic modes; (c) Same as (a) but for 8°S-12°S; (d) Same as in (c) but for the LOM SSHA. Negative values (dashed contours) indicate a shoaling thermocline, and positive values (solid contours) depict a deepening thermocline. The interval for D20A is .125m and1cm for SSHA. Time is given in months, where 1 corresponds to January and 12 to December.

As for Region 1, the Pacific forcing causes large amplitude D20A in the eastern basin east of 80°E (Figs. 3.9 and 3.10). Signals of the D20A propagate westward with weakening amplitudes, which act to reduce the D20A amplitudes in Region 2 (Fig. 3.9c). The D20As due to the Pacific forcing are generally out of phase with the D20As forced by longshore winds (Fig. 3.10, compare middle and right panels). As a result, the Pacific forcing reduces the thermocline variability in solution HYCOM-INDOPAC south of Java. Adding the Pacific signals basically removes D20 variability generated locally by the along shore winds in the region.

3.3 Intraseasonal variability

The spatial patterns of intraseasonal SSHA from HYCOM-INDOPAC and HYCOM-IND are remarkably similar (Figs. 3.11a-3.11b), showing regions of enhanced intraseasonal variability south of Sumatra and Java within a zonal band that extends westward into the interior Indian Ocean along 12°S. Significant variability also appears in the vicinity of the Somali current, south of India and along the coast of Sumatra. Intraseasonal SSHA in most regions of the Indian Ocean north of 10°S result mainly from Indian Ocean intraseasonal wind forcing (compare Figs. 3.11a-3.11c and 3.11d-3.11f), except for the Somali coast where instabilities also have large contributions (Brandt et al. 2003; Han et al. 2007; Schott et al. 2009; Schiller et al. 2010). In the tropical southern Indian Ocean between 10°S-15°S, a region of focus for this study, however, intraseasonal SSHA occurs in all HYCOM solutions: HYCOM-INDOPAC, HYCOM-IND and HYCOM-DIFF, suggesting that either both the Indian Ocean and Pacific intraseasonal winds are important, or instabilities due to nonlinearity of the oceanic system are crucial for causing the intraseasonal SSHA in the region. Both the LOM-INDOPAC and LOM-IND (Figs. 3.11d-3.11e) capture the region of enhanced variability off the Sumatran coast associated with the intraseasonal Kelvin wave,

and the variability within the TRIO latitude spanning 0-10°S. Conspicuously, the region of largest variability in the HYCOM experiments is essentially absent from all the LOM solutions. These results suggest that the largest intraseasonal variance in the southeast tropical Indian Ocean results primarily from oceanic instabilities since the LOM only includes wind-driven linear wave dynamics. The Pacific forcing can somewhat modify these instabilities (compare Figs. 3.11a-3.11c, 3.11d-3.11f).

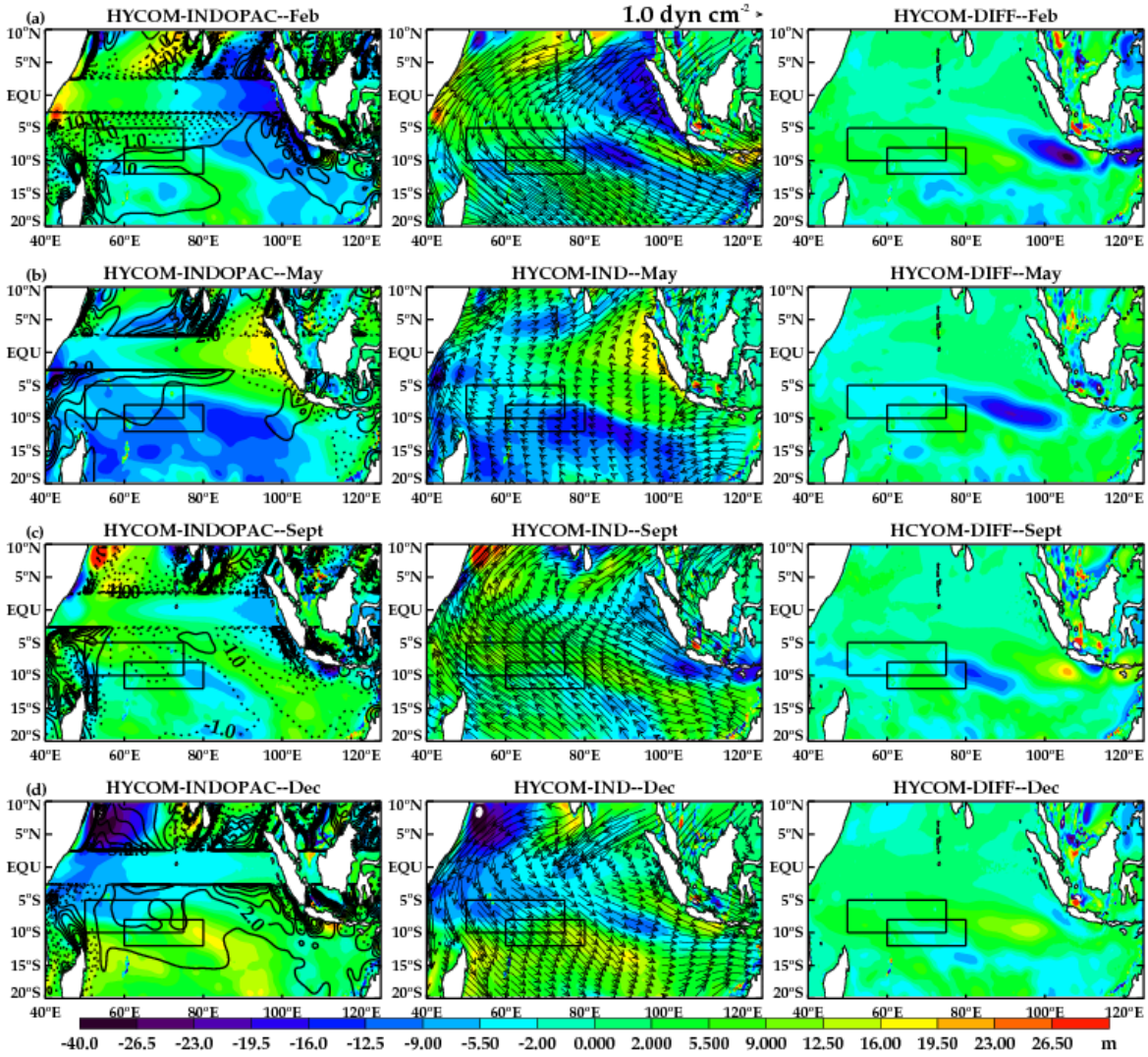

Figure 3.10: (a) Horizontal maps showing the seasonal cycle of thermocline anomalies – D20A (color contours, m) from HYCOM-INDOPAC (left), HYCOM-IND (middle) and HYCOM-DIFF (right) for February; Anomalous Ekman pumping velocities ($w_{e,}$ lines, $ms^{-1}x10^{-6}$) are also shown in the left panel with an increment of $1.5*10^{-6}$ m/s, and surface wind stress (vectors, dyn cm^{-2}) are shown in the middle panel; (b), (c) and (d) are the same as (a) but for May, September, and December, respectively.

Why is there little transmission of intraseasonal wave energy through the Indonesian passage (Fig. 3.11a), yet there is enhanced intraseasonal sea level variability in the Indonesian seas, along the western Pacific boundary and south of Java (Fig. 3.11c)? Note that the turning latitudes for Rossby waves with periods less than 60 days are equatorward of 10°S (Potemra 2001) and the Lesser Sunda Islands prevent these waves from entering the southern Indian Ocean. A spectral peak of 40-80 days is found for the SSHA south of Java (9.5°S-14.5°S, 95°E-115°E; not shown). Within this period range, a majority of the energy is blocked from entering the southern Indian Ocean. Only a small portion of signals with periods longer than 60 days is possibly transmitted into the Indian Ocean (Fig. 3.11f).

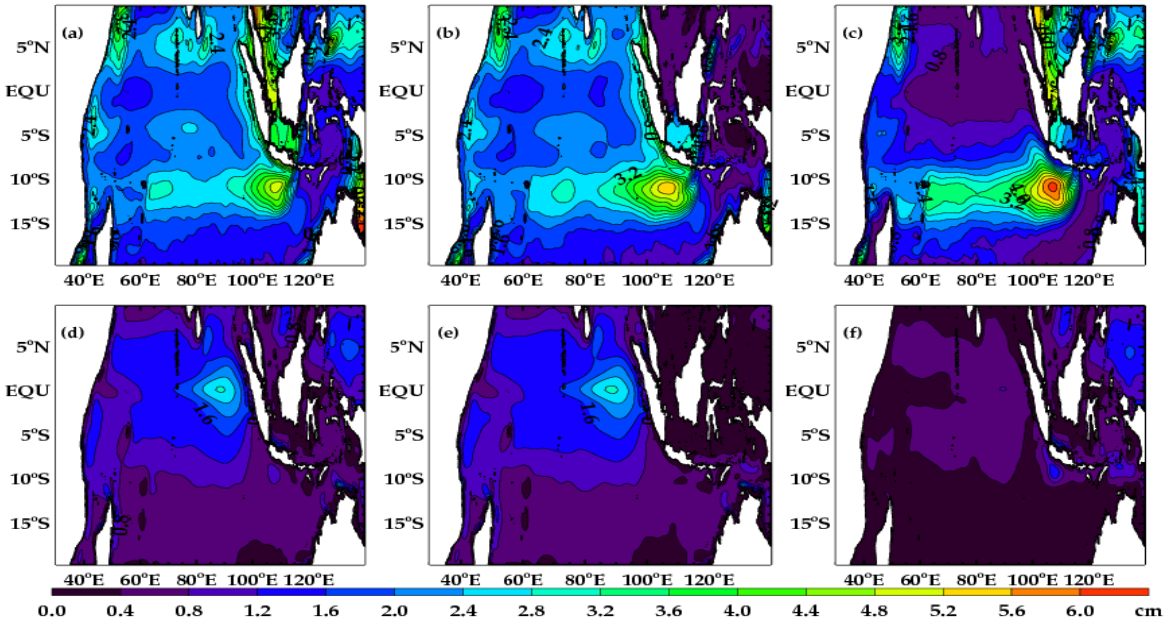

Figure 3.11: The STD of intraseasonal SSHA (cm), which is obtained by bandpass filtering the detrended and demeaned SSH to 28-105 day periods for the 1970-2001 period from (a) HYCOM-INDOPAC, (b) HYCOM-IND, and (c) HYCOM-DIFF; (d) Same as (a) but for the LOM-INDOPAC, where SSHA is computed as the sum of the first 15 vertical modes; (e) Same as (d) but for the LOM-IND; (f) same as (c) but for LOM-DIFF.

3.4 Indian versus Pacific forcing on ITF transport

While the ITF can affect the Indian Ocean, variability of the Indian Ocean can also modify the ITF volume transport. Existing observational and modeling studies suggest that variability of

the ITF volume transport is driven by the pressure difference between the Pacific and Indian Oceans (e.g., Wyrtki 1987), and winds over both equatorial Indian and Pacific Oceans contribute to the pressure difference and thus to the variability of the ITF. It has been found that annual variations of the ITF are associated with equatorial waves generated in the Indian Ocean (Clarke and Liu 1993; Masomoto and Yamagata 1996; Sprintall et al. 2008), whereas interannual variability of the ITF results primarily from the Pacific forcing (Clarke and Liu 1994; Bray et al. 1996; Meyers 1996; Potemra et al. 1997; England and Huang 2005; Fieux et al. 2005). Such that the ITF transport is weakened during El Niño in response to the lower sea level in the western Pacific (Wyrtki 1987; Clarke and Liu 1994; Meyers 1996; England and Huang 2005). On intraseasonal time scales, variability of the ITF can be caused by the remote wind variations in the equatorial Indian (Sprintall et al. 2000; Wijffels and Meyers 2004; Schiller et al. 2010) and Pacific Oceans (Cravatte et al. 2004; Qu et al. 2008).

Here, using controlled HYCOM experiments, we quantify the impacts of the Indian versus Pacific forcing on multi-time scale variability of the ITF. The standard deviation of the interannual ITF variability from HYCOM-INDOPAC is 2.48 Sv, comparing to 1.46 Sv from HYCOM-IND and 2.21 Sv from HYCOM-DIFF (Fig. 3.12a). The correlation coefficient is 0.47 between the HYCOM-INDOPAC and HYCOM-IND ITF, but is 0.82 between HYCOM-INDOPAC and HYCOM-DIFF. These results confirm that forcing over the Pacific Ocean has a larger influence on the interannual variability of ITF. In contrast, the combined Indian and Pacific Ocean forcing contribute to the ITF seasonal variability (Fig. 3.12b). The standard deviation of the seasonal ITF variability from HYCOM-INDOPAC is 1.02 Sv, comparing to 3.51 Sv from HYCOM-IND and 2.61 Sv from HYCOM-DIFF (Fig. 3.12b). The correlation coefficient is 0.91 between the HYCOM-INDOPAC and HYCOM-IND, but is -0.83 between

HYCOM-INDOPAC and HYCOM-DIFF. Note that even though the correlations are based on only 12 data points, they still provide us with information about the phase agreements. These results suggest that Indian Ocean forcing sets the phase in the seasonal cycle of the ITF, while the Pacific reduces the amplitude of these variations. On intraseasonal timescales, the correlation of ITF variability between HYCOM-INDOPAC and HYCOM-IND is 0.79, and between HYCOM-INDOPAC and HYCOM-DIFF is 0.55 (Fig. 3.12c). The standard deviation is 1.9 Sv for HYCOM-INDOPAC, comparing to 1.6 Sv for HYCOM-IND and 1.16 Sv for HYCOM-DIFF. Apparently, forcing over the Indian Ocean plays a larger role, however, the Pacific forcing is also significant.

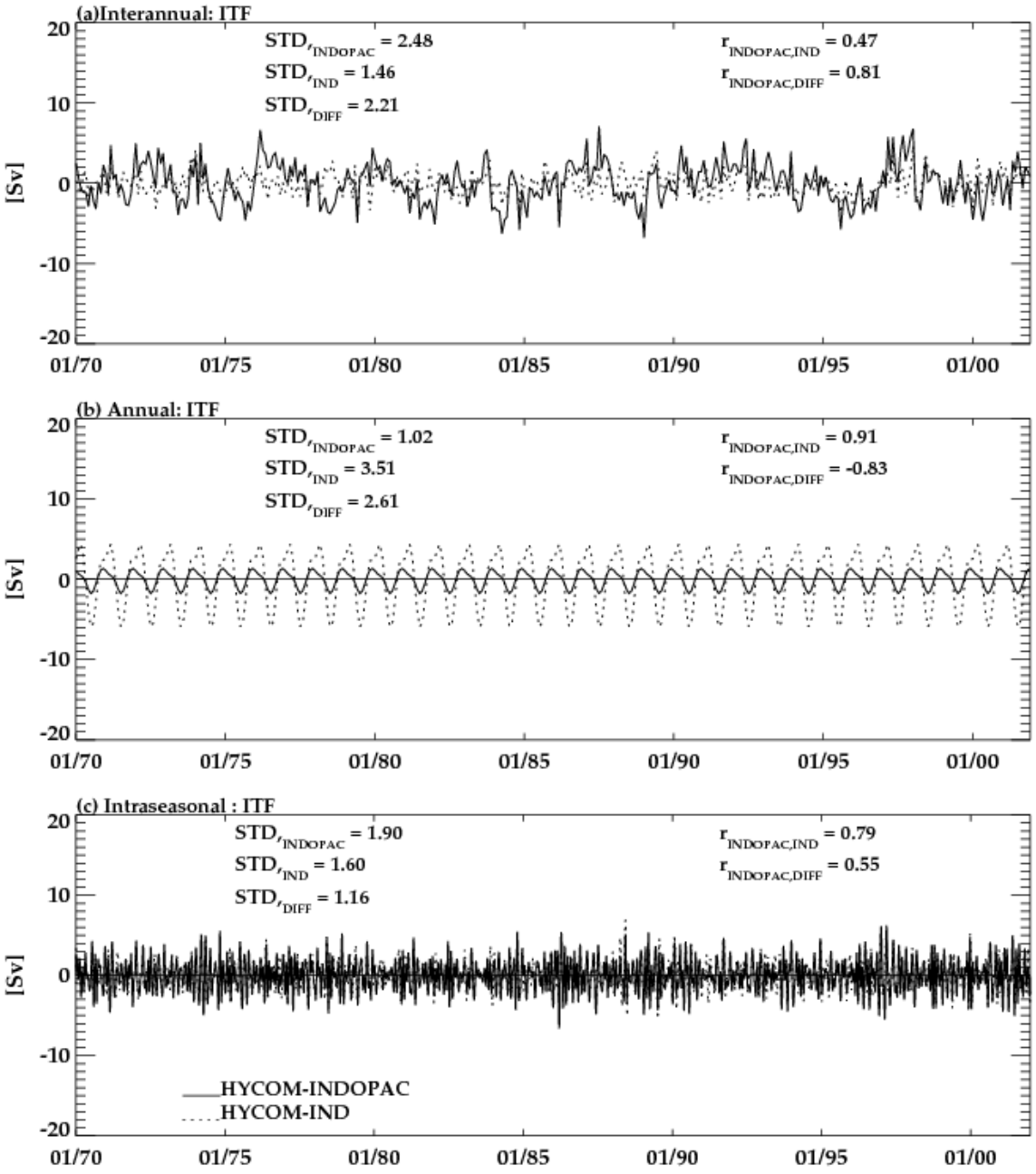

Figure 3.12: (a) Time series of monthly ITF volume transport (Sv) with the seasonal cycle removed from HYCOM-INDOPAC (solid) and HYCOM-IND (dotted) for 1970-2001; (b) Repeating seasonal cycle of monthly ITF volume transport, computed as the first three harmonics of the seasonal cycle for 1970-2001; (c) Same as (a) but for the 28 to 105 day bandpass filtered ITF. All anomalies are computed relative to the 1970-2001 mean.

3.5 Summary

The relative importance of local versus remote forcing on interannual-to-intraseasonal sea level and thermocline variability of the tropical south Indian Ocean is systematically examined by performing a suite of controlled experiments using an ocean general circulation model and a linear ocean model. Particular emphasis is placed on the Thermocline Ridge of the Indian Ocean (TRIO; 50^{o}E -80^{o}E, 5^{o}S-12^{o}S). On interannual and seasonal time scales, sea level and thermocline variability within the TRIO region is primarily forced by winds acting on the Indian Ocean. Interannual variability is primarily caused by westward-propagating Rossby waves forced by Ekman pumping velocities east of the region. Seasonally, thermocline variability over the TRIO region is induced by a combination of local Ekman pumping and Rossby waves generated by winds from the east. Adjustment of the tropical southern Indian Ocean at both time scales generally follows linear theory and is captured by the first two baroclinic modes. Remote forcing from the Pacific via the oceanic bridge has significant influence on seasonal and interannual thermocline variability in the east basin of the southern Indian Ocean, and weak impact on the TRIO region. On intraseasonal time scales, strong sea level and thermocline variability is found in the southeast tropical Indian Ocean, and it primarily arises from oceanic instabilities. In the TRIO region, intraseasonal sea level is relatively weak, and it results from Indian Ocean wind forcing. Forcing over the Pacific is the major cause for interannual variability of the Indonesian Throughflow transport, while forcing over the Indian Ocean plays a larger role in determining seasonal and intraseasonal ITF variability.

Chapter 4

Decadal variability

4.1 Background

4.1.1 Multi-decadal trend

Multi-decadal changes in the vertical structure of temperature in the Indian Ocean shows a complex pattern of near-surface warming accompanied by thermocline cooling in the tropical south Indian Ocean (Barnet et al. 2005; Pierce et al. 2006; Han et al. 2006, Alory et al. 2007, Trenary and Han 2008; Schwarzkopf and Böning 2011). This intricate pattern of temperature variability is consistent with the distinct spatial patterns of sea level trends found over the Indian Ocean since the 1960s, where the sea level drops in the southwestern Indian Ocean and rises elsewhere (Han et al. 2010; Timmerman et al. 2010; Schwarzkopf and Böning 2011; Hamlington et al. 2011; Dunne et al. 2012). Changes in the regional Indian Ocean Walker and Hadley Circulations, forced in part by heating of the Indo-Pacific warm pool, are argued to be the primary cause for the sea level pattern (Han et al. 2010). The changing winds manifest as strengthened westerlies in the equatorial Indian Ocean and the southeasterly trades in the subtropical southern Indian Ocean, which result in an increased upward Ekman pumping velocity over the southwestern tropical Indian Ocean (Han et al. 2006) and a spin-up of the subtropical cell (Trenary and Han 2008). The enhanced Ekman pumping shoals the thermocline, cools the subsurface and lowers the sea level. On the other hand, the thermocline cooling has also been attributed to reduction of the Indonesian Throughflow (ITF) transport after the 1976/77 climate shift (Alory et al. 2007; Wainwright et al. 2008). An ocean general circulation model (OGCM) forced by NCEP winds, which have an apparent reduction of strength in the equatorial Pacific near 1976/77 (Feng et al. 2011), also suggests significant ITF contribution (Schwarzkopf

and Böning 2011). The estimated ITF transport after 1977 using 14 global ocean data assimilation products, however, showed no apparent reduction (Lee et al. 2010*)*.

4.1.2 Decadal variability of SST, sea level, and upper ocean heat content

Overlying the multi-decadal trend, large-amplitude decadal variability has been observed for Indian Ocean sea surface temperature (SST), sea level, and upper ocean heat content. Decadal variability of Indian Ocean SST is often attributed to low frequency variations of ENSO and communicated to the Indian Ocean through the atmospheric bridge and changes in the ITF (Cole et al. 2000; Shi et al. 2007). Regional changes in the south Indian Ocean subtropical atmospheric circulation and decadal modulation of the Indian Ocean Dipole are also linked to decadal temperature variability (Allan et al. 1995; Reason et al. 1996; Ashok et al. 2004; Tozuka et al. 2007).

Satellite observed sea surface height (SSH) data documented large-scale decadal changes over the Indo-Pacific Ocean from 1993-2000 to 2000-2006 (Lee and McPhaden 2008; Feng et al. 2011). Sea level falls in the tropical southwestern Indian Ocean and rises in the eastern Indian Ocean for 1993-2000. The sign of the SSH trend reverses during 2000-2006. Upper ocean heat content, which is associated with variations of SST and thermocline depth, similarly shows a relatively large component of decadal variability superimposed on the long trends (Levitus et al. 2009; Palmer et al. 2009).

In the south Indian Ocean, sea level and thermocline depth variations can result from wind forcing, transmission of signals from the Pacific via the ITF, variations in the ITF temperature and salinity properties, nonlinearities of the oceanic system. The ocean response to wind forcing consists of a component driven by locally forced Ekman convergence or divergence at the surface, which in turn deepens or shoals the thermocline, and Rossby wave forced by

windstress curl from the east. It is also possible that Rossby waves forced by equatorial Pacific winds transmit through the Indonesian passage, with part of the energy radiating westward as Rossby waves equatorward of the turning latitude (McCreary and Kundu 1987), and part propagating poleward along the west coast of Australia as coastal Kelvin waves south of the turning latitude. Observations show a strong correlation between the SSH anomalies (SSHA) in the tropical western Pacific and along the northwestern coast of Australia (Wijffels and Meyers 2004; Feng et al. 2010, 2011).

4.1.3 Internal variability:

In addition to the oceanic variability forced by atmospheric forcing fields at the surface and from the ITF, oceanic variability can also arise from instabilities due to nonlinearity of the oceanic system. Previous studies reported the effects of oceanic internal variability in generating "intraseasonal timescale" variability near Somali coast, in the southwest tropical basin, and South Equatorial Current region of the Indian Ocean (e.g., Kindle and Thompson 1989; Woodberry et al. 1989; Tsai et al. 1992; Jochum and Murtugudde 2005; Feng and Wijffels 2002; Yu and Potemra 2006; Han et al. 2007; Palastanga et al. 2007; Ogata and Masumoto 2010, 2011; Trenary and Han 2012). Levels of high eddy kinetic energy found in the 20^{o}S-30^{o}S band of the southern Indian Ocean, undergo large seasonal and interannual variations, resulting from varying vertical shear of the South Indian Counter Current-South Equatorial Current system (e.g., de Ruijter et al. 2004; Palastanga et al. 2007; Jia et al. 2011). It remains unclear, however, how oceanic instabilities affect decadal variability of Indian Ocean SST, sea level and thermocline.

At latitudes greater than 20 degrees, generalized theory links instability of baroclinic Rossby waves with eddy generation (LeCasce and Pedlosky 2004; Isachsen et al. 2007). The absence of large scale westward propagating SSH anomalies and the chaotic structure of the

higher latitude SSH field is indicative of this response (See Chelton and Schlax 1996). Theoretically, mesoscale eddy activity has also been associated with self-sustained intrinsic variability of the mid-latitude gyres (Dijkstra and Ghil 2005 and references therein). Idealized quasi-geostrophic simulations attribute the robust decadal variability of the gyre system to mesoscale eddy activity (e.g. Schmeits and Dijkstra 2001; Berloff et al. 2007).

4.2 Present Research

In this study, we investigate decadal variability of the temperature structure, its relation to sea level and thermocline variability, and their causes since the 1970s. Specifically, we examine the relative contributions of atmospheric forcing over the Indian Ocean, remote forcing from the Pacific via the ITF, and oceanic instabilities. To achieve these objectives, a suite of sensitivity experiments is performed using an ocean general circulation model.

4.3 Results

In this section, we first compare HYCOM solutions with AVISO SSHA, WOD05 and SODA data (section 4.3.1). Then we find the dominant patterns of decadal variability of temperature (section 4.3.2), and assess the contributions from forcing over the Indian Ocean, remote forcing from the Pacific via ITF and oceanic instabilities to the spatial patterns of decadal temperature, sea level and thermocline depth anomalies (section 4.3.3). Finally, we will examine the causes for decadal phase reversal of SSHA before/after 2000 (section4.3 3.4).

4.3.1 Model and data comparisons

4.3.1.1 Decadal variability of temperature

The vertical structure of the multi-decadal temperature trends show the largest cooling occurs in the vicinity of the thermocline (5^{o}S-17^{o}S between 100 to 300m) in the subtropical

southern Indian Ocean (Barnett et al. 2005; Han et al. 2006; Pierce et al. 2006; Alory et al. 2007; Trenary and Han 2008). A time series of the anomalous interannual (Fig. 4.1; thin lines) and 8-year lowpass filtered (thick lines) temperature anomalies from INDOPAC, SODA, and WOD05 is constructed for the maximum cooling region. All datasets show consistent decadal variability, with cool phases during 1970-1974, 1981-1985, and 1993-20 and warm phases during 1975-1980 and 1986-1992. The correlation coefficient between HYCOM and WOD05 is ~0.6 at both interannual and decadal time scales. HYCOM solution shows less agreement with SODA data, with correlation of 0.48 for interannual variability and 0.54 for the 8-year lowpassed decadal variability. There are, however, some notable differences in the timing of the cooling/warming phase transitions and in the amplitudes. For example, the warm phase begins in 1975 and the amplitude is larger in HYCOM. Cold phase during 1981-86 is stronger and during 1993-2001 is weaker in HYCOM compared to the other two datasets. Despite these differences, HYCOM, WOD05 and SODA show general agreements in the evolution of subsurface decadal temperature variations.

To characterize the spatial structures of temperature anomalies, the periods of negative and positive phases shown in Fig. 4.1, are used to form vertical and horizontal sections of temperature anomalies. Latitude-depth sections (Fig. 4.2) show that the vertical structures of decadal temperature variability are complex in the tropical-subtropical Indian Ocean, with surface warming (cooling) often accompanied by subsurface cooling (warming). HYCOM results agree reasonably well with SODA data, and to a lesser extent with WOD05 data, despite HYCOM/WOD05 having a somewhat better agreement for the averaged anomalies in the maximum cooling region (Fig. 4.1). This is likely because of the inadequacy of data sampling issue of WOD05 data (Carson and Harrison 2008), which may not be adequate to resolve the

subsurface structure of temperature variability. Typically, the largest cooling and warming occur in the thermocline layer. To show the horizontal structures of temperature variability in the thermocline, we produce the temperature anomalies averaged from 100m-300m (Fig. 4.3). The horizontal structures are also complex. During some periods temperature anomalies of similar sign are basin-scale, at different times anomalies of one sign bound a region of oppositely signed anomalies in the 5^{o}S-12^{o}S band (Fig. 4.3). Again, HYCOM solution (Fig. 4.3, left column) agrees reasonably well with SODA reanalysis albeit with quantitative differences (middle column), and less with the WOD05 data (right column).

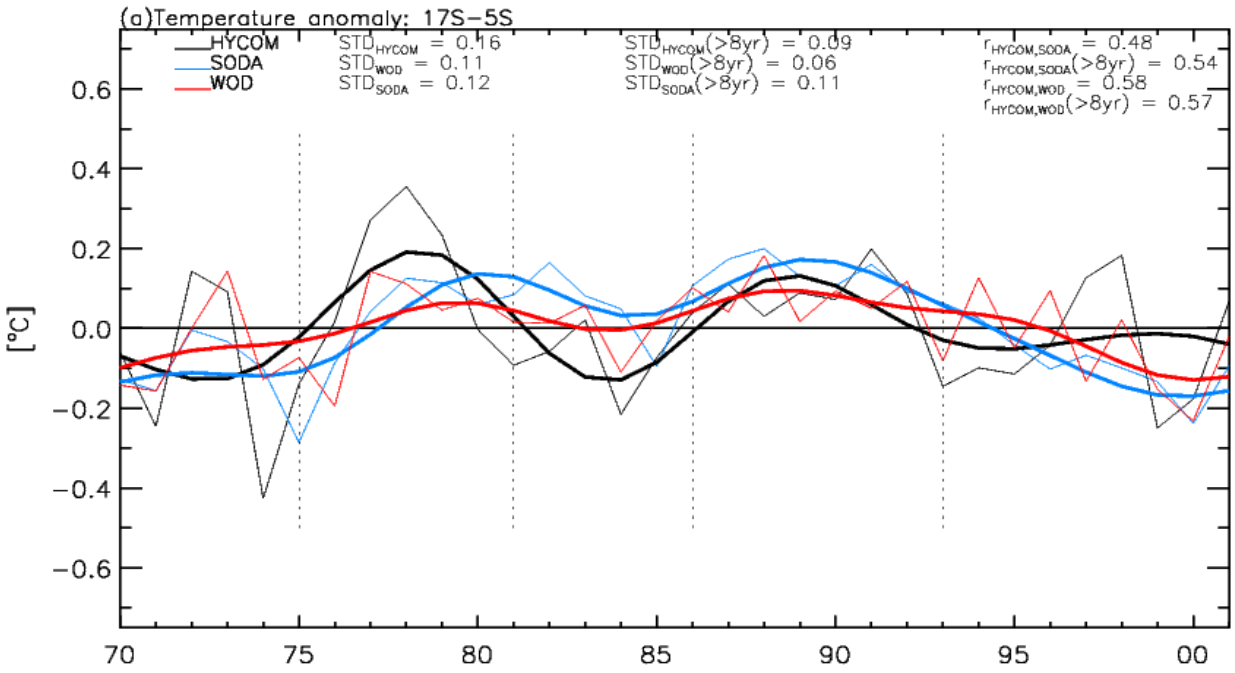

Figure 4.1: Time series of interannual temperature anomalies (detrended) averaged over (52^{o}E-75^{o}E, 5^{o}S-17^{o}S) between 100m-300m, which corresponds to the region of maximum cooling trend, from HYCOM-INDPAC (thin black), SODA (thin blue), and WOD05 (thin red),. The thick lines are the corresponding 8-year lowpass filtered time series and are used to identify the phases of the subsurface temperature variations. Periods of similar phases are indicated by the dotted vertical lines.

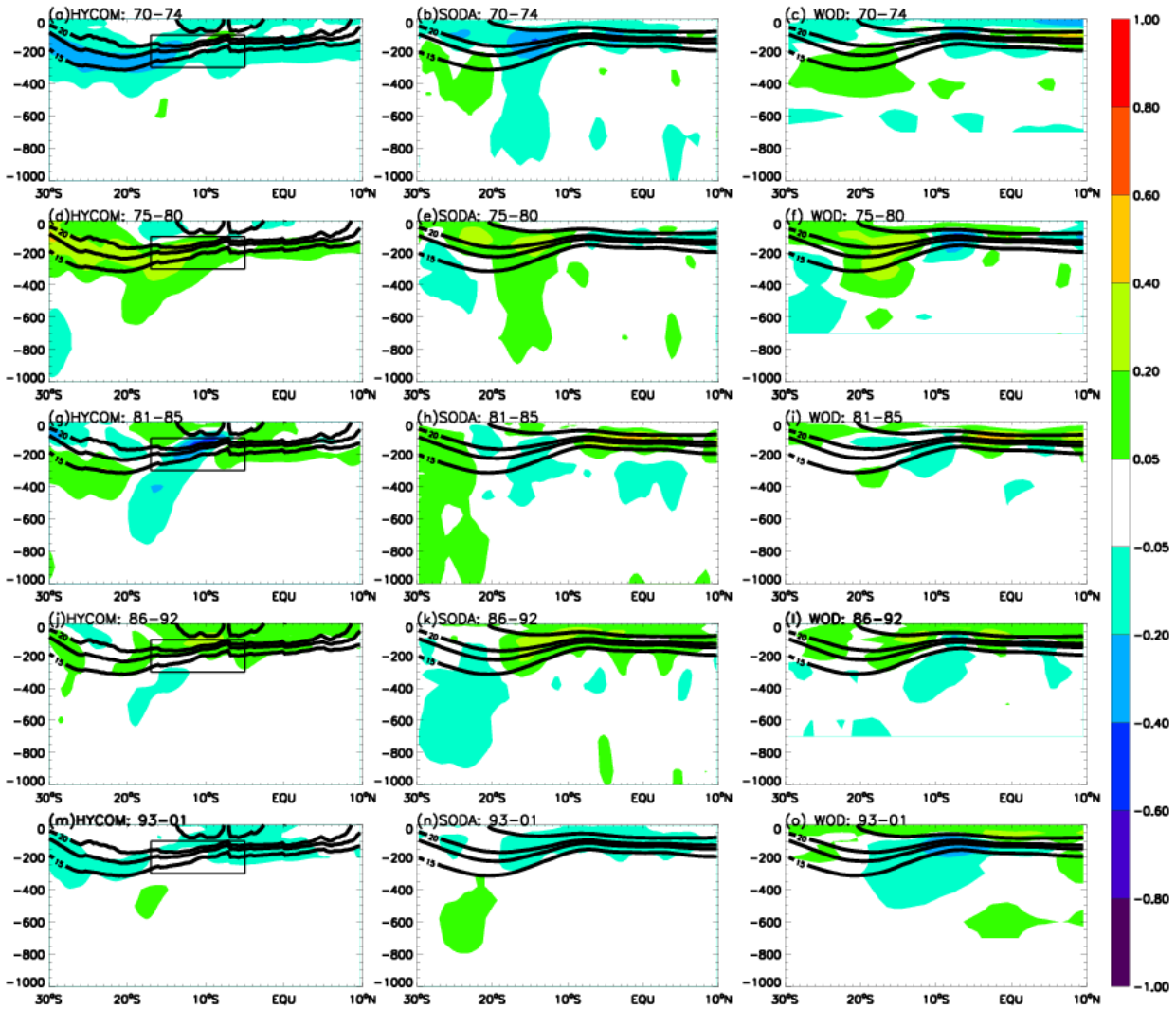

Figure 4.2: Decadal zonal mean temperature anomalies for HYCOM (left), SODA (middle), and WOD05 (right) for the periods 1970-1974 (top), 1975-1980 (second row), 1981-1985 (third row), 1986-1992 (fourth row), 1993-2001 (bottom). The decadal anomalies are computed from the detrended and demeaned annual temperature fields zonally averaged from 35^{o}E to the eastern boundary. The anomalies are then averaged over each period. Phase identification is based on Figure 2. The color contours show temperature anomalies and the line contours show depths of the 25, 20,18, and 15 ^{o}C isotherms.

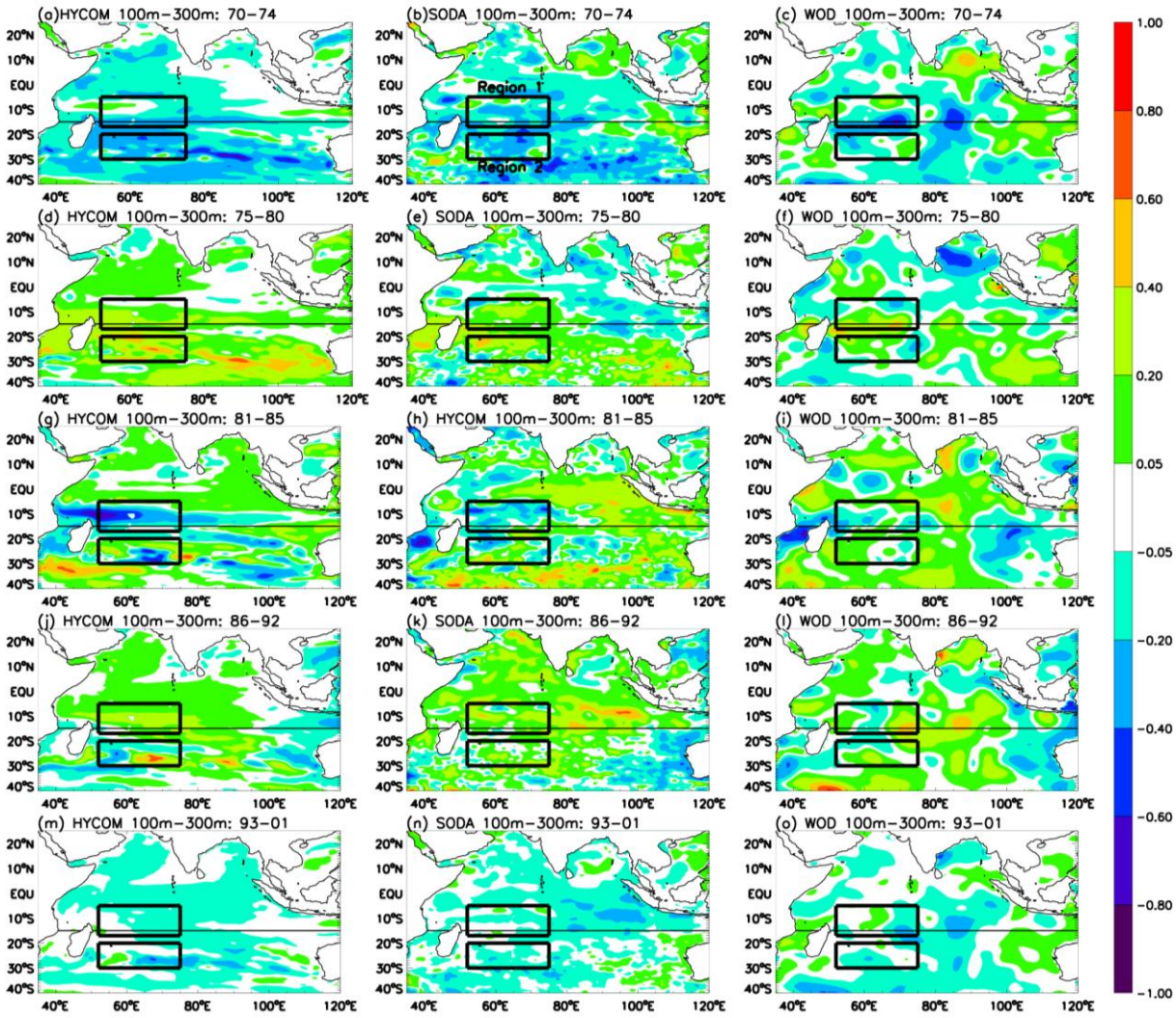

Figure 4.3: Mean temperature anomalies between 100m-300m for HYCOM (left), SODA (middle), and WOD05 (right) for the periods 1970-1974 (top), 1975-1980 (second row), 1981-1985 (third row), 1986-1992 (fourth row), and 1993-2001 (bottom). The decadal anomalies are computed from the detrended and demeaned annual temperature fields. The horizontal line marks the latitude of 15°S. The boxed region encloses (52°E-75°E, 5°S-17°S), and averaged temperature anomalies in the region are shown in Figure 2. Region 2 encloses (52°E-75°E, 20°S-30°S), which is used to form time series for Figure 4.5.

4.3.1.2 Decadal change of SSH

The observed basin-wide SSH trend patterns from 1993-2000 and 2000-2007, as well as the observed decadal phase reversal of the SSH trends near 1999~2000 (Lee and McPhaden, 2008) are successfully simulated by HYCOM, albeit with some quantitative differences in some

regions. For example, observations show more small scale structures in the SSH trends in south subtropical basin than HYCOM. High eddy activities have been documented in these regions (section 4.1.3), and the relatively coarse (1/3°x1/3°) horizontal grids of HYCOM may underestimate these eddies. The dominant pattern of SSH trend in the south Indian Ocean during 1993-2000 is rising sea level in the eastern basin accompanied by sea level drop in the interior, especially in the central and western south tropical basin (between 5°S-20°S extending zonally from 40°E-100°E; Figs. 4.4a-5c). A phase reversal is apparent from 2000-2007, with sea level trends essentially reversed in these regions. Similar patterns are also shown in SODA reanalysis data (Fig. 4.4c,f). HYCOM simulations, however, agree with AVISO SSHA as well as, or even better than, SODA data.

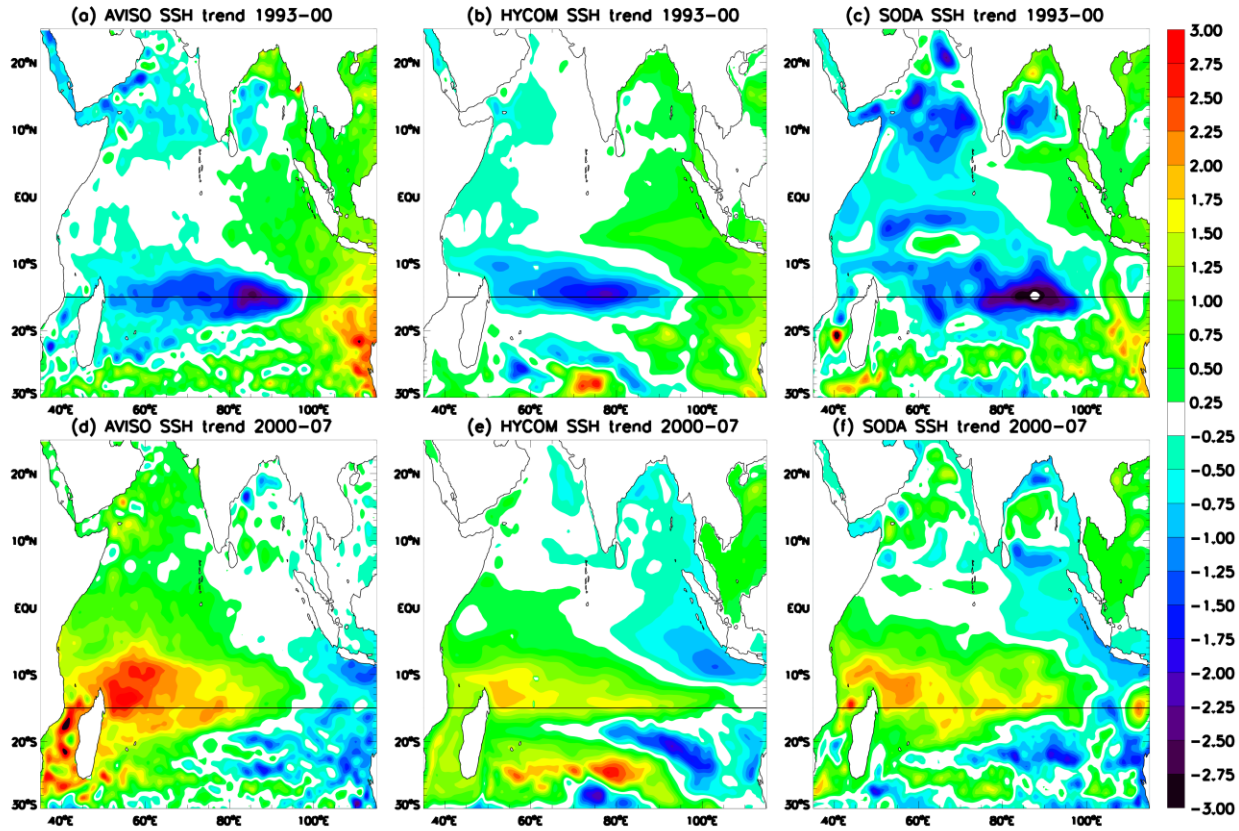

Figure 4.4: Linear trends in SSHA for the period 1993-2000 (top row) for (a) AVISO, (b) HYCOM, and (c) SODA-POP; (d)-(f) Same as (a)-(c) but for the period 2000-2007. Trends are given as cm yr^{-1}. The horizontal line marks the latitude of 15°S.

4.3.1.3 Relationship between SSHA, D20A, and subsurface temperature variability

One goal of this research is to understand the relative contributions of wind forcing acting on the Indian Ocean versus the impacts of a varying ITF on decadal variability of the temperature structure of the southern Indian Ocean. Large temperature variability primarily occurs in the thermocline (Fig. 4.2). To demonstrate the relationship between subsurface temperature variations and SSHA, we correlate the mean subsurface temperature anomalies between 100m-300m with SSHA, and then quantify the relationship between SSHA and D20A. The analysis is presented for both interannual and decadal anomalies. Decadal anomalies are obtained from the annual detrended and demeaned data and 8-year lowpass Lanczos digital filtering (Duchon, 1979). Two regions in the south Indian Ocean are selected for quantitative comparison: the first is for (52^{o}E-75^{o}E, 5^{o}S-17^{o}S) , which is Region 1 of Fig. 4.3, and the second, (52^{o}E-75^{o}E, 20^{o}S-30^{o}S), which is Region 2 of Fig. 4.3. In Region 1, both HYCOM and SODA subsurface temperature anomalies are strongly correlated with SSHA at interannual and decadal time scales, with correlation coefficients of 0.92 and 0.94 for HYCOM versus 0.95 and 0.94 for SODA (Fig. 4.5a). The HYCOM solution also shows strong correlations between SSHA and D20A, with correlations of 0.88 and 0.94 for interannual and decadal variability (Fig. 4.5b). SODA data show a lower SSHA/D20A correlation of 0.7 on decadal timescale, even though the correlation is higher (0.93) on interannual timescale. The strong correlations between SSHA and D20A, and between SSHA and subsurface temperature anomalies imply that baroclinic response of the ocean is important is causing subsurface temperature variability in the thermocline layer.

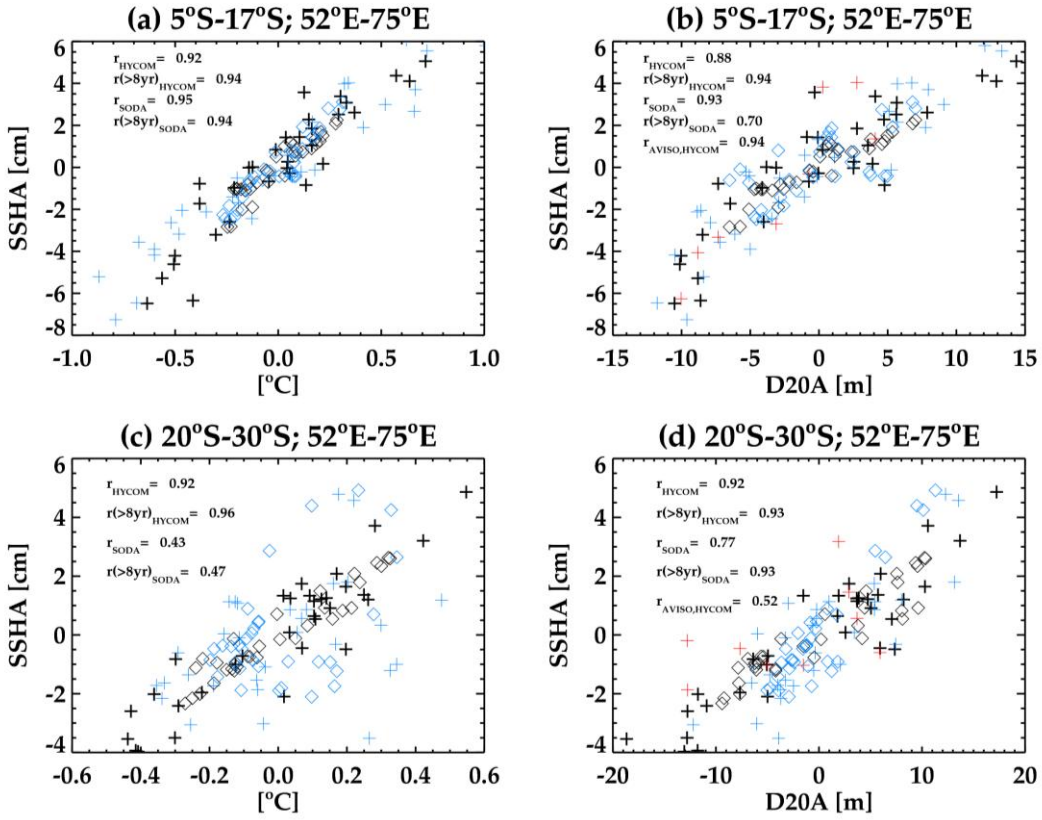

Figure 4.5: Scatter plots showing the relationship between the SSHA and thermocline (100m-300m) temperature anomalies averaged over (5°S-17°S, 52°E-75°E): (a) Black crosses are for interannual HYCOM solutions for the period 1970-2001, black diamonds represent 8-year lowpass filtered anomalies, blue crosses are for interannual SODA data for the period 1970-2001, and blue diamonds are the 8-year lowpassed SODA data; (b) Same as in (a) but for SSHA and D20A; The red crosses represent interannual SSHA from AVISO for the period 1993-2001; (c) Same as (a) but for the region (52°E-75°E, 20°S-30°S); (d) Same as in (b) but for the region (52°E-75°E, 20°S-30°S).

Interannual variability of D20 from HYCOM is in good agreement with AVISO SSHA, with a correlation of 0.94 (Fig. 4.5b). The correlations between HYCOM SSHA and subsurface temperature variations remain strong in Region 2 (Fig. 4.5c), but weakens substantially for SODA. Similarly, the correlations between SSHA and D20A remain strong in HYCOM and SODA, while the correlation between HYCOM D20A and AVISO SSHA drops to 0.54. The correlation between SODA SSHA and subsurface temperature anomalies is considerably weaker in Region 2, indicating that processes other that vertical movement of the thermocline contribute to subsurface temperature variations in the reanalysis product.

4.3.2 Dominant spatial patterns of decadal temperature variations

To obtain the dominant vertical structures of decadal temperature variability, EOF analysis is performed for the 8-year lowpassed zonal mean temperature anomalies during 1974-1997 from HYCOM solutions. Even though the period is short for decadal variability, the leading vertical structures of temperature variability from solutions INDOPAC and IND (Figs. 4.6a-b) show very similar patterns and account for 43% and 48% of the variance, respectively. Much of the variability occurs in the upper 300m and near the surface, with the maximum amplitudes occurring in the main thermocline (~200m) and near the surface within 15^{o}S-5^{o}N of the tropics. This pattern shows large temperature variability in the main thermocline, the in-phase relationship between the thermocline and the near-surface temperature anomalies, and the presence of oppositely signed anomalies below 200m south of ~15°S. These features were shown in the vertical structures of warm/cold phases of decadal temperature variability during 1986 to 2001 (Figs. 4.2j-k and 4.2m-n). This is consistent with the fact that the principle component of EOF1 (PC1) of INDOPAC is in phase with the identified decadal phase reversals for the 1986-2001 period (Fig.. 4.6d). During 1974-1985, PC1 of HYCOM-INDOPAC has a 90° phase shift compared to the temperature variability shown in Fig. 4.2. Consequently, the opposite phase relationship between the surface and ~200m shown in Fig. 4.2 is not reproduced by EOF1. Rather, it is dominated by EOF2 (Fig. 4.6e), as shown by the in-phase relations between the PC2 of HYCOM-INDOPAC and the phase reversals indentified earlier (Fig. 4.6h). These results are intriguing, and indicate that evolution of the vertical structures of decadal temperature variability varies for different decades.

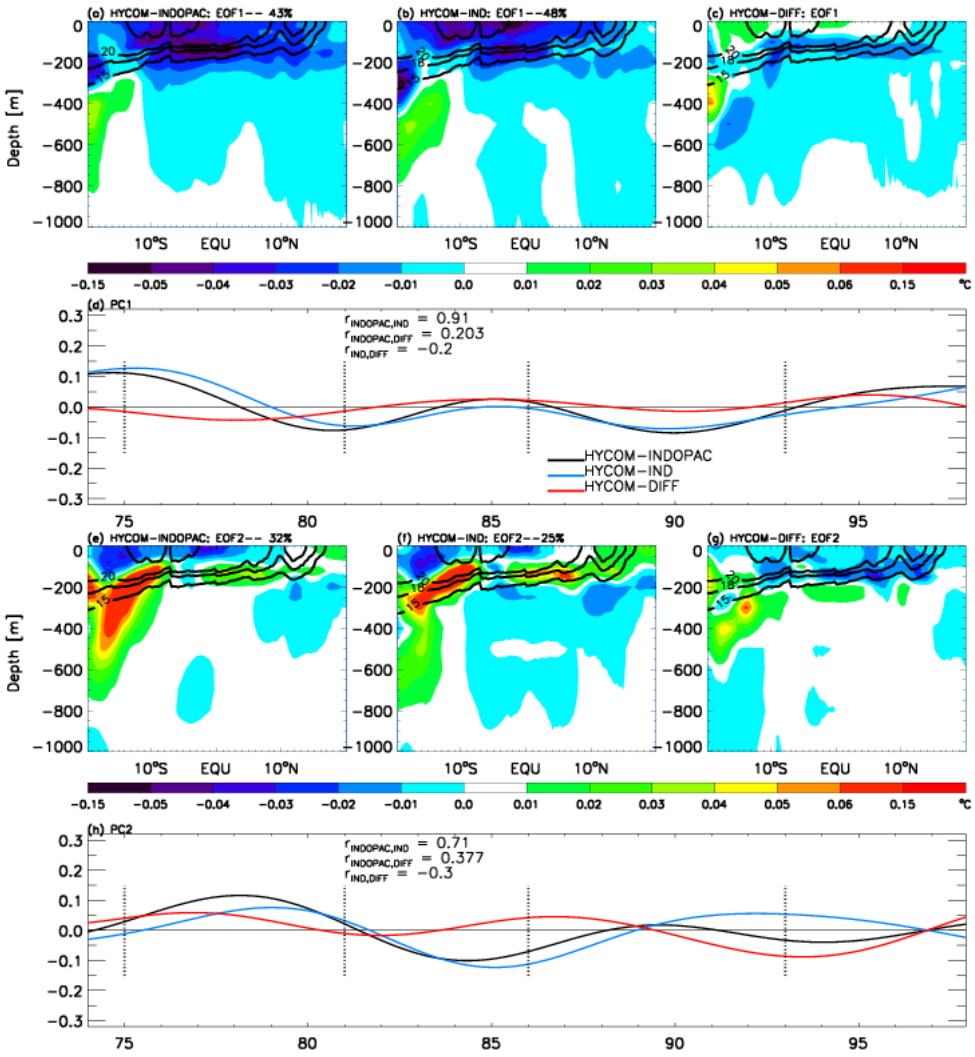

Figure 4.6: The first leading EOF (EOF1; top) and associated principle components (PC1; panel d) for 8-year lowpassed zonal mean temperature anomalies using the detrended and demeaned annual temperature during 1974-1998 from HYCOM-INDOPAC (a), HYCOM-IND (b), and the difference between HYCOM-INDOPAC and HYCOM-IND (c). Panels (e)-(h) are the same as in (a)-(c) but for EOF2. The first and last 4 years are removed prior to EOF analysis to remove contamination of results from filter's endpoints. The vertical dotted lines denote the periods of phase changes identified in Figure 2. The lined contours in a-c and e-g show depths of the 25, 20, 18, and 15 ^{o}C isotherms.

Both the EOF1 and EOF2 patterns from INDOPAC are well reproduced by the IND solution, demonstrating the dominant role of surface wind forcing over the Indian Ocean in determining the vertical structures of decadal temperature variability. Their PC1s also exhibit consistent temporal evolutions, with a correlate of 0.91 (Fig. 4.6d). Their PC2s are also highly correlated, with a correlation coefficient of 0.71. Contribution from the Pacific via the ITF,

which is represented as the difference (HYCOM-DIFF = INDOPAC – IND), has the largest influence in the tropical (north of 15^{o}S) thermocline (100~200m) and apparent contributions in the subtropical south Indian Ocean (Figs. 4.6c and 4.6g). The correlation between the PC1s of INDOPAC and DIFF is 0.20, and between the PC2s is 0.38. The dominant effects of forcing over the Indian Ocean on the vertical structures of zonal mean decadal temperature variability are also evident by directly comparing the temperature anomalies from solutions INDOPAC and IND (Fig. 4.7). While the EOF1 structure dominates the periods of 1986-1992 and 1993-2001, the EOF2 pattern is more accurately captures temperature structure during 1975-1980 and 1981-1985.

Even though forcing over the Indian Ocean plays a dominant role in determining the vertical structures of decadal temperature variability, contributions from the ITF are equally important in the thermoline layer (100-300m) of the tropical basin south of the equator, and also likely in the upper 600m of the subtropical south Indian Ocean (Fig. 4.7, right column). Note that in the subtropical southern Indian Ocean, eddies are active (see section 4.1.3) and thus oceanic instabilities may contribute to the decadal temperature variability there. As shown by Fig. 4.8, decadal internal variability has significant influence on decadal temperature structures in the southern subtropical Indian Ocean.

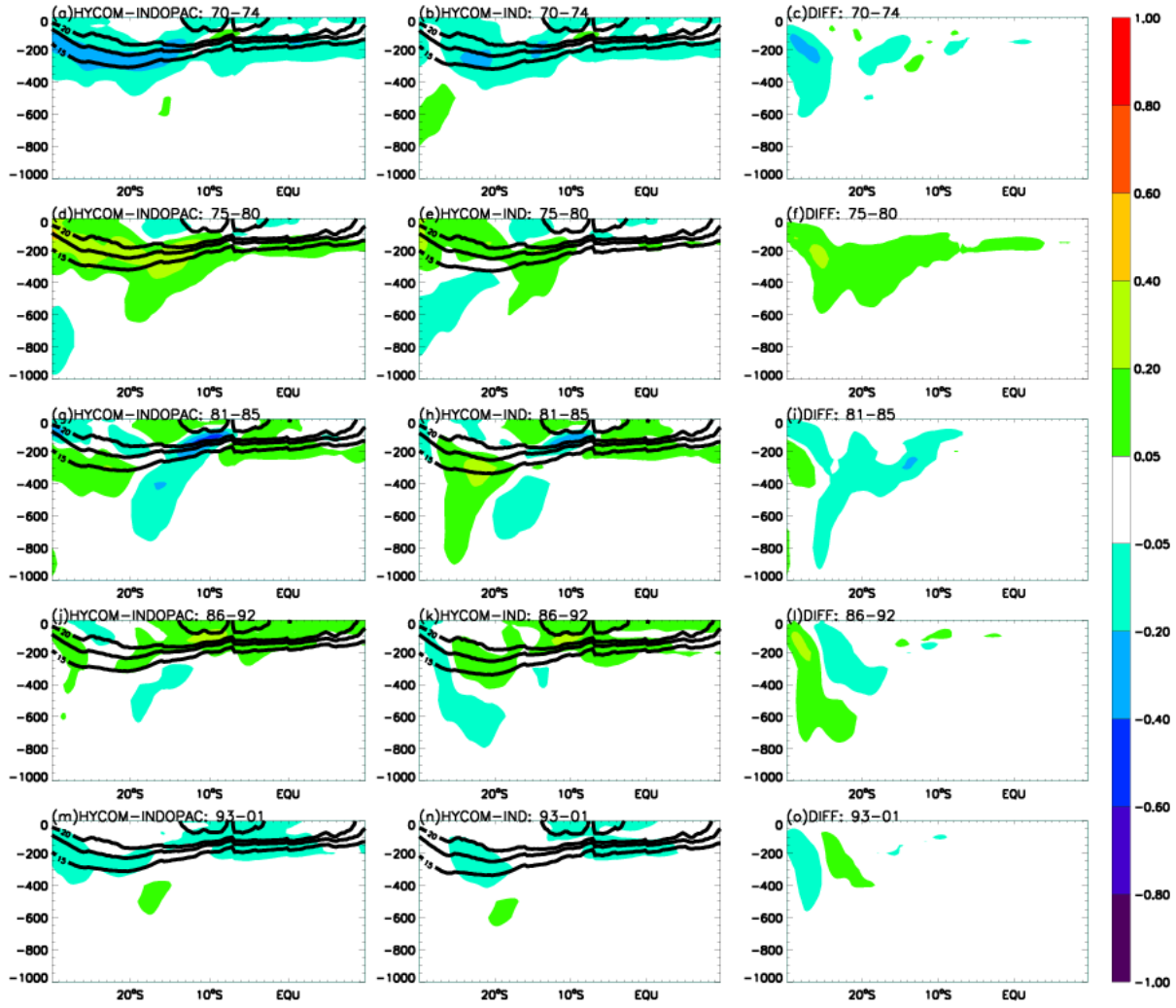

Figure 4.7: Decadal zonal mean temperature anomalies from HYCOM-INDOPAC (left), HYCOM-IND (middle), and HYCOM-DIFF (right) for the periods 1970-1974 (top), 1975-1980 (second row), 1981-1985 (third row), 1986-1992 (fourth row), 1993-2001 (bottom). The decadal anomalies are computed from the detrended and demeaned annual temperature anomalies. The zonal-mean temperature fields are averaged over each period. The color contours show temperature anomalies (^{o}C) and the line contours show depths of the 25, 20,18, and 15 ^{o}C isotherms.

Given that decadal temperature variability is large in the thermocline, and forcing over the Indian Ocean and the ITF have comparable influence there, we examine the horizontal structures of temperature variability in the thermocline (Fig. 4.9). Consistent with Fig. 4.7, north of the equator, decadal temperature variability is dominated by forcing over the Indian Ocean, with contributions from the ITF being much weaker. In the tropical south Indian Ocean (0-15^{o}S), forcing over the Indian Ocean dominates the maximum cooling in the southwestern basin, while

the ITF explains the cooling in the eastern basin (Figs. 4.9g-4.9i). In the subtropical south Indian Ocean (south of 15^{o}S), effects of forcing over the Indian Ocean (IND) and that of solution DIFF have comparable amplitudes. As mentioned above, solution DIFF measures the Pacific influence via ITF; meanwhile, it also contains the effects of oceanic instabilities, which are strong in the subtropical region (Fig. 4.8). Results obtained from the eddy permitting HYCOM-Climatology experiment forced by the monthly climatologies of forcing fields show relatively large decadal variability in D20A and SSHA between 20^{o}S-30^{o}S, with greatest variations found in the vicinity of the subtropical gyre accompanied by a secondary region of enhanced variability extending westward from the Australian coast (Fig. 4.10b-c). The oceanic internal variability also affects upper ocean temperature in the 20 ^{o}S -30 ^{o}S subtropical basin especially east of 80^{o}E (Fig. 4.10a). While small in amplitude, the internal variability of SST may affect the basin-wide SST pattern, and thus feedback to the atmosphere to affect atmospheric circulation. Restoring boundary conditions are active along 35 ^{o}S and may have some influence on the solutions near 30 ^{o}S.

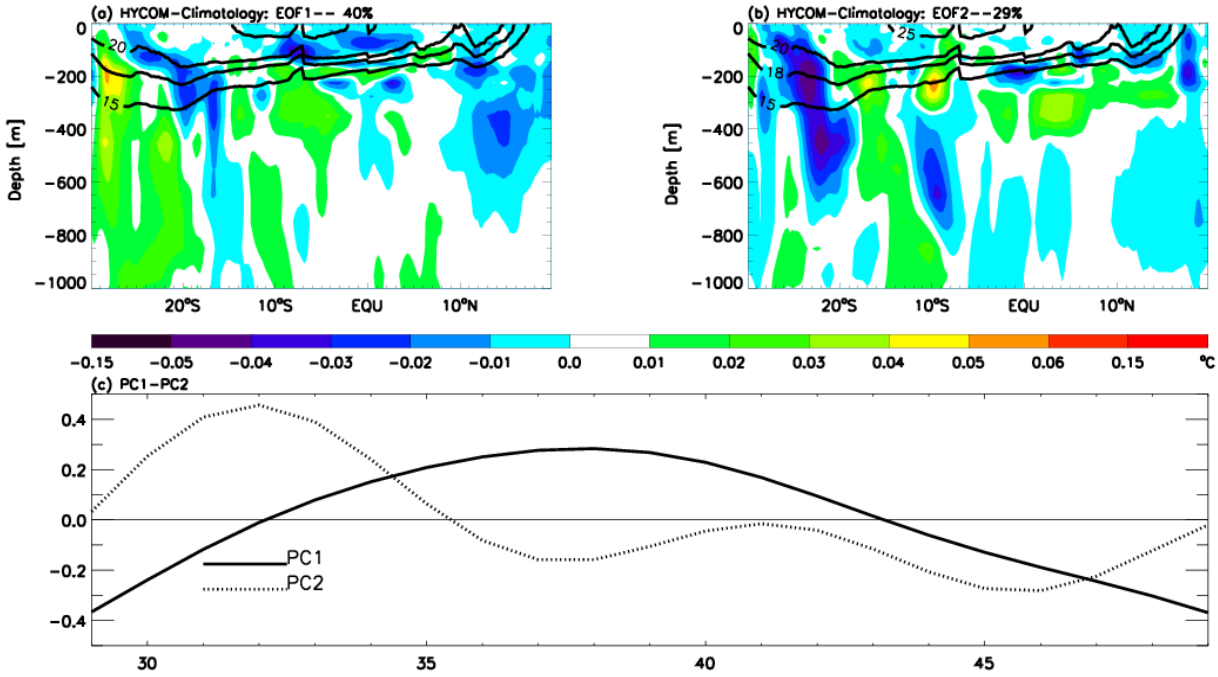

Figure 4.8: The first (EOF1; a) and second (EOF2; b) leading EOFs and associated principle components (PC1 and PC2; panel c) for 8-year lowpassed zonal mean temperature anomalies using the detrended and demeaned annual temperature from the HYCOM-Climatology run for years 20-59. The lined contours in a-c and e-g show depths of the 25, 20, 18, and 15^{o}C isotherms.

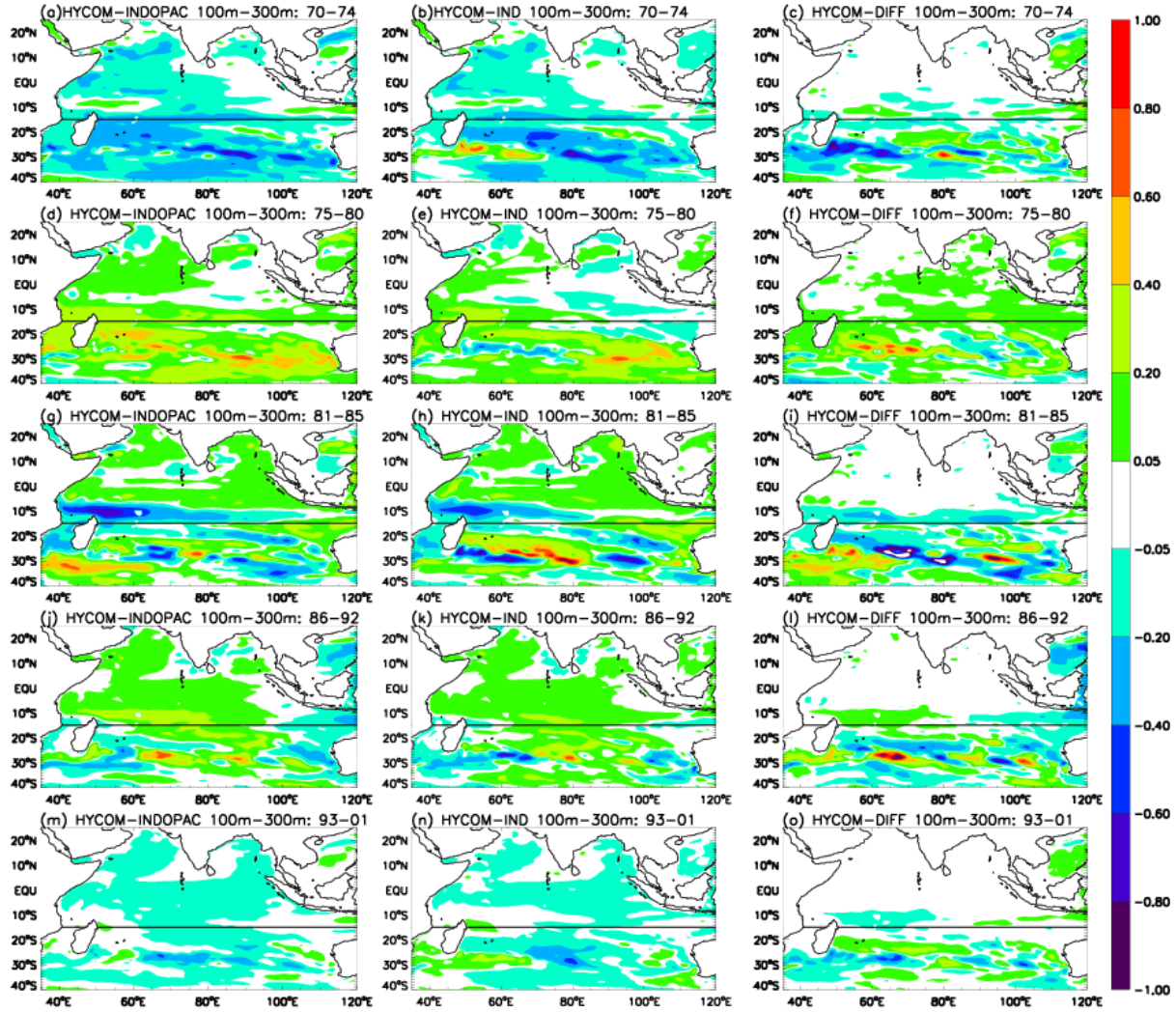

Figure 4.9: Horizontal structures of temperature anomalies in the thermocline (100m-300m mean) from HYCOM-INDOPAC (left), HYCOM-IND (middle), and HYCOM-DIFF (right) averaged for the periods of 1970-1974 (top), 1975-1980 (second row), 1981-1985 (third row), 1986-1992 (fourth row), and 1993-2001 (bottom). The decadal anomalies are computed from the detrended and demeaned annual mean temperature fields. The horizontal line in each panel marks the latitude of 15^{o}S.

4.3.3 Dynamic processes contributing to temperature variations in the thermocline

Interannual and decadal temperature anomalies in the thermocline are linked to vertical movement of the thermocline, as shown by the high correlations between the temperature anomalies and D20A (Fig. 4.12). Further, the amplitudes of the subsurface temperature anomalies (100m-300m), SSHA, and D20A tend to increase towards the west within the latitude

band 5°S-12°S and 20°S-30°S (Fig. 4.11), which may indicate oceanic adjustment process that involves westward-propagating Rossby waves.

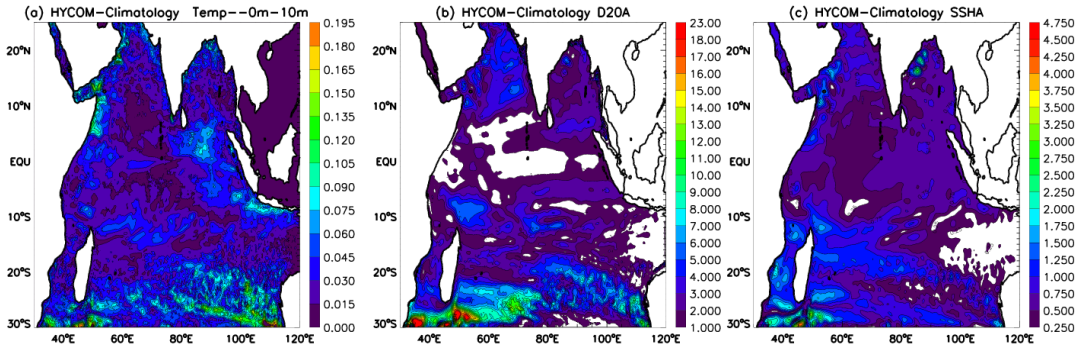

Figure 4.10: Standard deviation maps of the 8-yr lowpassed surface temperature anomalies °C (0m-10m; a), (b) D20A in m, and (c) SSHA in cm for HYCOM climatology run from year 20 to 59. The regions of enhanced variability indentify areas strongly impacted by oceanic internal variability.

In the tropical southern Indian Ocean, displacement of the thermocline can be forced by local Ekman pumping and Rossby wave propagation. In turn, the Rossby waves may be associated with the thermocline anomalies along the eastern boundary–either caused by local alongshore wind or the ITF-or large scale windstress curl acting on the ocean interior. On decadal timescales, after the westward propagating waves have passed, the ocean reaches Sverdrup balance. The simplest description of wind induced thermocline variability is contained in the longwave approximation of the linear vorticity equation using a 1½ layer reduced gravity model:

$$h_t + c_r h_x = w_e \tag{4.1}$$

where h is the thermocline depth anomaly, x is the distance from the eastern boundary and w_e the Ekman pumping velocity, defined as:

$$w_e = \nabla \times \left(\frac{\hat{\tau}}{\rho \hat{f}} \right) \tag{4.2}$$

The phase speed of a long Rossby wave is $c_r = -\beta c^2 f^{-2}$, where c is the baroclinic mode speed, f is the Coriolis parameter and β its meridional derivative. Variations of thermocline depth (refer to Eq. (4.1)) are driven by Ekman pumping velocity at a previous time along the wave path and local Ekman pumping. If the Rossby wave speed is slow, the ocean will adjust to the changing winds and the zonal integral of Ekman pumping velocity should lead the anomalies in the western basin. If the ocean has obtained a quasi-steady state, the term h_t is small and there is a direct relationship between the zonal integral of Ekman pumping and the east-west gradient of thermocline depth (h_w-h_e). The resulting expression is a baroclinic form of the Sverdrup relation.

The relative roles of regional Indian Ocean forcing versus the ITF on the southern Indian Ocean thermocline depth variability are inferred through comparison of the time series of zonal gradient of D20A from the INDOPAC and IND experiments. The difference between INDOPAC and IND provides a measure of the Pacific contribution to D20A, assuming that nonlinearity are not important. The relationship between the wind forcing and thermocline displacement will be determined through direct comparison of the zonally integrated Ekman pumping and the east-west gradient of thermocline anomalies.

Rossby wave phase speeds are dependent upon latitude and the oceanic background stratification. The first and second baroclinic mode speeds, estimated from the mean stratification of the southern Indian Ocean from INDOPAC are c_1=2.98 m s^{-1} and c_2 =1.67 m s^{-1}. Assuming the wave travels from the eastern boundary to 40^{o}E, the corresponding adjustment times at 10^{o}S, 20^{o}S, and 30^{o}S are ~1 year, ~3.7 years, and ~8 years, respectively. Adjustment times for the 2nd baroclinic mode Rossby wave at the latitudes 10^{o}S, 20^{o}S, and 30^{o}S are ~3year, ~12 years, and ~25 years, respectively. For decadal variability (>8years), D20A should be in quasi-equilibrium with the wind forcing and propagating signals should not be evident within the

5^oS-17^oS band. Indeed, longitude-time plots of D20A averaged within this latitude band show no apparent westward propagation (Fig. 4.13, top row). In the western and central basin, the evolution of the D20As within the 5^oS-17^oS band is similar for INDOPAC and IND, indicating that the thermocline variations primarily result from forcing over the Indian Ocean. Contributions from the ITF have the largest impact in the eastern basin. Zonal gradients of D20A (averaged within 5^oS-17^oS) from INDOPAC and IND are highly correlated (r=0.97), and they are essentially in balance with the 8-year lowpassed zonally integrated Ekman pumping velocity (Fig. 4.14a). Prior to the 1990's, the zonal-mean gradients of D20A are largely determined by the gradients in the western basin, which are forced by wind stress curl imposed upon the Indian Ocean, with the ITF contribution being weak. The ITF, however, dominates the Indian Ocean forcing in the eastern since the 1990s, and also the western basin from 1993-1997 (Figs 4.14c and 4.14e; the difference between the black and red curves estimate the ITF effect). The importance of ITF in shoaling the D20 during this period is also apparent in Fig. 4.13 (top-right panel). This shoaling of D20 results from the decadal weakening of the easterly trades in the equatorial Pacific (Fig. 4.15a). The subsequent enhancement of the easterly trades deepens the D20 in the eastern basin (Fig. 4.15a and top-right of 4.13). This D20 deepening, however, is much weaker than the D20A induced by the Indian Ocean winds in the ocean interior.

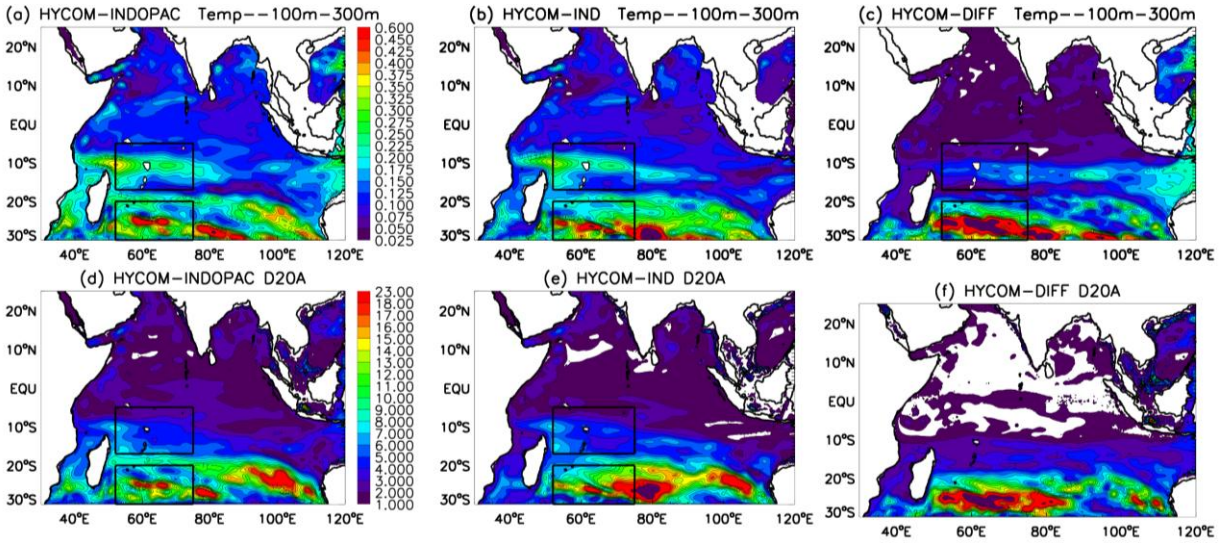

Figure 4.11: Standard deviation maps of the 8-year lowpassed average subsurface (100m-300m) temperature anomalies (top row) for HYCOM-INDOPAC (a), HYCOM-IND (b), and their difference (INDOPAC-IND; c). Figures (d)-(f) are the same as in (a)-(c) but for D20A. Figures (g)-(i) are the same as in (a)-(c) but for SSHA. The boxes show Region 1 and Region 2 of Figure 4.3, circumscribing the regions of greatest variability in the ocean interior. The relationship between subsurface temperature variability, D20A and SSHA in the boxed regions is presented in Figure 4.13.

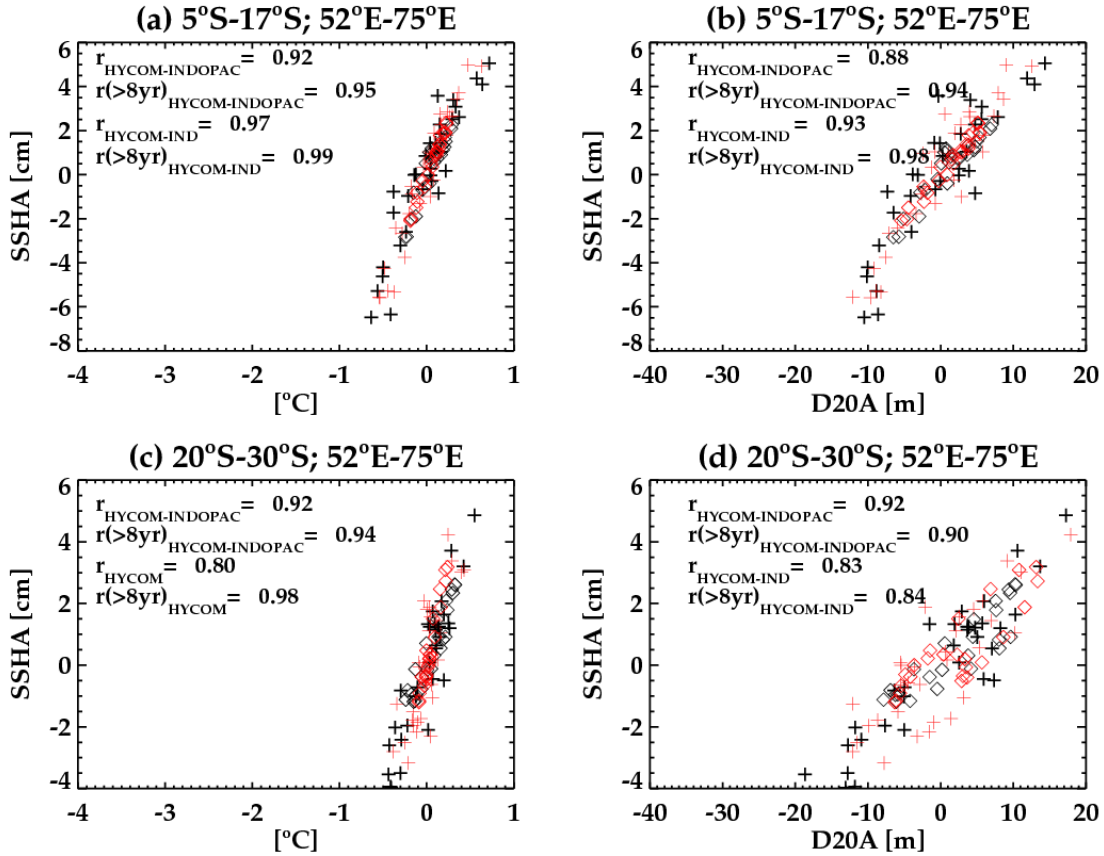

Figure 4.12: Same as Figure 4.6 but for scatter plots showing the relationships between SSHA, (100m-300m) averaged temperature anomaly, and D20A from HYCOM-INDPAC and HYCOM-IND.

In contrast to the tropics, westward propagation of D20A is apparent in the subtropical south Indian Ocean between 20^{o}S-30^{o}S (Fig. 4.13, bottom row). The amplitudes are weaker in solution INDOPAC than IND (Fig. 4.13, bottom-left and bottom-middle), and their difference shows significant amplitudes in the central and western basin (bottom-right). The differences between INDOPAC and IND, however, do not appear to have originated from the west coast of Australia, indicating that nonlinearities might be important (Fig. 4.10b-c). Correlation analysis between the zonally integrated Ekman pumping velocity and the zonal D20 gradient shows a good level of agreement for solution IND (r=-0.63). Apparent differences, however, exist (Fig. 4.14b). Similar correlation analysis for the INDOPAC solution is significantly reduced (r = -0.26; Fig. 4.14b). The westward propagating signals identified in both INDOPAC and IND appears to originate as anomalies along the eastern boundary (bottom-left of Fig. 4.13 and Fig. 4.14f). Excluding the early 1990s, the INDOPAC and IND solutions capture eastern boundary anomalies of similar magnitude and sign (Fig. 4.14f). The solutions begin to diverge around 80^{o}E. The apparent differences in the two solutions suggest the effects of instabilities: Rossby waves may go unstable (LeCasce and Pedlosky 2004). Further, the HYCOM-Climatology experiment solution indicates that thermocline depth variability on decadal timescale has large amplitudes west of 80°E (Fig. 4.10).

In the tropics, the largest difference between INDOPAC and IND occurs in the eastern basin (Fig. 4.13, top-right). In contrast, the greatest differences within 20^{o}S-30^{o}S are found in the central and western basin (Fig. 4.13, bottom-right). Moreover, eastern boundary D20As from INDOPAC and IND show good agreement prior to the 1990s (Fig. 4.14f), indicating the importance of direct forcing over the Indian Ocean in determining boundary conditions along western Australia. The model solutions differ considerably in the western basin for the same

period (Fig. 4.14d). These results suggest that oceanic instabilities associated with nonlinearities of the flow play an important role in affecting decadal variability of the thermocline in the subtropical southwestern Indian Ocean (Fig. 4.10). After the 1990s, D20A from (INDOPAC – IND) are significant, which is consistent with the evident ITF effects associated with the equatorial Pacific westerly wind anomalies as in the tropics (Figs 4.14e-4.14f).

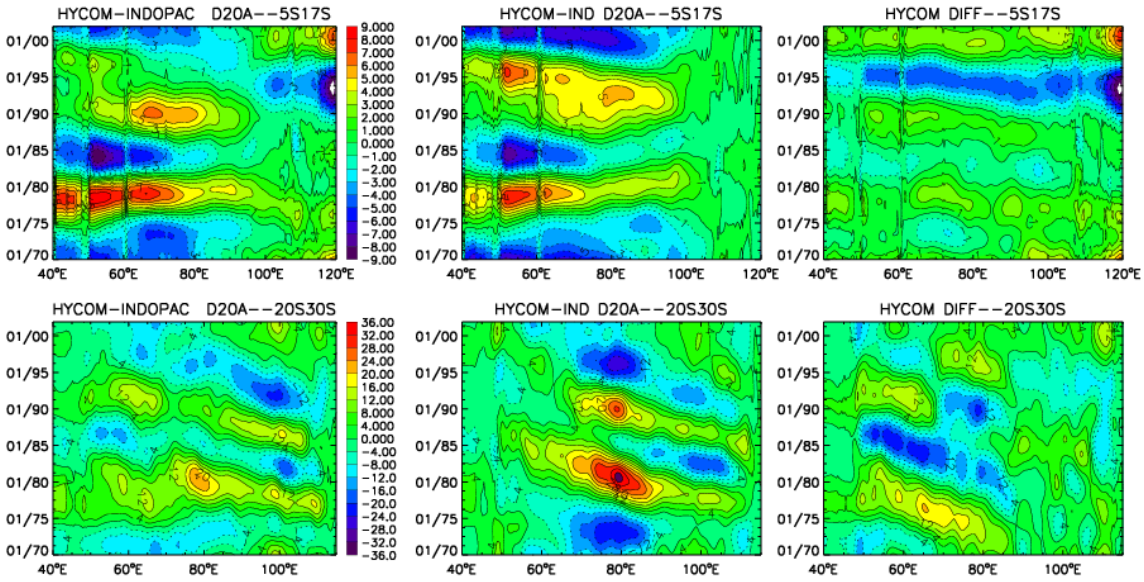

Figure 4.13: Longitude-time plots of the lowpass filtered (>8 yr) thermocline depth anomalies between the latitudes 5^{o}S-17^{o}S (top) and 20^{o}S-30^{o}S (bottom) from HYCOM-INDOPAC (left column), HYCOM-IND (middle column), and their difference (INDOPAC – IND; right column). Thermocline depth anomalies are represented by color and line contours with an interval of 1m. Negative values indicate a shoaling thermocline, and positive values a deepening thermocline.

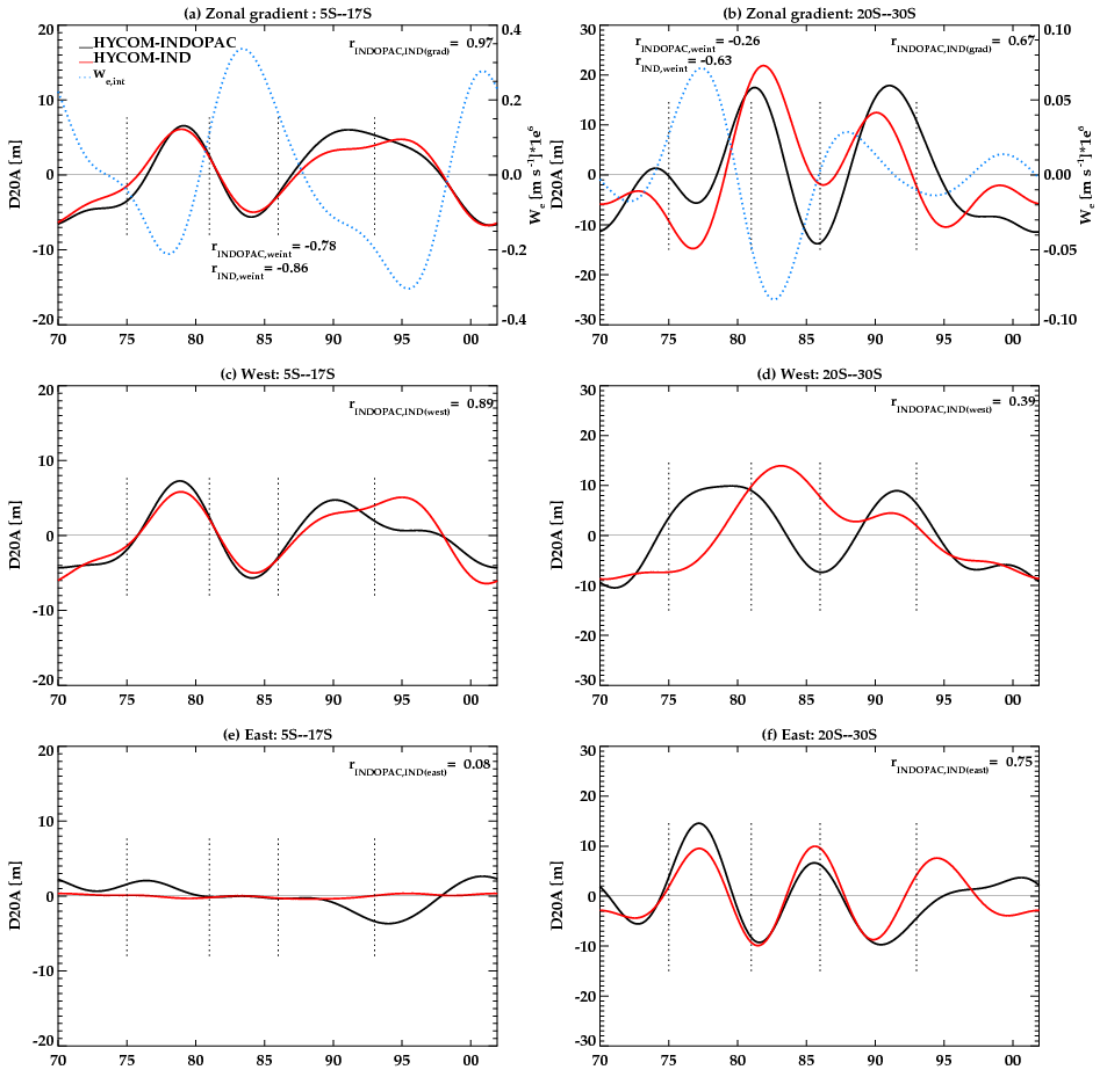

Figure 4.14: Time series of the lowpass filtered (>8 yr; thick lines) zonal gradient in thermocline depth anomalies (a) in the latitudes 5°S-17°S, and (b) 20°S-30°S from HYCOM-INDOPAC (black), HYCOM-IND (red), and the zonal integral of Ekman pumping ($w_{e,int}$; blue-dotted). The zonal gradient is determined as the difference in thermocline depth in the west (Figs. c-d) and east (Figs. e-f). Time series of the lowpass filtered western basin (52°E-75°E) thermocline anomalies for the latitudes 5°S-17°S (c) and 20°S-30°S (d). Eastern basin thermocline anomalies (105°E-115°E) in the latitudes 5°S-17°S (e) and 20°S-30°S (f). Periods of similar phase are indicated by the dotted vertical lines (see Fig. 4.1.) The difference between INDOPAC and IND estimates the ITF influence.

4.3.5 Decadal phase reversal of SSHA and D20A

Given that SSHA, D20A and thermcoline temperature anomalies are highly correlated on decadal time scales, here we examine the relative importance of forcing over the Indian Ocean and the ITF in causing the observed decadal phase reversal of SSH near 1999~2000 (Lee and

McPhaden 2008). Altimetry data shows a drop in sea level in the tropical southwestern Indian Ocean accompanied by rising sea level in the eastern Indian Ocean from 1993-2000 (Fig. 4.4a), a pattern similar to the 1961-2008 trend identified by Han et al. (2010). The sign of the SSH trend reverses during 2000-2007 (Fig. 4.4d). Our model results indicate that sea level fall and thermocline depth variations in the western tropical Indian Ocean are well described by Sverdrup balance and the impact of transmitted anomalies from the Pacific is relatively weak. Both the INDOPAC and IND experiments show similar sea level patterns and reversal in phase (Figs 4.16a-4.16b). The difference (INDOPAC – IND) demonstrates that the Pacific contribution to the decadal phase reversal of Indian Ocean sea level are generally weak, with significant amplitudes appearing near the eastern basin especially during the 1993-2000 period (Fig. 4.16c). Significant variability also occurs in the subtropical southern Indian Ocean, where oceanic instabilities can be important, as discussed above. Consistent with the south tropical Indian Ocean sea level fall from 1993-2000, a cooling trend appears in the thermocline and near the surface in the same latitude band (Figs 4.17a-4.17b). The sea level rise transmitted from the Pacific warms the thermocline region at the same latitudes, which reduces the Indian Ocean forced subsurface cooling (Fig. 4.17c). The phase reversal in SSH trends during 2000-2007 is related to warming throughout the tropic-subtropical thermocline. The patterns of zonal temperature trends are consistent with results obtained from EOF analysis: trends during 1993-2000 show remarkable agreement with EOF1, while the 2000-2007 trend is characteristic of EOF2 (Compare Fig. 4.17 and Fig. 4.6).

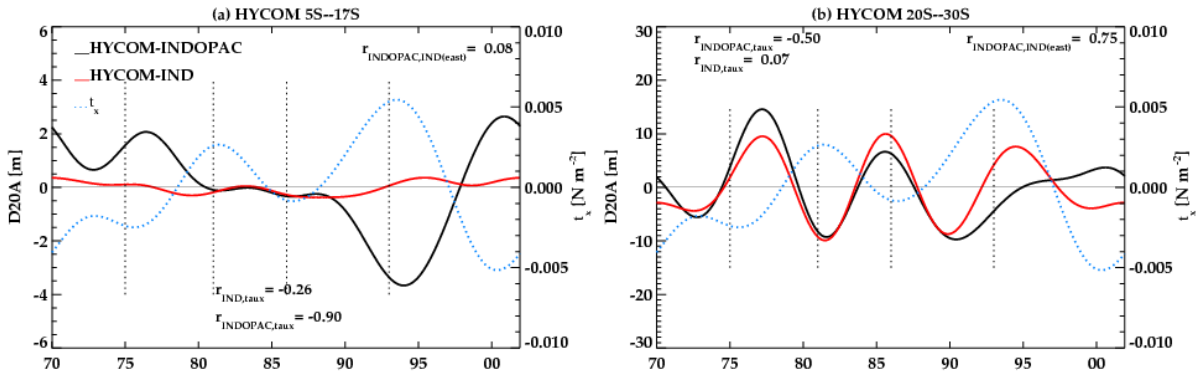

Figure 4.15: Time series of the eastern basin (105°E-115°E) thermocline anomalies (a) in the latitudes 5°S-17°S, and (b) 20°S-30°S from HYCOM-INDOPAC (black), HYCOM-IND (red), and the average equatorial (5°N-5°S ; 130°E-100°W) Pacific zonal wind stress (blue-dotted). Periods of similar phase are indicated by the dotted vertical lines (see Fig. 4.1.)

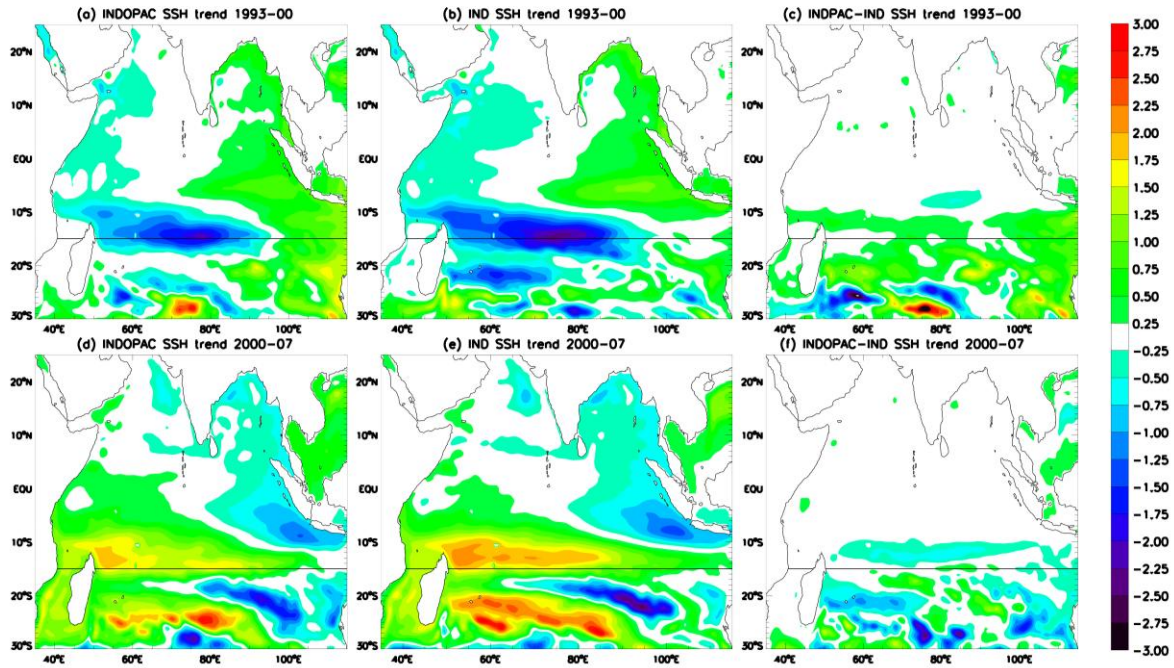

Figure 4.16: Linear trends in SSHA for the period 1993-2000 (top row) for (a) HYCOM-INDOPAC, (b) HYCOM-IND, and (c) INDOPAC - IND. (d)-(f) Same as (a)-(c) but for the period 2000-2007. Trends are given as cm yr^{-1}.

4.4 Summary

Analysis is performed on a set of diagnostic numerical experiments designed to isolate local versus remote oceanic influence from the Pacific on decadal variability of subsurface temperature, sea level and thermocline depth of the south Indian Ocean. It is found that the vertical structure of decadal temperature variability varies from decade-to-decade, with maximum variability peaking in the vicinity of the thermocline. The decadal scale temperature variations in the tropical southwestern Indian Ocean between 5^{o}S-17^{o}S are primarily associated with the vertical displacements of the thermocline. Prior to the early 1990s, decadal variations in sea level and thermocline depth can be described in terms of a baroclinic Sverdrup balance, forced by Ekman pumping velocity associated with windstress curl acting on the Indian Ocean. Beginning in the early 90's, decadal variability of the equatorial Pacific trades forces thermocline variations that modify the sea level and thermocline depth across the entire tropical southern Indian Ocean basin. Farther south, between 20^{o}S-30^{o}S, oceanic instabilities appear to make significant contributions to decadal variability of the thermocline. The anomalies along the western coast of Australia are primarily driven by regional forcing acting on the Indian Ocean prior to 1990s, and signals originating from the Pacific make a greater contribution thereafter.

Chapter 5

Multi-decadal variability

Observational evidence for the last few decades suggests that the world ocean is warming, with the strongest warming confined to the upper few hundred meters (Levitus et al., 2005). The vertical structure of the linear trend of oceanic heat content indicates that regions of cooling accompany the near-surface warming in both the Indian and Pacific Oceans (Barnett et al., 2005; Han et al., 2006; IPCC). In the Indian Ocean, maximum cooling occurs in the upper thermocline and attains the largest amplitude near 10^{o}S. Several climate models employed for the 20th century experiments of the Intergovernmental Panel on Climate Change (IPCC) documented similar thermocline cooling of the tropical-subtropical Indian Ocean (Barnett et al., 2005; Alory et al., 2007).

Attempts have been made recently to explain the development of the Indian Ocean subsurface cooling. Han et al. (2006) used a simple 2-layer equilibrium state model and suggested that cooling in the upper thermocline during 1960 - 1999 is primarily associated with anomalous upward Ekman pumping velocities. In contrast, Alory et al. (2006) suggests that cooling of the south Indian Ocean is remotely forced by a shoaling of the western Pacific equatorial thermocline, and is associated with decreased heat transport by the ITF. Other possible mechanisms may also cause thermocline anomalies: spin up or spin down of the subtropical cells (STCs; e.g., Liu, 1994; McCreary and Lu, 1994; McPhaden and Zhang, 2002), mid-latitude cooling/warming (Huang and Pedlosky, 2000; Boccaletti et al., 2004) and influence from the Antarctic Circumpolar Current (ACC). Eddy activity in the Southern Ocean has been shown to

shoal the thermocline in the Atlantic (Kamenkovich and Sarachik, 2004) and may have a similar effect in the southern Indian Ocean.

In this chapter, the long term variability of the subsurface Indian Ocean temperature, its relation to changes in the regional winds and the strength of the subtropical cells (STCs) are examined. This chapter begins with a brief summary which serves to characterize the spatial structure of the multi-decadal trends in temperature captured by a variety of datasets (Section 5.1). This is followed by a brief overview of the properties of the STC and a review of the STC theory (section 5.2). A detailed description of the structure of the shallow overturning cells of the Indian Ocean is provided in section 5.2.2. In Section 5.3, model results are presented which relate long term changes in the winds to variability of the Indian Ocean STC and Cross Equatorial Cell (CEC) strength, and the thermocline cooling. In section 5.4 the possible implications of these changes on climate are discussed. The principle findings are summarized in section 5.5

5.1 Structure of Multi-decadal temperature variations

A cooling trend in the tropical Indian Ocean thermocline for the period of 1961-2000 is shown in all four datasets, in addition to surface warming. Both the WOD05 and SODA-POP data (Figs 5.1a and 5.1b) show that the warming between 5^{o}N-15^{o}S is trapped to the surface and caps a region of thermocline cooling, with the strongest cooling mainly occurring above 200m, with the exception of SODA-POP data, which shows an additional region of strong cooling near 400m. Weaker cooling signals, found in SODA-POP, HYCOM, and POP-Hindcast, extend downward and southward at greater depths.

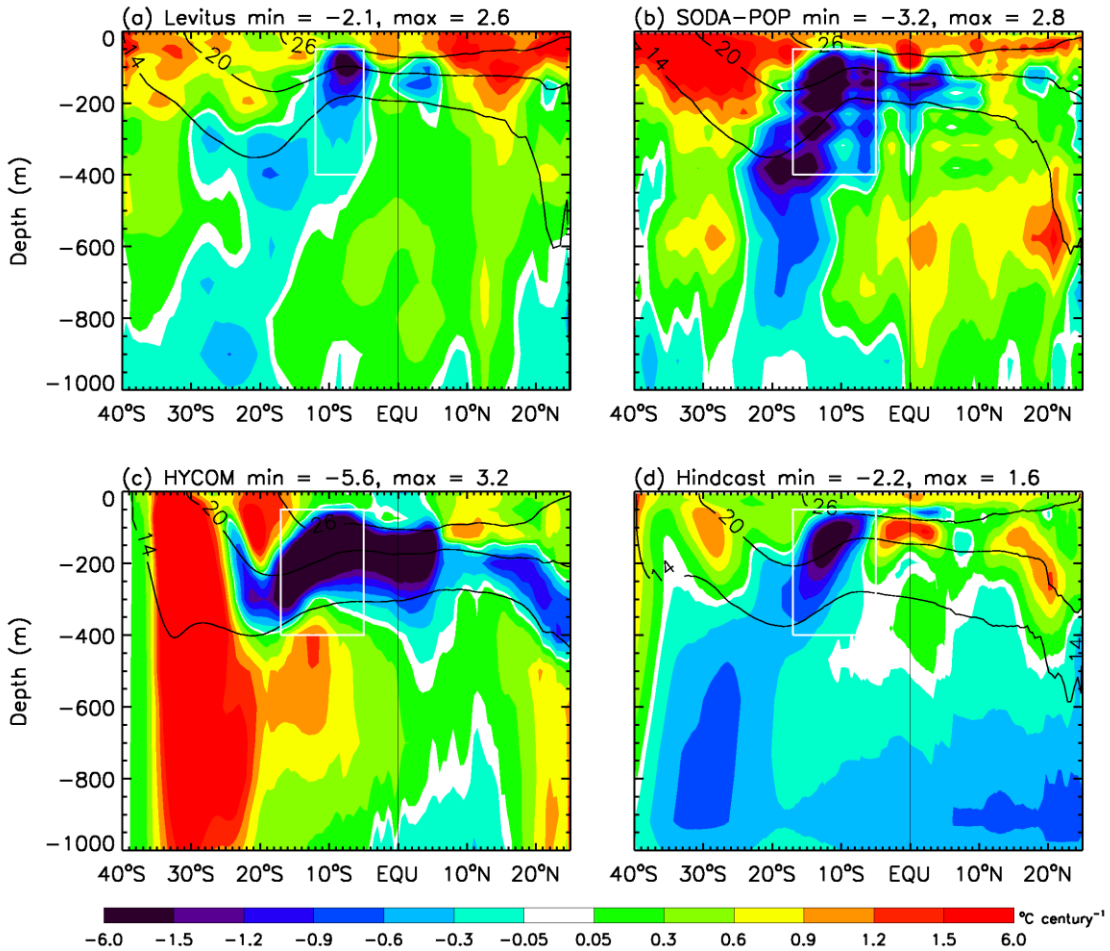

Figure 5.1: Latitude-depth plot of linear trend of temperature zonally-averaged over the Indian Ocean from (a) WOD05, (b) SODA-POP, (c) HYCOM, and (d) POP-Hindcast during 1961-2000. The black contours show the mean 26°, 20° and 14°C isotherms from the 1960's. White boxes are used to define trend indexes in Figure 5.2d.

HYCOM captures the strong cooling in the upper thermocline and the near-surface warming (Fig. 5.1c). The cooling region, however, shows little extent into the deeper ocean below 400m. Cooling in the north Indian Ocean is also stronger than the WOD05 and SODA-POP data. These model/data discrepancies are likely due to the artificial boundary at 40°S, which excludes the effects of ACC and may also affect realistic simulation of the ITF. POP-Hindcast also shows cooling of the upper thermocline south of the equator (Fig. 5.1d). Relative to WOD05 and SODA-POP data, the cooling extends too far south in the deeper layers. The lower thermocline cooling of the northern hemisphere also disagrees with the warming from other

datasets. Nevertheless, cooling in the thermocline above 400m is shown in both data and model solutions.

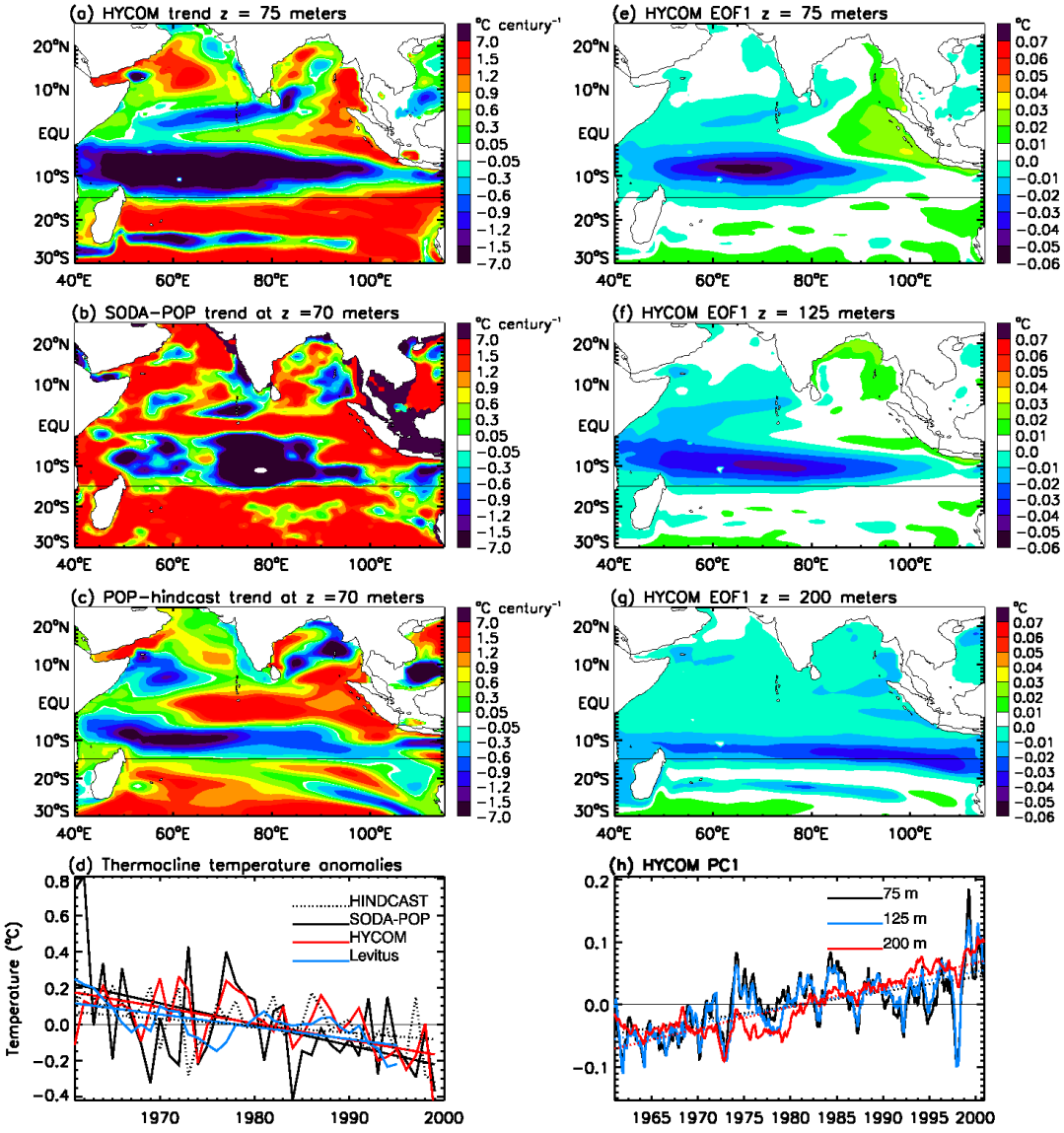

Figure 5.2: (a) Spatial pattern of temperature linear trend at 75m from HYCOM solution; (b) Same as a) except for SODA-POP temperature trend; (c) Same as a) except for POP-Hindcast temperature trend; (d) Time series of the thermocline temperature anomaly averaged over the cooling region (white boxes in Fig. 1) for WOD05 (blue), HCYOM (red), POP-Hindcast (dotted), and SODA-POP (black); (e)-(g) are the first EOF of temperature variability from HYCOM solution at 75m, 125m and 200m; (h) Time series of the principle component (PC) associated with the first EOFs at 75, 125 and 200m.

The spatial structure of the linear trend of temperature is illustrated in Figs 5.2a-5.2c for 70~75m from HYCOM, SODA-POP and POP-Hindcast. Albeit with quantitative differences, all data show a strong cooling trend south of the equator especially in the central-western basin, weaker cooling north of the equator in the central ocean and warming in the eastern tropical basin, a pattern that qualitatively resembles the Indian Ocean Dipole (IOD; e.g., Saji et al., 1999; Webster et al., 1999). The consistent thermocline cooling trends south of the equator from all datasets are also shown in Fig. 5.2d, which corresponds to a trend toward a negative IOD.

The dipole pattern is well captured by the first empirical orthogonal function (EOF1) of temperature variability (compare Figs 5.2e and 5.2a), and is also shown at 125m (Fig. 5.2f). The first 4 EOF modes explain about 37% of the total variance at 75 meters, with EOF1 accounting for 15%. At 125m, the first 4 modes explain about 45% of the total variance, with EOF1 accounting for 19%. The dipole pattern disappears at 200m, and the EOF1 shows a monopole structure (Fig. 5.2g). The principle components (PCs) for each of the leading EOFs (Fig. 5.2h) collectively show trends toward a cooling phase in the southern Indian Ocean, which again corresponds to a trend toward a negative IOD. It is also clearly evident that temperature in the upper-thermocline shows strong interannual-to-decadal scale variability (black and blue lines of Fig. 5.2h).

HYCOM solutions show that the strongest cooling in the central-western basin in the upper-thermocline extends eastward with the increase of depth, and appears to originate from the ITF region at 200m (Figs 5.2e-g). Linear trend of the 20^{o}C isotherm depth (D20) also shows weak connection with the ITF. Reduced heat transport associated with cooling of the western Pacific, appears to make a greater contribution in the lower thermocline and further south. However, a detailed heat budget of the upper Indian Ocean is beyond the scope of this work.

Analysis of WOD05 and SODA-POP data similarly indicate that shoaling of the Indian Ocean thermocline is greatest in the central-western basin, while POP-Hindcast solution shows a more pronounced connection to the ITF at all depths (not shown).

5.2 STCs: theory and structure

The subtropical cell is a shallow meridional overturning circulation confined to the upper 500 m of the ocean. In the Atlantic and Pacific, the cells are present in both hemispheres and the circulation connects the regions of subtropical subduction to the tropical upwelling. The surface branch of the cell is largely described by Ekman drift and the transport by the subsurface branch is in geostrophic balance.

Unlike the other major ocean basins, the Indian Ocean does not possess an equatorial upwelling zone. Rather, upwelling is found in the northern hemisphere off the African coast/Arabian Sea and in the open ocean of the tropical southern Indian Ocean. The subduction zone is in the southern hemisphere, consequently, the upper branches of the shallow overturning consists of a cross equatorial flow (CEC) and the southern Indian Ocean STC.

Because the lower branch of the STC supplies the cool subsurface waters needed to maintain the tropical thermocline, variations in transport by cell has been linked to climate variability.

5.2.1 Steady state model of the STC

The simplest model, which captures the existence, strength, and subsurface pathways, are captured by the 2 ½ layer model. The model has proved useful tool in constructing analytical solutions describing the basic structure of the STC (Luyten et al 1983; Pedlosky 1987, 1988, 1991; Pedlosky and Samuelson 1989; McCreary and Lu 1994; Lui 1994). In the aforementioned

studies, most of the analytical solutions are constructed for an open basin, and the strength of the equatorial circulation must be externally specific. McCreary and Lu (1994), using the same 2 ½ layer framework, constructed an analytical solution for the subtropical/tropical mass exchange in a closed basin. For this reason, the steady state theory provided in their study will be presented, as it provides a complete description of the STC.

The governing equations that describe the steady-state response of the STC are given as follows:

$$f\hat{\mathrm{k}} \times \vec{v}_i + \nabla p_i = \delta_{1i} \frac{\vec{\tau}}{h_i} \tag{5.1}$$

$$\left(h_i \vec{v}_i\right) = -(-1)^i w_i \tag{5.2}$$

Equation 5.1 is the steady state momentum equation, where *f* is the Coriolis parameter, $\hat{\mathrm{k}}$ is the unit vector in the vertical, $\vec{v}_i$ is the horizontal layer velocities, ∇p_i represents the horizontal pressure gradients, $\vec{\tau}$ is the wind stress vector, and h_i the layer thickness. δ_{i1} is the Kronecker delta function, with $\delta_{11} = 1$ and $\delta_{12} = 0$. The wind stress is introduced as a body force, acting only upon upper layer, the second layer is in geostrophic balance. Equation 5.2 is a form of the continuity equation, where w_1 represents the upwelling and downwelling branches of the STC, and allows for water transfer between the layers.

McCreary and Lu (1984) found the analytical solution to equations 5.1-5.2, for a rectangular basin (Fig. 5.1), bounded to the north at 50^o and to the south by the equator. The solutions are subject to the constraint that h_1 and h_2 are constant along the eastern boundary. Their model is forced by zonally independent wind field, i.e., $\vec{\tau} = \tau^x(y)$.

The dynamical regimes of the analytical solution obtained by McCreary and Lu (1994) are illustrated schematically in Figure 5.3. In Region 1 ($y > y_d$) entrainment and detrainment

processes work in concert to maintain a fixed depth in layer 1 ($h_1 = H_1$, where H_1 is constant). This layer behaves as a constant thickness mixed layer, in which water is instantly transferred between the layers. In region 2 (δ_e <y < y_d) both entrainment and detrainment are suppressed and $w_1 = 0$. Region 3 defines the upwelling boundary region; only entrainment is allowed to occur in this region. The boundaries of the northern and western frictional boundary currents are denoted by the lines y= y_n –δ_n and x = δ_w, respectively. Similar to Luyten et al. (1993), y_d denotes the ventilation latitude, and corresponds the latitude at which the $\nabla \times \left(\frac{\vec{\tau}}{\rho f} \right) = 0$.

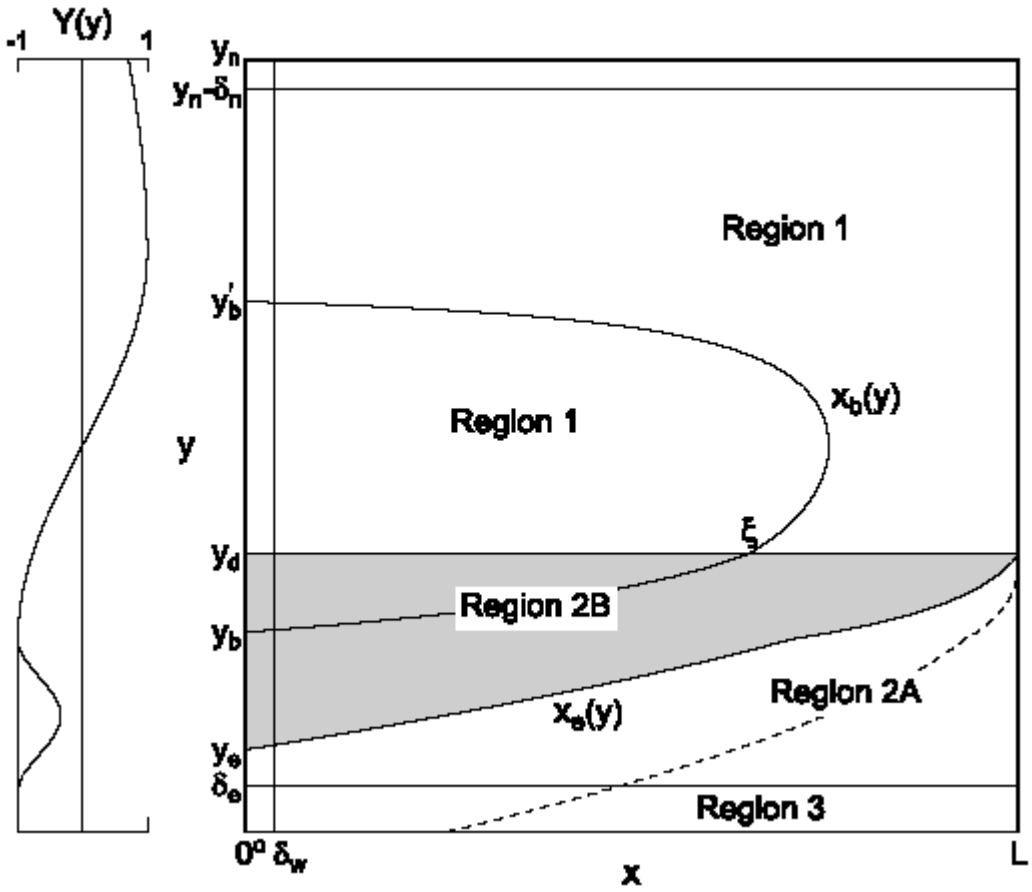

Figure 5.3: A schematic diagram illustrating the structure of the analytical solution of McCreary and Lu (1994). To the left are two zonal wind profiles. Image adapted from McCreary and Lu (1994).

5.2.2 Strength of the STC

Following McCreary and Lu (1994), it can be shown that the upper layer transport at the detrainment cut-off latitude can be expressed as follows:

$$M_1(y_d) = \int_0^L h_1(x,y) v_1(x,y) dx = -L \frac{\tau^x(y_d)}{f(y_d)} \left(1 - \frac{2H_1}{D + \sqrt{D^2 - 2L\tau^x(y_d) / g_{23}^1}} \right) \tag{5.3}$$

Equation 5.3 simply states that the meridional transport at y_d is partly determined by the Ekman drift (1st term on the right hand side of 5.3) and geostrophic flow (2nd term). The geostrophic flow always acts against the Ekman drift, but is relatively weak in comparison. Because region 2 is absent of any vertical motion (i.e. $w_1 = 0$), continuity require that transport everywhere in region 2 must be the same, $M_1(y_d) = M_1(y)$. Simply stated, $M_1(y_d)$ determines the strength of the upper branch of the STC. Further, continuity also requires that $M_2(y) = -M_1(y)$, so that the strength of the upper branch determines the strength of the return flow. In other words, the water removed from the tropics must be replaced by water from the subtropics. Amazingly, in a 2-layer model, the strength of the STC is determined only by the zonal wind stress at the detrainment cut-off latitude and is insensitive to changes in subtropical windstress curl.

The detailed solutions describing the subsurface flow will not be provided here. Rather, only a qualitative discussion of the subsurface equatorward flow is presented. The interested reader can refer to McCreary and Lu (1994). The negative Ekman pumping imposed on region1, forces water to be subduct and enter layer 2. According to equation 5.3 some portion of the water must flow past the latitude y_d. Some portion of the water will flow equatorward in the ocean interior, some portion recirculates in the subtropical gyre, and some portion moves equatorward through the low latitude western boundary current. The specific pathway taken by the subsurface

water is determined by the location of subduction relative the characteristic lower layer streamlines x_e and x_b (see Fig. 5.3). The line $x_e(y)$ divides region 2 into two dynamically distinct flow regimes. East of x_e (region 2A) the flow is stagnant and all motion is confined to the upper wind driven layer. Often referred to as the 'shadow zone' (Luyten et al. 1983), the constraint of constant layer thickness along the eastern boundary implies that the potential vorticity is not constant along the boundary and no streamlines can be emitted. As such, there is no motion in region 2A. To the west of x_e (region 2B), the flow is able to move equatorward either through the ocean interior, the pathway is depends upon the placement of water relative to the characteristic x_b. Subducted water to the west of x_b will recirculate in the subtropical gyre, while water to east participates in the STC. For flow to reach the equator the characteristic x_e, must intersect the equator. The interior pathway is more likely if the basin is larger and the subducted water comes from a shallower thermocline.

Sensitivity studies indicate that physics captured by the analytical solutions are robust and well represented in numerical models of varying complexity. Analysis of numerical solutions obtained from a constant temperature model and a thermodynamic model were found to be consistent with the analytical solutions. Specifically, the most significant result found in the constant temperature layer model is that the location equatorial upwelling is sensitive to the equatorial wind stress, while the strength of the upwelling is remotely determined by the zonal subtropical wind forcing. Results obtained from the thermodynamic model suggest that the lower layer temperature in the tropics is maintained by the advection of cool water by the STC.

5.2.3 Indian Ocean STCs

The Pacific and Atlantic oceans possess two STCs each, one in each hemisphere. The zone of equatorial upwelling serves as the rising branch of the cells and subduction occurs in the

eastern subtropics of each hemisphere. Because the Indian Ocean lacks persistent equatorial trades, the upwelling is located off the equator along the coasts of Somalia and Oman, near the tips of Indian, and within the open ocean between 5^{o}S-12^{o}S (Fig. 5.4). The regions of upwelling are associated with the ascending branches of the Cross Equatorial Cell (CEC) and the southern STC.

5.2.3.1 CEC

The upper branch of the CEC is driven by the southward cross-equatorial Sverdrup balance at an average rate of 6 Sv (Schott et al. 2004). In the proceeding theoretical discussion, it was noted that the strength of the STC is controlled by the zonal wind stress and the resulting Ekman drift. There appears to a contradiction in stating that the strength of the CEC is controlled by the Sverdrup transports, rather than Ekman drift. This is only an apparent contradiction. Because the zonal winds nearly disappear along the equator during the monsoons, it can be shown that the strength of the zonal winds is proportional to the distance from the equator and the Ekman pumping vanishes (Miyama et al. 2003). Consequently, there are no geostrophic currents and the fluid motion is entirely wind driven. Further, this implies that $-\frac{\tau_y^x}{\beta} = -\frac{\tau_y^x}{f}$ and the Sverdrup transport and Ekman drift are equivalent. Subduction of the water occurs in the southeast southern Indian Ocean (Fig. 5.4). The return flow is transported back to the northern hemisphere upwelling zones via the subsurface northward flowing Somali current. A schematic showing the meridional circulation of the CEC is shown in Fig. 5.3. Both observations (Schott et al. 2002) and modeling studies (McCreary et al. 1993l Miyama et al. 2003, Schoenfeldt and Schott 2006) have demonstrated that the CEC is primarily responsible for inter-hemispheric mass and heat exchange.

5.2.3.2 Southern STC

The ascending branch of the southern STC is associated with the upwelling zone in the southern Indian Ocean between 5°S-12°S (Fig. 5.4). As is the case for the Atlantic and Pacific, the upper ocean branch is driven by Ekman drift at an average rate of 8 Sv (McCreary et al. 1993; Lee 2004). The return flow of the southern STC is supplied by southern subduction, recirculation, and the ITF.

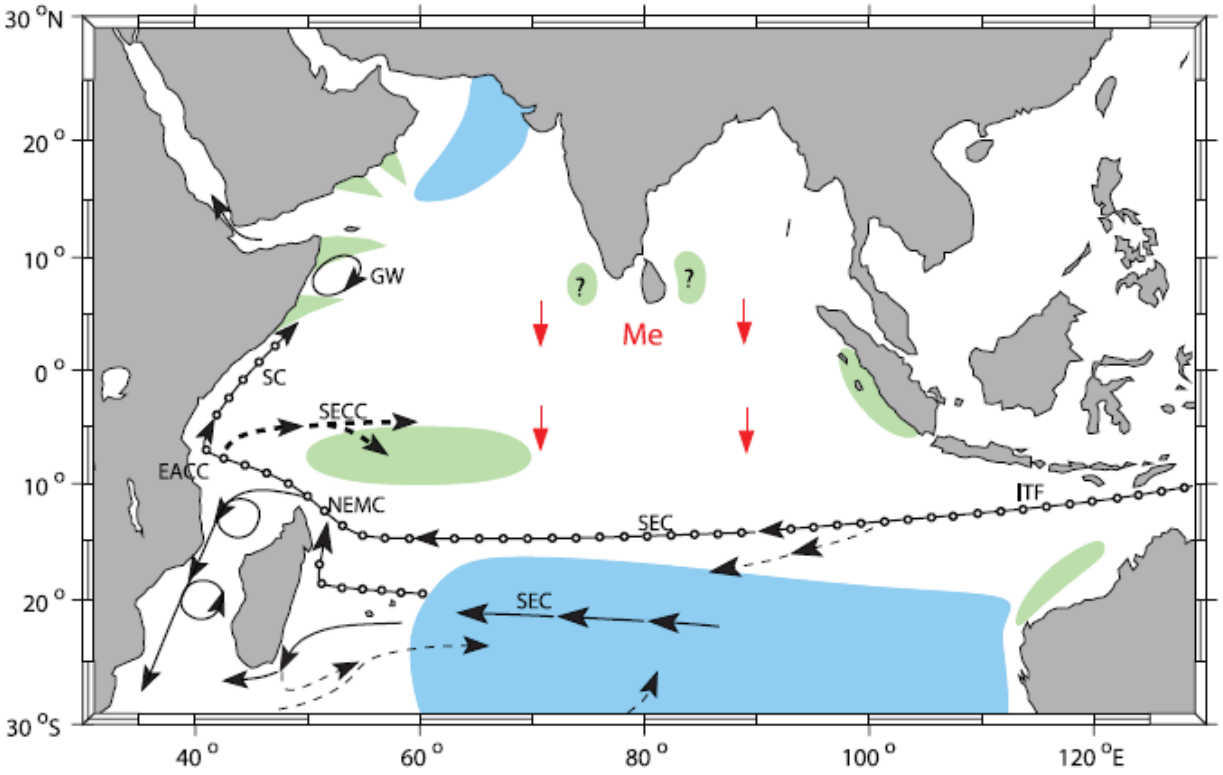

Figure 5.4: Schematic representation of the circulation involved in connecting the regions of upwelling with to the areas of subduction. Figure taken from Schott et al, 2009. The blue shading denotes regions of subduction, the green areas indicate regions of upwelling. The surface Ekman transport is denoted by the red vectors. The black arrows show a number of the characterizing currents of the Indian Ocean. Current acronyms are provided in Chapter 1.

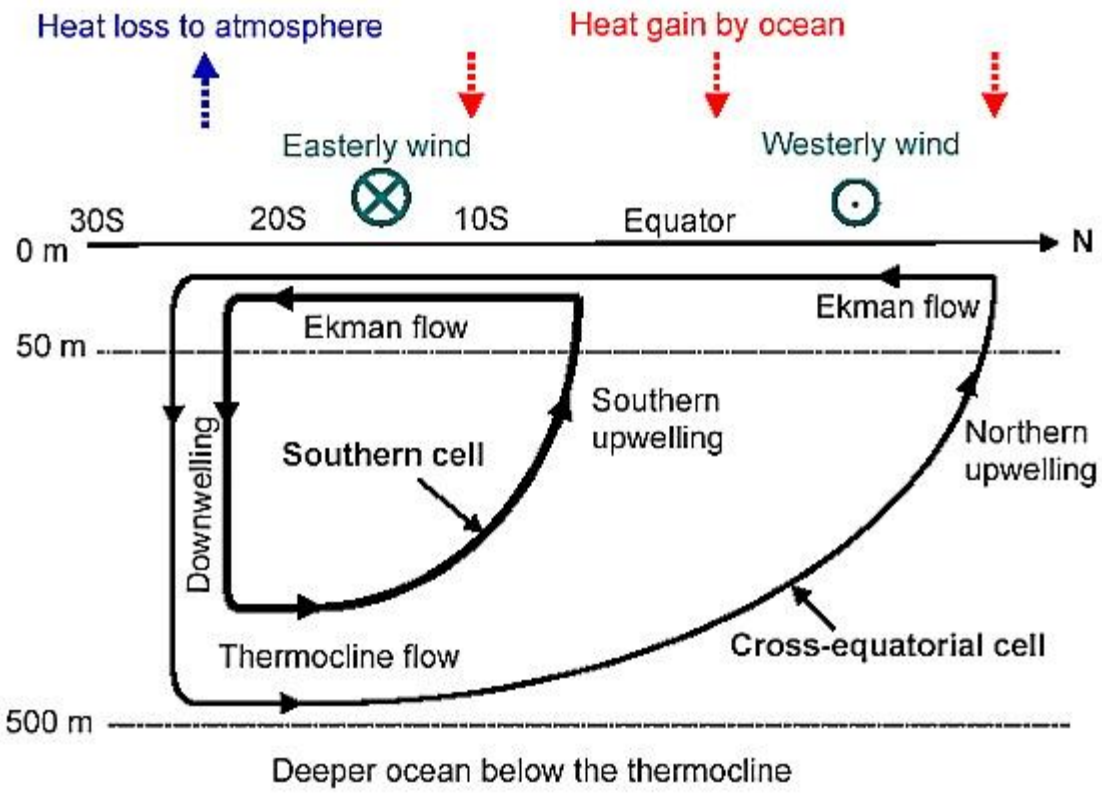

Figure 5.5: Schematic of the shallow meridional overturning circulations of the Indian Ocean, the cross-equatorial cell and the southern cell. The direction of the zonal winds, as well as, the heat flux is also illustrated. Image adapted from Lee 2004.

5.3 Indian Ocean STC variability and winds

Fig. 5.6a (black curve) shows the time series of the estimated strength of the STC, given by the meridional Ekman transport computed from the ERA40 winds at 15^{o}S, the latitude where Ekman pumping velocity (w_e) ~ 0. In the Indian Ocean, this estimate measures the total strength of the SSTC and CEC (Schott et al, 2004). The southward Ekman transport has an increasing trend and enhances by ~2 Sverdrup (Sv) from 1961 – 2000. Consistently, the southward upper-level transports from both SODA-POP and HYCOM increase by 2~3 Sv (Fig. 5.6a).

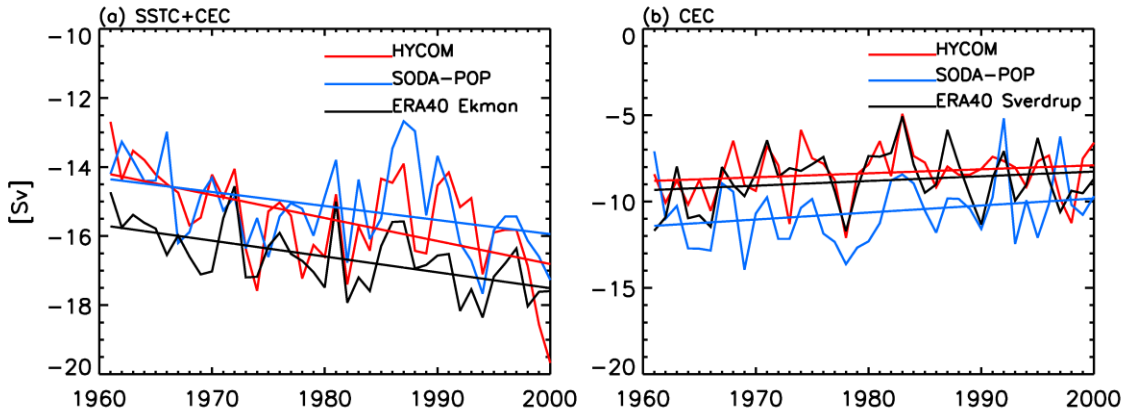

Figure 5.6: (a) Time series of the upper-layer southward transport in HYCOM (red), SODA-POP (blue) and the Ekman transport computed from ERA40 winds (black) at 15°S; the ERA40 winds are used to force both SODA-POP and HYCOM; (b) The upper-layer southward transport at the equator in HYCOM (red), SODA-POP (blue) and the Sverdrup transport computed from ERA40 winds (black). The upper layer transport in HYCOM is the zonal integral of meridional transport from 48°E-115°E at 15°S in the layers equal and above 22.25 kgm^{-3} (below which transport reverses), and from 46°E-100°E at the equator in the layers equal and above 26.18 kgm^{-3}. The upper-layer transport in SODA-POP was computed over the same longitudinal bands, from the surface to the depth where transport reverses.

Interestingly, while the total transport associated with the SSTC and CEC is strengthening, the CEC individually spins down (Fig. 5.6b). The spin down of the CEC is consistent with the estimate of Schoenefeldt and Schott (2006). The difference between the enhanced southward transport at 15°S and the weakened CEC suggests a surface divergence of ~3-4 Sv within the 15°S – 0°S band. This latitudinal band contains the upwelling zone associated with the SSTC and in conjunction, is the region of strongest cooling and enhanced w_e.

Figures 5.7a and 5.7b show scatter plots of the annual mean surface-layer divergence and thermocline-layer convergence between 15°S – 0°S from HYCOM solutions in relation to the annual and zonal mean w_e anomaly averaged over 15°S – 3°S. Of particular interest is the high degree of correlation between the spin up of the SSTC and enhanced w_e on decadal time scales, a correlation on interannual times scales is not apparent. In turn, the enhanced w_e is highly correlated with the thermocline cooling on decadal timescales in both the HYCOM solution and SODA-POP data (Figs 5.7c and 5.7d). The enhanced w_e corresponds to progressive cooling of

the thermocline. These results suggest that a relationship exists between the enhanced w_e, spin-up of the SSTC and thermocline cooling. In addition, the enhanced equatorial westerly winds found in both ERA40 and NCEP reanalysis (not shown) contribute to the anomalous warming in the eastern equatorial basin and cooling in the off equatorial central-western basin, through anomalous equatorial Ekman convergence and off-equatorial Ekman divergence. This contributes to the negative IOD trend shown in Fig. 5.2

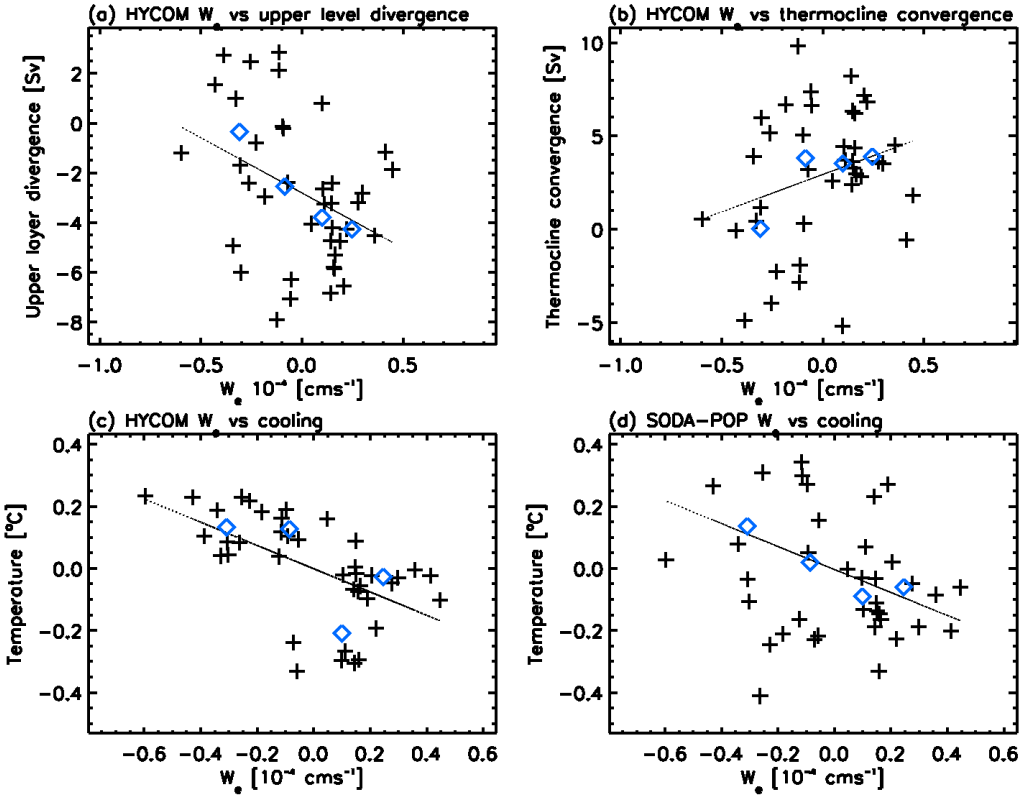

Figure 5.7: (a) A scatter plot of upper-layer divergence between 15°S – 0°S in HYCOM versus w_e anomaly calculated from the ERA40 winds averaged over 15°S – 3°S; (b) Same as in (a) except for thermocline convergence versus w_e anomaly; (c) Same as (a) except for thermocline temperature anomaly averaged in the white box of Fig. 5.1c versus w_e anomaly; (d) Same as in (c) except for SODA-POP thermocline temperature anomaly versus w_e anomaly. Annual mean values denoted by crosses. Decadal mean values denoted by blue diamonds. The thermocline convergence is the difference between the thermocline transport at 15°S and transport of the western boundary current at 0°N (see Schott et al. 2004 for CEC pathways). The thermocline transport at 15°S is the zonal integral of meridional transport from 48°E-115°E for layers 23.25 - 26.18 kgm^{-3}, and along the equator from 35°E-46°E for layers equal and above 26.18 kgm^{-3}.

5.4 STC and climate

Xie et al. (2002) showed that interannual variability of thermocline depth is correlated to changes of sea surface temperature in the upwelling zone of the south tropical Indian Ocean. The decadal change of thermocline depth (and thus the thermocline cooling) and negative Indian Ocean Dipole trend found in our paper can affect the upper ocean heat content, which may feedback onto the atmosphere and subsequently affect the climate. Indeed, reduced precipitation in Africa and enhanced rainfall in the eastern Indian Ocean occurred during our period of interest (Fig 5.8). These rainfall anomalies, together with the anomalous equatorial westerly winds, are the patterns associated with a negative Indian Ocean Dipole (e.g., Saji et al., 1999), indicating the potential importance of Indian Ocean thermocline feedback on climate.

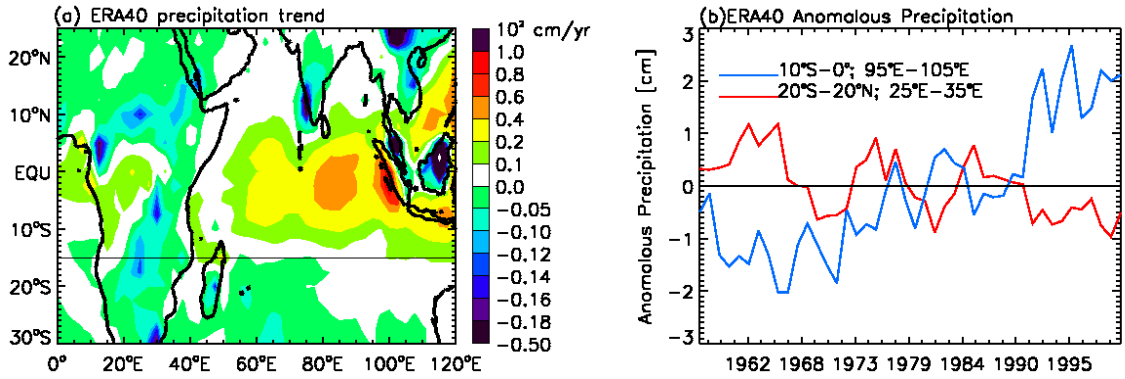

Figure 5.8: (a) Map of the linear precipitation rate trend from ERA40, (b) Time series of the total precipitation rate over eastern Africa (20°S-20°N; 35°E-40°E; red) and near Indonesia (10°S-0°; 95°E-105°E; blue).

5.5 Summary

The vertical structure of temperature change in the Indian Ocean during 1961-2000 indicates that a region of tropical thermocline cooling accompanies the upper level warming. Results from data analysis and ocean general circulation model experiments suggest that the cooling signals exceed the cross-data and cross-model differences. Spatial patterns of the temperature trend above 200m resemble the negative IO dipole structure, with the strongest

cooling occurring in the western-central basin south of the equator. The upper thermocline cooling is mainly caused by enhanced Ekman pumping velocity, which shoals the thermocline. The enhanced upwelling is consistent with the strengthened Southern subtropical cell. Enhanced equatorial westerly winds contribute to the negative dipole pattern.

Chapter 6

Summary and future work

There is a rich spectrum of sea level and thermocline depth variability in the southern Indian Ocean and corresponding unique forcing mechanisms per timescale. Dynamic control of sea level and thermocline depth in the interior of the ocean may arise from local wind stress curl, regionally forced Rossby waves by Ekman pumping to the east, Rossby waves originating from eastern boundary anomalies, nonlinearities in the flow, and energy flux from the Pacific. In this thesis, a suite of diagnostic numerical experiments are used to investigate the cause(s) of intraseasonal-to-multi-decadal timescale variability of southern Indian Ocean sea level and thermocline depth. Two separate models were used in this study: HYCOM a full physics primitive equation ocean general circulation model and a relatively simple linear normal mode model.

Analysis of these numerical model solutions suggests that the physical mechanism(s) responsible for sea level and thermocline depth variations are dependent upon the location within the southern Indian Ocean and timescale of the forcing. While various latitudinal bands are examined as part of this study, the major analysis is performed in the region know as the Thermocline Ridge of the Indian Ocean (TRIO). The TRIO is characterized by a climatologically shallow thermocline in the southwestern Indian Ocean, between 50^{o}E-80^{o}E and bounded latitudinally between 5^{o}S-12^{o}S. The degree to which energy flux from the Pacific Ocean penetrates into the interior of the southern Indian Ocean is also found to be time scale dependent. Below, the primary findings of this thesis are summarized based on timescale (sections 6.1-6.3) and the direction of future work discussed (section 6.4).

6.1 Interannual-to-intraseasonal

On interannual time scales, sea level and thermocline depth variability in the TRIO region is primarily driven by atmospheric forcing acting on the Indian Ocean. Consistent with previous studies, the models results presented here, similarly suggest that sea level and thermocline depth variability in the TRIO region is largely controlled by Rossby waves forced by the Ekman pumping velocities east of the region. Equatorward of 12^{o}S, the fundamental dynamics of the southern Indian Ocean response are linear, and the westward-propagating Rossby waves are generally captured by the first and second baroclinic modes. The Pacific contribution to the amplitude and phase of the southern Indian Ocean waves is weak in the TRIO region, even though its influence is significant in the eastern basin. South of 12^{o}S, linear wave signatures are still identifiable in the nonlinear HYCOM solutions. For example, Rossby waves get shorter and slower with the increase of latitude, as predicted by the linear theory. Large differences, however, exists between the HYCOM and LOM solutions. These differences indicate that nonlinear processes, changes in stratification, realistic topography and the barotropic mode, which are all absent in the LOM, may be important in causing interannual variability of sea level and thermocline south of 20°S.

On the seasonal timescale, variability of thermocline depth (represented here as the depth of 20^{o}C isotherm; D20) and SSH in the TRIO region are driven by different forcing mechanisms based on location within the ridge. Over the northern portion of the TRIO (5^{o}S-10^{o}S; 50^{o}E-75^{o}E), thermocline variability exhibits a semiannual cycle, with deep D20 occurring in February and September and shallow D20 in May and December. Previous studies have suggested that the semiannual cycle of the TRIO is driven by local Ekman pumping (Yokoi et al. 2008) and may be impacted by the arrival of remotely forced Rossby waves (Hermes and Reason, 2008). Here we

demonstrate that the seasonal variability of thermocline depth is primarily forced by winds acting on the Indian Ocean and is associated with the arrival of the westward-propagating Rossby wave and direct Ekman pumping. Forcing by Rossby wave arrival appears greatest from January-July, while local forcing becomes more important during the latter part of the year. The Pacific forcing makes relatively weak contribution in the region, even though it causes large amplitude SSHA and D20A in the eastern basin. The Pacific-forced annual signals interfere constructively (for example, February-March) or destructively (June-October) with the Indian Ocean forced semiannual signals in the north portion of the TRIO region. Further south (60^{o}E-80^{o}E, 8^{o}S-12^{o}S), sea level and thermocline variability is dominated by an annual cycle and is largely forced by local Ekman pumping. The arrival of Rossby waves generated by winds east of the region, however, also contributes to the amplitudes of D20A. The Pacific forcing somewhat reduces the amplitudes of D20A in the region. In addition, the Pacific forced D20As in the eastern Indian Ocean are out of phase with those forced by the local longshore winds. Introducing the Pacific signals essentially removes the D20A generated locally by the longshore winds.

On intraseasonal time scales, the strongest SSHA and D20A occur in the southeast tropical Indian Ocean. HYCOM and LOM experiment results suggest that this variability primarily arises from oceanic instabilities. The relatively weak SSHA/D20A in the TRIO region most likely result from direct forcing by intraseasonal winds.

Variability of the ITF transport can be affected by winds over both the Indian and Pacific Oceans. While the Pacific forcing is more important in causing the interannual variability of ITF transport, the Indian Ocean forcing plays a larger role in determining its seasonal and intraseasonal variability.

6.2 Decadal

On annual to interannual timescales the transmission of Pacific signals into the interior of the Indian Ocean is weak and thermocline variability is dominated by regional winds acting on the southern Indian Ocean (see above). Multi-decadal trends, however, are suggestive of a more prominent contribution from the Pacific at longer time scales (Trenary and Han 2008; Schwarzkopf and Böning 2011).

Our results show that decadal variations of the vertical structure of temperature zonally-averaged across the Indian Ocean can be described by two distinct spatial patterns. One is characterized by similarly signed temperature anomalies in the upper 300 meters within the 5^{o}S-15^{o}S band, with maximum variability in thermocline (EOF1). The second dominant pattern (EOF2) of temperature variability shows temperature variations of one sign occupying the upper 100m of the ocean, capping a region of oppositely signed anomalies. The subsurface temperature anomalies peak south of 10^{o} between the depths of 200-500m. Horizontal structures of decadal SSHA, D20A and temperature variability of the thermocline layer (100m~300m) show complex patterns, and their variations are highly correlated, suggesting the importance of upper-ocean baroclinic adjustment. Periods characterized by uniform upper ocean temperature anomalies (EOF1) tend to be associated with like signed basin wide anomalies in the upper thermocline. The horizontal structure of thermocline depth temperature variations associated EOF2 are characterized by temperature anomalies of one sign in the tropics surrounded by anomalies of the opposite sign.

Wind forcing over the Indian Ocean plays a deterministic role in causing the spatial (vertical and horizontal) patterns of decadal variability of SSH, D20 and thermocline temperature in the south Indian Ocean. The ITF, however, can have significant contributions to the

temperature anomalies especially in the thermocline during some decades. Oceanic instabilities are important in generating decadal variability of SST, SSH and D20 in the subtropical south Indian Ocean from 20°S-30°S.

In the tropical south Indian Ocean (between 5^{o}S-17^{o}S), within the vicinity of the Indonesian throughflow, our model results indicate that thermocline anomalies originating from the Pacific have little impact on the sea level/thermocline depth variations in the western Indian Ocean prior to the 1990's. During this time, variations in the western Indian Ocean thermocline depth are dictated by a baroclinic Sverdrup balance resulting from oceanic adjustment to the Indian Ocean windstress curl forcing. Beginning in the early 90's, D20As from INDOPAC and IND begin to diverge. The rapid shoaling of D20 in the eastern Indian Ocean coincides with the weakening of the equatorial Pacific trade winds, that begins in the early 90's, peaks around 1993, and lasts until 1997. Weakening of the equatorial Pacific trade winds is proceeded by a period of strengthening and the transmission of positive thermocline depth anomalies to the tropical southern Indian Ocean. Before the 1990's, the transmission of decadal thermocline anomalies from the Pacific into the southern Indian was minimal. Consistent with our results, the estimated ITF transport from 14 different ocean data assimilation products all show a robust decadal scale change in the ITF during the 1990s, with little to no change in the ITF before/after 1977 (Lee et al. 2010). As noted by Wainwright et al. (2008), estimates of the ITF transport calculated from the Island Rule (Godfrey, 1989) remained nearly constant following the 1976/77 climate shift, regardless of whether NCEP or ECMWF wind products were used. The results from this study suggest that the transmission efficiency of decadal thermocline anomalies from the Pacific has increased during the 1990s.

In the subtropics between 20°S-30°S, decadal adjustment of the thermocline in the IND experiment more closely follows Sverdrup balance; however, there are significant westward-propagating Rossby wave signals that lead to deviatations from the balance. This is because the oceanic adjustment times are longer at higher latitudes. The two experiments show a high degree of correlation between the eastern boundary anomalies, but the correlation drops significantly in the west, indicating that the thermocline depth variability is strongly modified in the interior of the ocean. Prior to the 1990's, the strong agreement in phase and magnitude of the eastern boundary anomalies suggests that local forcing in the Indian Ocean determines both the amplitude and sign of anomalies found off the western coast of Australia. After the 1990s, however, Pacific forcing is important in causing the SSHA along the west Australian coast.

Differences between the solutions in the western basin reflect the influence of oceanic instabilities associated with nonlinearities of the oceanic system, and may arise from unstable baroclinic Rossby waves. It is also possible that by limiting variability of the ITF, we have in turn modified the stability of the South Indian Counter Current and the South Equatorial Current system (Jia et al. 2011a,b). An experiment forced solely by atmospheric climatology also highlights the contributions of oceanic internal variability to decadal time scale variation in surface temperature, SSH, and thermocline depth.

Spatial patterns of the observed/simulated sea level trends for 1993-2000 and 2000-2006 periods as well as their phase reversal are primarily caused by forcing over the Indian Ocean, with the ITF contributing to the sea level rise during 1993-2000 and fall during 2000-2006 in the eastern tropical Indian Ocean and along the west Australian coast. Consistent with the SSH change, thermocline temperature anomalies in the south tropical Indian Ocean also exhibit decadal phase reversal, with cooling from 1993-2000 and warming from 2000-2006 .

6.3 Multi-decadal trends

Linear trend analysis of the zonal mean temperature field of historical data (Levitus 2009) spanning the last 40 years indicates that the thermal structure of the Indian Ocean is changing. The evolution of zonal mean temperature in the upper thermocline is complex, but can be summarized as regions of maximum surface warming occupying the subtropics of both hemispheres and penetrating to depths of 200 –300 m, depending on the hemisphere. The surface warming is accompanied by subsurface thermocline cooling that is localized in tropical thermocline, with the strongest cooling occurring at 10^{o}S and confined to the upper 200m. Updated data from the WOD, output from SODA-POP reanalysis product, as well as output from the numerical models HYCOM and POP-Hindcast, all captured the broad characterizing features of the zonal mean temperature field during 1961-2000. A time series of the zonal mean temperature within the cooling region, computed separately for each data set confirms the persistence of thermocline cooling, a signal that exceeds cross-model and dataset differences.

Through analysis, it is found that the Cross Equatorial Cell (CEC) of the Indian Ocean is spinning down, this spin-down is driven by the decrease in the cross equatorial Sverdrup transport, and is associated with a decreases in both the upper level southward interior flow and the Somali current. These finding are consistent with previous work by Schoenefeldt et al. (2006), who similarly found a spin-down in the CEC in output from the SODA assimilation product for the years 1950-2001. Model results generated by HYCOM and SODA reanalysis indicate that the upper level southward transport in the subtropical southern Indian Ocean has been increasing in response to increasing Ekman transport. Further, the subsurface northward flow has similarly increased in response to changes in the upper level flow. It was found that a significant correlation exists between the thermocline convergence at 15 ^{o}S and changes in the

zonal mean anomalous Ekman pumping. The correlation indicates that weakened thermocline convergence is related to weakened Ekman pumping and vice versa. Similarly, a significant correlation was found between the surface divergence and Ekman pumping. Changes in Ekman pumping are in turn found to be correlated to changes in the zonal mean anomalous temperature of the region of maximum cooling in both HYCOM and SODA-POP. These results do not prove the existence of a subtropical/tropical exchange altering subsurface temperature; however these results are consistent with the hypothesis that variability of the subtropical cell (STC) can affect the tropical thermocline.

6.4 Future work

Recommendations for future work fall into three broad categories: (i) sensitivity experiments, (ii) the role of nonlinearities, and (iii) air-sea interactions.

6.4.1 Sensitivity experiments

Recommendations in this category will help establish the upper and lower bounds of Pacific influence, via the oceanic bridge, on multi-timescale seal level and thermocline depth variability in the Indian Ocean.

- Perform HYCOM experiments with less topographical smoothing. Current results use a 2^{o}x2^{o} smoothing; as a result the Lombok strait is not clearly defined in the model. Experiments should be performed in which the smoothing is systematically reduced by half to 1 ^{o}, ½ ^{o}, etc., until the topography of the Indonesian Archipelago is more accurately depicted. Analysis similar to what has been performed here can be replicated to determine the robustness of these general conclusions. Stability constraints will require a decrease in model resolution to follow reductions in smoothing.

- Flows within the Indonesian seas are strongly modified by tidal mixing. Once the optimal topographic smoothing has been identified, sensitivity experiments should be performed that include tidal mixing.

- Perform a second experiment using HYCOM, allowing the atmospheric forcing acting on the Pacific to vary and holding the forcing over the Indian Ocean constant. Following pervious nomenclature, this would be labeled the PAC experiment, and variations arising in the Indian Ocean would be largely related to the transmission of signals from the Pacific.

- Perform similar experiments to IND and INDOPAC, using other widely used ocean general circulation models. Do the other models show similar timescale dependent transmission of energy from the Pacific to the Indian Ocean?

6.4.2 Nonlinearities

Inferences made from the current results suggest that nonlinearities of the flow substantially alter sea level and thermocline depth in the southern Indian Ocean. The general recommendations made below are intended to help identify the source of the eddies and to clarify their role in forcing multi-timescale SSHA/D20A.

- Compare the eddy kinetic energy between the IND and INDOPAC experiments. Determine if differences exist between experiments in terms of the location and amplitude of eddies.

- Quantify differences in eddy activity through stability analysis and comparison of growth rates in different regions of the southern Indian Ocean

- Determine whether the remote oceanic influence from the Pacific contributes to changes in the meridional temperature gradient in the southern Indian Ocean, and consequently basin thermal wind balance, and the stability of the southern Indian Ocean currents. If remote oceanic forcing from the Pacific does contribute to differences in the mean state, does remote forcing from the Pacific systematically contribute to seasonal-to-decadal differences in the eddy activity?

- On decadal timescales, the model results presented in this study show that anomalies along the eastern boundary appear to propagate westward as Rossby waves and 'break-up' mid-basin. Through a stability analysis, IND and INDOPAC solutions will be compared to determine whether remote forcing from the Pacific make waves more or less stable.

6.4.3 Air-sea interactions

This study focused exclusively on the forced response of the ocean to atmospheric forcing and the resulting exchange between the Pacific and Indian Oceans. The source of variations in atmospheric forcing acting on the Indian Ocean and the role the ITF in regional/global air-sea interactions are completely neglected. To help address these issues, the following coupled experiments are suggested:

- The source of variations in atmospheric conditions over the Indian Ocean will be diagnosed from a coupled-model experiment, in which the air-sea interactions over the Pacific have been turned off, while the coupling over the Indian Ocean remains active. Comparison of the experiment solutions with those obtained from a fully-coupled run can

be used to infer the remote influence from the Pacific on variations in the Indian Ocean atmospheric conditions and subsequent ocean response.

- Comparisons of models solutions with and without an open Indonesian Passage indicate that the Indonesian Throughflow warms the eastern Indian Ocean, as a result, the warm pool and the centers of deep convection are shifted westward. To isolate the impact of ITF on coupled ocean/atmosphere processes, the air-sea interactions within the eastern Indian Ocean will be turned off in a coupled general circulation model. These solutions will be compared to solutions from a fully coupled model.

Bibliography

Allan, R. J., J. A. Lindesay, and C. J. C. Reason, 1995: Multidecadal variability in the climate system over the Indian Ocean region during the austral summer. *J. Climate*, **8,** 1853–1873.

Alory, G., S. Wijffels, and G. A. Meyers, 2007: Observed temperature trends in the Indian Ocean over 1960-1999 and associated mechanisms. *Geophy. Res. Lett.,* **34**,1232-1253.

Annamalai, H., P. Liu, and S.-P. Xie, 2005: Southwest Indian Ocean SST variability: Its local effect and remote influence on Asian monsoons. *J. Clim*., **18**, 4150–4167.

Ashok, K., W-L. Chan, T. Motoi, and T. Yamagata, 2004: Decadal variability of the Indian Ocean dipole. *Geophys. Res. Lett.*, **31,**L24207, doi:10.1029/2004GL021345.

Atmadipoera, A., R. Molcard, G. Madec, S. Wijffels, J. Sprintall, A. Koch-Larrouy, I. Jaya, and A. Supagat, 2009: Characteristics and variability of the Indonesian Throughflow Water at the Outflow Straits. *Deep Sea Res., Part I*, **56**, doi:10.1016/j.dsr.2009.06.004, 1942-1954.

Baquero-Bernal, A., and M. Latif, 2005: Wind-driven oceanic Rossby waves in the Tropical South Indian Ocean with and without an active ENSO. *J. Phys. Oceanogr*., **35**, 729–746.

Barnett T.P. and Coauthors, 2005: Penetration of human-induced warming into the world's oceans, *Science*, ***309***, 284-287.

Battisti, D.S., 1988: The Dynamics and Thermodynamics of a Warming Event in a Coupled Tropical Atmosphere/Ocean Model. *J. Atmos. Sci.*, **45**, 2889-2919.

Berloff, P., A. Mc C. Hogg, and W. Dewar, 2007: The Turbulent Oscillator: A Mechanism of Low-Frequency Variability of the Wind-Driven Ocean Gyres. *J. Phys. Oceanogr.*, **37**, 2363–2386.

Birol, F., and R. Morrow, 2001: Source of the baroclinic waves in the southeast Indian Ocean. *J. Geophys. Res.*, **106**, 9145–9160, doi:10.1029/2000JC900044.

Bleck, R., 2002: An oceanic general circulation model framed in hybrid isopycnic-Cartesian coordinates. *Ocean Model.*, ***4***, 55-88.

Boccaletti, Giulio, R.C. Pacanowski, S.G.H. Philander, and A.V. Fedorov, 2004: The thermal structure of the upper ocean, *J. Phys. Oceanogr.*, *34*, 888-902.

Boulanger, J-P., S. Cravatte, and C. Menkes, 2003: Reflected and locally wind-forced interannual equatorial Kelvin waves in the western Pacific Ocean. *J. Geophys. Res.*, **108.**3311, doi:10.1029/2002JC001760.

Brandt P., M. Dengler, A. Rubino, D. Quadfasel, and F. Schott, 2003: Intraseasonal variability in the southeastern Arabian Sea and its relation to the seasonal circulation. *Deep Sea Res., Part II*, **50**, 2129-2141.

Bray, N., S. Hautala, J. Chong and J. Pariwono, 1996: Large-scale sea level, thermocline, and wind variations in the Indonesian throughflow region. *J. Geophys. Res.*, **101**, 12,239-12,254.

Brodeau, L., B. Barnier, A. Treguier, T. Penduff, and S. Gulev, 2009: An ERA40-based atmospheric forcing for global ocean circulation models. *Ocean Model.*, **31,** 88-104.

Capotondi, A., M. A. Alexander, C. Deser, and M. J. McPhaden, 2005: Anatomy and decadal evolution of the Pacific Subtropical Cells (STC). *J. Clim.*, **18,** 3739-3758.

Carson, Mark, D. E. Harrison, 2008: Is the Upper Ocean Warming? Comparisons of 50-Year Trends from Different Analyses*. *J. Climate*, **21**, 2259–2268.

Carton, J.A., and B.S. Giese, 2008: A reanalysis of ocean climate using Simple Ocean Data Assimilation (SODA). *Mon. Wea. Rev.*, **136**, 2999-3017.

Chambers, D. P., B. D. Tapley, and R. H. Stewart, 1999: Anomalous warming in the Indian Ocean coincident with El Niño. *J. Geophys. Res*., **104**, 3035–3047.

Clarke, A. J., 1983: The reflection of equatorial waves from ocean boundaries. *J. Phys. Oceanogr*., **13,** 1193–1207.

Clarke, A. J., 1991: On the reflection and transmission of low-frequency energy at the irregular western Pacific boundary. *J. Geophys. Res.*, **96** (Suppl), 3289-3305.

Clarke, A. J., and X. Liu, 1993: Observations and dynamics of semiannual and annual sea levels near the eastern equatorial Indian Ocean boundary. *J. Phys. Oceanogr.*, **23**, 386-399.

Clarke, A. J., and X. Liu, 1994: Interannual sea level in the northern and eastern Indian Ocean. *J. Phys. Oceanogr*., **24**, 1224-1235.

Coatanoan, C., N. Metzl, M. Fieux, and B. Coste, 1999: Seasonal water mass distribution in the Indonesian throughflow entering the Indian Ocean. *J. Geophys. Res.*, **104**, 20,801–20,826, doi:10.1029/1999JC900129.

Cobb, K.M., D.E. Hunter, and C.D. Charles. 2001. A central tropical Pacific coral demonstrates Pacific, Indian, and Atlantic decadal climate connections. *Geophys. Res. Lett*, **28**, 2209-2212.

Cole, J. E., R. B. Dunbar, T. R. McClanahan, and N. A. Muthiga, 2000: Tropical Pacific forcing of decadal SST variability in the western Indian Ocean over the past two centuries. *Science*, **287,** 617–619.

Cravette, S., J. Boulanger and J. Picaut, 2004: Reflection of intraseasonal equatorial Rossby waves at the western boundary of the Pacific Ocean. *Geophys. Res. Lett.*, **31**, L10301, doi: 10.1029/2004GL019679.

de Ruijter, W. P., van Aken, H. M, Beier, E. J., Lutjeharms, J. R. E., Matano, R. P., and Schouten, M. W., 2004: Eddies and dipoles around South Madagascar: formation, pathways and large-scale impact. *Deep Sea Res., I,* 51, 383-400.

Dijkstra, H. and Ghil, M., 2005: Low-frequency variability of the large-scale ocean circulation: A dynamical systems approach. *Reviews of Geophysics*, **43**, doi: 10.1029/2002RG000122.

Doney, S., S. Yeager, G. Danabasoglu, W. Large, and J.C. McWilliams, 2007: Mechanisms governing interannual variability of upper-ocean temperature in a global ocean hindcast simulation, *J. Phys.Oceanogr., 37,*1918-1938.

Donguy, J. R., and G. Meyers, 1995: Observations of geostrophic transport variability in the western tropical Indian Ocean. *Deep Sea Res., Part I,* **42**, 1007–1028.

Drushka, K., J. Sprintall, S. T. Gille, and I. Brodjonegoro, 2010: Vertical Structure of Kelvin Waves in the Indonesian Throughflow Exit Passages. *J. Phys. Oceanogr.*, **40**, 1965–1987, doi:10.1175/2010JPO4380.1 .

Ducet N., P.Y. Le Traon and G. Reverdin, 2000: Global high resolution mapping of ocean circulation from the combination of T/P and ERS-1/2. *J. Geophys. Res.*, **105**,19,477-19,498.

Duchon, C. E., 1979: Lanczos filtering in one and two dimensions. *J. Applied Meteorology*, **18**, 1016-1022.

Dunne, R. P., S.M. Barbosa, and P.L. Woodworth, 2012: Contemporary sea level in the Chagos Archipelago, central Indian Ocean. *Global and Planetary Change*, 82-83. 25-27. 10.1016/j.gloplacha.2011.11.009

Du Penhoat, Y., and M. Cane, 1991: Effect of low-latitude western boundary gaps on the reflection of equatorial motions. *J. Geophys. Res.*, **96,** 3307–3322.

England, M. H., and F. Huang, 2005: On the interannual variability of the Indonesian Throughflow and its linkage with ENSO. *J. Clim.*, **18**, 1435–1444.

Feng, M., and S. Wijffels, 2002: Intraseasonal variability in the South Equatorial Current of the East Indian Ocean. *J. Phys. Oceanogr*., **32**, 265–277.

Feng M., G. Meyers, 2003: Interannual variability in the tropical Indian Ocean: A two-year time scale of Indian Ocean Dipole. *Deep-Sea Research*, **50**, 2263-2284.

Feng, M., M. J. McPhaden, and T. Lee, 2010: Decadal variability of the Pacific subtropical cells and their influence on the southeast Indian Ocean, *Geophys. Res. Lett.*, **37**, L09606, doi:10.1029/2010GL042796.

Ffield, A., and A. L. Gordon, 1992: Vertical mixing in the Indonesian thermocline. *J. Phys. Oceanogr.*, **22**, 184–195.

Fieux, M., R. Molcard, and A. G. Ilahude, 1996: Geostrophic transport of the Pacific-Indian Oceans Throughflow. *J. Geophys. Res*., **101**, 12,421–12,432.

Fieux, M., R. Molcard, R. Morrow, A. Kartavtseff, A.G. Ilahude, 2005: Variability of the throughflow at its exit in the Indian Ocean. *Geophys. Res. Lett.,* **32**, L14616.

Foltz G., J. Vialard, P. Kumar and M.J. McPhaden, 2010: Seasonal mixed layer heat balance of the Southwestern Tropical Indian Ocean, *J. Clim.,* **23**,doi:10.1175/2009JCLI3268.1.

Fu, L.L, and R. D. Smith, 1996: Global ocean circulation from satellite altimetry and high-resolution computer simulation. *Bull. Amer. Meteor. Soc*., **77**, 2625–2636.

Fu, L.L. , 2001: Ocean circulation and variability from satellite altimetry. *Ocean Circulation and Climate: Observing and Modelling the Global Ocean*, G. Siedler, J. Church, and J. Gould, Eds., Elsevier ,141 – 172.

Goddard, L. and N. E. Graham, 1999: The importance of the Indian Ocean for simulating precipitation anomalies over eastern and southern Africa. *J. Geophys. Res.*, **104**, 19099-19116.

Gordon, A.L., and R.A. Fine, 1996: Pathways of water between the Pacific and Indian Oceans in the Indonesian Seas. *Nature*, **379**, 146-149.

Gordon, A.L., R.D. Susanto, and A.L. Ffield, 1999: Throughflow within Makassar Strait. *Geophys. Res. Lett.,* **26**, 3325-3328.

Hamlington, B. D., R.R. Leben, R.S. Nerem, W. Han, and K.-Y. Kim, 2011: Reconstructing sea level using cyclostationary empirical orthogonal functions, *J. Geophys. Res.*, **116**, C12015, doi:10.1029/2011JC007529.

Han, W., P.J. Webster, R. Lukas, P. Hacker, and A. Hu, 2004: Impact of atmospheric intraseasonl variability in the Indian Ocean: low-frequency rectification in equatorial surface current and transport. *J. Phys. Oceanogr.*, **34**, 1350-1372.

Han W., 2005: Origins and Dynamics of the 90-Day and 30–60-Day Variations in the Equatorial Indian Ocean. *J. Phys. Oceanogr.*, **35**, 708–728, doi: 10.1175/JPO2725.1.

Han, W., G. A. Meehl, and A. Hu, 2006: Interpretation of tropical thermocline cooling in the Indian and Pacific oceans during recent decades, *Geophys. Res. Lett.*, **33**, L23615, doi:10.1029/2006GL027982.

Han, W., D. Yuan, W.T. Liu, and D.J. Halkides, 2007: Intraseasonal variability of Indian Ocean sea surface temperatre during boreal winter: MJO versus submonthly forcing and processes. *J. Geophys. Res.*, **112**, C04001, doi:10.1029/2006JC003791.

Han W., P.J. Webster, J. Lin, W.T. Liu, R. Fu, D. Yuan and A. Hu, 2008: Dynamics of intraseasonal sea level and thermocline variability in the equatorial Atlantic during 2002-2003. *J. Phys. Oceanogr.*, **38**, 945-967.

Han, W., G.A. Meehl, B. Rajagopalan, J. Fasullo, A. Hu, J. Lin, W. Large, J. Wang, X. Quan, L. Trenary, A. Wallcraft, T. Shinoda, and S. Yeager, 2010: Patterns of Indian Ocean sea level change in a warming climate. *Nature Geoscience*, DOI:10.1038/NGEO901.

Harrison, D.E., and G.A. Vecchi, 2001: January 1999 Indian Ocean cooling event. *Geophys. Res. Lett.*, **28**, 3717-3720.

Hermes, J. C., and C. J. C. Reason, 2008: Annual cycle of the South Indian Ocean (Seychelles-Chagos) thermocline ridge in a regional ocean model. *J. Geophys. Res.*, **113**, C04035, doi:10.1029/2007JC004363.

Hermes, J. C., and C. J. C. Reason, 2009: The sensitivity of the Seychelles – Chagos thermocline ridge to large-scale wind anomalies. *ICES J. Mar. Sci.*, **66**, 1455 – 1466.

Hirst, A. C., and J. S. Godfrey, 1993: The role of the Indonesian Throughflow in a global ocean GCM. *J. Phys. Oceanogr.*, **23**, 1057–1086.

Huang, B., and J. L. Kinter III, 2002: Interannual variability in the tropical Indian Ocean. *J. Geophys. Res.*, **107**, 3199, doi:10.1029/2001JC001278.

Huang, B., and J.L. Shukla, 2007a: Mechanisms for the Interannual Variability in the Tropical Indian Ocean. Part I: The Role of Remote Forcing from the Tropical Pacific. *J. Clim.*, **20**, 2917-2936.

Huang, B., J.L. Shukla, 2007b: Mechanisms for the Interannual Variability in the Tropical Indian Ocean. Part II: Regional Processes. *J. Clim.*, **20**, 2937–2960.

Huang, R.X., and J. Pedlosky, 2000: Climate variability of the equatorial thermocline inferred from a two-moving-layer model of the ventilated thermocline, *J. Phys. Oceanogr*., *30*, 2610-2626.

Ilahude, A.G., and A.L. Gordon, 1996: Thermocline Stratification Within the Indonesian Seas. *J. Geophys. Res.*, **101**, 12401-12409.

Jerlov, N. G., 1976: *Marine Optics*. Elsevier, 231 pp.

IPCC, 2007: Climate Change 2007 - The Physical Science Basis, Contribution of Working Group I to the Forth Assessment Report of the IPCC. Cambridge University Press, ISBN 978052188009-1.

Jia, F., L. Wu, and B. Qiu, 2011a: Seasonal Modulation of Eddy Kinetic Energy and Its Formation Mechanism in the Southeast Indian Ocean. *J. Phys. Oceanogr.*, **41**, 657–665. doi: 10.1175/2010JPO4436.1

Jia, F., L. Wu, J. Lan, and B. Qiu ,2011b: Interannual modulation of eddy kinetic energy in the southeast Indian Ocean by Southern Annular Mode, *J. Geophys. Res.*, **116**, C02029, doi:10.1029/2010JC006699.

Jury, M. R., and B. Huang, 2004: The Rossby wave as a key mechanism of Indian Ocean climate variability. *Deep Sea Res., Part I,* **51**, 2123–2136.

Jochum, M., and R. Murtugudde, 2005: Internal variability of Indian Ocean SST. *J. Clim.*, **18**, 3726– 3738.

Kalnay, E., and Coauthors, 1996: The NCEP/NCAR 40-year reanalysis project. *Bull. Amer. Meteor. Soc.*, 77, 437-470.

Kamenkovich, Igor V., and E.S. Sarachik, 2004: Mechanisms controlling the sensitivity of the Atlantic Thermohaline Circulation to the parameterization of eddy transports in ocean GCMs, *J. Phys. Oceanogr., 34,* 1628-1647.

Kindle, J. C., and J. D. Thompson, 1989: The 26- and 50-day oscillations in the western Indian Ocean: Model results. *J.Geophys. Res.*, **94**, 4721–4736.

Kleeman, R., J.P. McCreary, and B. Klinger (1999), A mechanism for generating ENSO decadal variability, *Geophys. Res. Lett., 26,* 1743-1746.

Kunze, E., E. Firing, J. M. Hummon, T. K. Chereskin, A. M. Thurnherr, 2006: Global Abyssal Mixing Inferred from Lowered ADCP Shear and CTD Strain Profiles. *J. Phys. Oceanogr.*, **36**, 1553–1576, doi: 10.1175/JPO2926.1.

Large, W. G., J. C. McWilliams, and S. C. Doney, 1994: Oceanic vertical mixing: A review and a model with a nonlocal boundary layer parameterization. *Rev. Geophys.*, **32**, 363–403, doi:10.1029/94RG01872.

Lee, T., I. Fukumori, D. Menemenlis, Z. Xing, and L. L. Fu, 2002: Effects of the Indonesian Throughflow on the Pacific and Indian Oceans. *J. Phys. Oceanogr.*, **32**, 1404–1429.

Lee, T., and M. J. McPhaden, 2008: Decadal phase change in large-scale sea level and winds in the Indo-Pacific region at the end of the 20th century, *Geophys. Res. Lett*., **35**, L01605, doi:10.1029/2007GL032419.

Lee, T.,2004: Decadal weakening of the shallow overturning circulation in the South Indian Ocean, *Geophy. Res. Lett., 31,* L18305, doi:10.1029/2004GL020884.

Lee, T. and coauthors, 2010: Consistency and fidelity of Indonesian-throughflow total volume transport estimated by 14 ocean data assimilation products. *Dyn. of Atmos. and Oceans,* **50**, 201–223.

Levitus, S., J. I. Antonov, T. P. Boyer, R. A. Locarnini, H. E. Garcia, and A. V. Mishonov,2009: Global ocean heat content 1955–2008 in light of recently revealed instrumentation problems, *Geophys. Res. Lett*., **36**, L07608, doi:10.1029/2008GL037155.1.

Levitus, S., J. Antonov, and T. Boyer, 2005: Warming of the world ocean, 1955-2003, *Geophys. Res. Lett., 32*, L02604, doi:10.1029/2004GL021592.

Levitus, S., R. Burgett, and T. P. Boyer, 1994: Salinity. Vol. 3. *World Ocean Atlas 1994*, vol. 3, Salinity, NOAA Atlas NESDIS 3, 111 pp.

Levitus, S., and T. P. Boyer, 1994: Temperature. Vol. 4, *World Ocean Atlas 1994*, NOAA Atlas NESDIS 4, 117 pp.

Liu, Z., 1994: A simple model of the mass exchange between the subtropical and tropical ocean, *J. Phys. Oceanogr., 24,* 1153-1165.

Masumoto, Y., and T. Yamagata, 1996: Seasonal variations of the Indonesian Throughflow in a general circulation model. *J. Geophys. Res.*, **101**, 12,287–12,293.

Masumoto, Y. and G. Meyers, 1998: Forced Rossby waves in the southern tropical Indian Ocean. *J. Geophys. Res.*, **103**, 27589-27602.

McCreary, J.P., and P.K. Kundu, 1987: On the dynamics of the throughflow from the Pacific into the Indian Ocean. *J. Phys. Oceanogr.*, **16**, 2191-2198.

McCreary, J.P., P.K. Kundu, and R.L. Molinari, 1993: A numerical investigation of dynamics, thermodynamics and mixed-layer processes in the Indian Ocean. *Prog. Oceanogr.*, **31**, 181-244.

McCreary, J.P., and P. Lu, 1994: Interaction between the subtropical and equatorial ocean circulations: the subtropical cell, *J. Phys.Oceanogr., 24,* 466-497.

McCreary, J.P., W. Han, D. Shankar, and S. R. Shetye, 1996: Dynamics of the East India Coastal Current 2. Numerical solutions. *J. Geophys. Res.,* **101,** 13 993–14 010.

McCreary, J.P., T. Miyama, R. Furue, T. Jensen, H.-W. Kang, B. Bang, and T. Qu, 2007: Interactions between the Indonesian Throughflow and circulations in the Indian and Pacific Oceans. *Progr. Oceanogr.*, **75**, 70–114.

McPhaden, M.J., and D. Zhang, 2002: Slowdown of the meridional overturning circulation in the upper Pacific Ocean, *Nature, 415,* 603-608.

Meyers, G., 1996: Variation of Indonesian throughflow and ENSO. *J. Geophys. Res.*, **101**, 12,255–12,264.

Murtugudde, R., and A. J. Busalacchi,1999: Interannual variability of the dynamics and thermodynamics of the tropical Indian Ocean. *J. Clim.*, **12**, 2300–2326.

Murtugudde, R. *et al.,* 1999: Ocean color variability of the tropical Indo-Pacific basin observed by SeaWiFS during 1997- 1998, *J. Geophys. Res., 104,* 18351-18366.

Murtugudde, R., J. P. McCreary, and A. J. Busalacchi, 2000: Oceanic processes associated with anomalous events in the Indian Ocean with relevance to 1997–1998. *J. Geophys. Res.,* **105,** 3295–3306.

Ogata, T. and Y. Masumoto, 2010: Interactions between mesoscale eddy variability and Indian Ocean dipole events in the Southeastern tropical Indian Ocean—case studies for 1994 and 1997/1998. *Ocean Dynam.,* **60,**717–730, DOI 10.1007/s10236-010-0304-4.

Ogata, T. and Y. Masumoto, 2011: Interannual modulation and its dynamics of the mesoscale eddy variability in the southeastern tropical Indian Ocean. *J. Geophys., Res*., **116**, C05005, doi:10.1029/2010JC006490.

Périgaud, C., and P. Delecluse, 1992: Annual Sea Level Variations in the Southern Tropical Indian Ocean From Geosat and Shallow-Water Simulations. *J. Geophys. Res.*, **97**, 20,169–20,178, doi:10.1029/92JC01961.

Palastanga, V., P. J. van Leeuwen, M. W. Schouten, and W. P. M. de Ruijter (2007), Flow structure and variability in the subtropical Indian Ocean: Instability of the South Indian Ocean Countercurrent, *J. Geophys. Res.*, **112**, C01001, doi:10.1029/2005JC003395.

Palmer, M. D., S. A. Good, K. Haines, N. A. Rayner, and P. A. Stott ,2009: A new perspective on warming of the global oceans, Geophys. Res. Lett., 36, L20709, doi:10.1029/2009GL039491

Pierce, D. W., T.P. Barnett, K.M. AchutaRao, P.J. Gleckler, J.M. Gregory, and W.M Washington, 2006: Anthropogenic Warming of the Oceans: Observations and Model Results. *J. Climate*, **19**, 1873–1900.

Périgaud, Claire, Pascale Delecluse, 1993: Interannual Sea Level Variations in the Tropical Indian Ocean from Geosat and Shallow Water Simulations. *J. Phys. Oceanogr.*, **23**, 1916–1934.

Potemra, J.T., R. Lukas, and G. Mitchum, 1997: Large-scale Estimation of Transport from the Pacific to the Indian Ocean. *J. Geophys. Res.*, **102**, 27,795–27,812.

Potemra, J. T., 2001: Contribution of equatorial Pacific winds to southern tropical Indian Ocean Rossby waves. *J. Geophys. Res.*, **106**, 2407-2422.

Qu, T.,J. Gan, A. Ishida, Y. Kashino, and T. Tozuka, 2008: Semiannual variation in the western tropical Pacific Ocean. *Geophys. Res. Lett*., **35**, L16602, doi:10.1029/2008GL035058.

Reason, C. J. C., R. J. Allan, and J. A. Lindesay, 1996: Dynamical response of the oceanic circulation and temperature to interdecadal variability in the surface winds over the Indian Ocean. *J. Climate*, **9,** 97–114.

Rao, S.A., S.K. Behera, Y. Masumoto, and T. Yamagata, 2002: Interannual subsurface variability in the tropical Indian Ocean with a special emphasis on the Indian Ocean Dipole. *Deep Sea Res., Part II*, **49**, 1549-1572.

Rao, S.A., and S.K. Behera, 2005: Subsurface influence on SST in the tropical Indian Ocean: Structure and interannual variability. *Dyn. Atmos. Oceans*, **39**, 103-139.

Saji, N. H., B. N. Goswami, P. N. Vinayachandran, and T. Yamagata, 1999: A dipole in the tropical Indian Ocean. *Nature*, **401**, 360–363.

Saji, N. H., S.-P. Xie, and C.-Y. Tam, 2006: Satellite observations ofintense intraseasonal cooling events in the tropical south Indian Ocean. *Geophys. Res. Lett.*, **33**, L14704, doi:10.1029/2006GL026525.

Santoso, A., A. R. Sen Gupta, and M. H. England**,** 2010: Genesis of Indian Ocean mixed layer temperature anomalies: a heat budget analysis. *J. Clim.*, **23**, 5375-5403.

Schiller A. , S. E. Wijffels, J. Sprintall, R. Molcard and P. R. Oke, 2010: Pathways of intraseasonal variability in the Indonesian Throughflow region. *Dyn. Atmos. Oceans*, **50**, 174–200. doi:10.1016/j.dynatmoce.2010.02.003.

Schott, F. A., S.-P. Xie, and J. P. McCreary Jr., 2009: Indian Ocean circulation and climate variability. *Rev. Geophys.*, **47**, RG1002, doi:10.1029/2007RG000245.

Schott, F., J.P. McCreary, and G.C. Johnson, 2004: Shallow overturning circulations of the tropical-subtropical oceans, *AGU Geophys. Monogr. Series, 147*, Eds. C. Wang, S.-P. Xie, J. A. Carton, 261-304.

Schneider, N., 1998: The Indonesian throughflow and the global climate system. *J. Climate*, **11**, 676–689.

Schoenefeldt, R., and F. Schott, 2006: Decadal variability of the Indian Ocean cross-equatorial exchange in SODA, *Geophys. Res.* Lett., 33.

Schwarzkopf, F. U., and C. W. Böning, 2011: Contribution of Pacific wind stress to multi-decadal variations in upper-ocean heat content and sea level in the tropical south Indian Ocean, *Geophys. Res. Lett.*, **38,** L12602, doi:10.1029/2011GL047651.

Schmeits, M.J., Dijkstra, H.A., 2001. Bimodal behavior of the Kuroshio and the GulfStream. *J. Phys. Oceanogr,* **31**, 3435–3456.

Shi, G., J. Ribbe, W. Cai, and T. Cowan (2007), Multidecadal variability in the transmission of ENSO signals to the Indian Ocean, *Geophys. Res. Lett.*, **34**, L09706, doi:10.1029/2007GL029528

Shinoda, T., H.H. Hendon, M. A. Alexander, 2004: Surface and subsurface dipole variability in the Indian Ocean and its relation with ENSO. *Deep Sea Res., Part I*, **51**, 619 – 635.

Spall, M. A., and J. Pedlosky, 2005: Reflection and Transmission of Equatorial Rossby Waves. *J. Phys. Oceanogr.*, **35**, 363-373.

Sprintall, J., J. Chong, F. Syamsudin, W. Morawitz, S. Hautala, N. Bray, and S. Wijffels, 1999: Dynamics of the South Java Current in the Indo-Australian Basin. *Geophys. Res. Lett.*, **26**,

2493–2496.

Sprintall, J., A. L. Gordon, R. Murtugudde, and R. D. Susanto, 2000: A semiannual Indian Ocean forced Kelvin wave observed in the Indonesian seas in May 1999. *J. Geophys. Res.*, **105,** 17 217–17 230.

Sprintall, J., J. T. Potemra, S. L. Hautala, N. A. Bray, and W. W. Pandoe, 2003: Temperature and salinity variability in the exit passages of the Indonesian Throughflow. *Deep Sea Res., Part II*, **50**, 2183–2204.

Sprintall, J., S. Wijffels, A. L. Gordon, A. Ffield, R. Molcard, R. D. Susanto, I. Soesilo, J. Sopaheluwakan, Y. Surachman, and H. M. van Aken , 2004: INSTANT: A new international array to measure the Indonesian Throughflow. *Eos Trans. AGU*, **85**, doi:10.1029/2004EO390002.

Sprintall, J., S. E. Wijffels, R. Molcard, and I. Jaya, 2009: Direct estimates of the Indonesian Throughflow entering the Indian Ocean: 2004–2006. *J. Geophys. Res.*, **114**, C07001, doi:10.1029/2008JC005257.

Timmermann, A., S. McGregor,and F.F. Jin, 2010: Wind Effects on Past and Future Regional Sea Level Trends in the Southern Indo-Pacific*. *J. Climate*, **23**, 4429–4437.

Tsai, P. T. H., J. J. O'Brien, and M. E. Luther, 1992: The 26-day oscillation observed in the satellite sea surface temperature measurements in the equatorial western Indian Ocean. *J. Geophys. Re*s., **97**, 9605– 9618.

Tozuka, T., J.J. Luo, S. Masson, T. Yamagata, 2007: Decadal Modulations of the Indian Ocean Dipole in the SINTEX-F1 Coupled GCM. *J. Climate*, **20**, 2881–2894.

Tozuka, T., T. Yokoi, and T. Yamagata, 2010: A modeling study of interannual variations of the Seychelles Dome. *J. Geophys. Res.*, **115**, C04005, doi:10.1029/2009JC005547.

Trenary, L. L., and W. Han, 2008: Causes of decadal subsurface cooling in the tropical Indian Ocean during 1961–2000, *Geophys. Res. Lett.*, **35**, L17602, doi:10.1029/2008GL034687.

Trenary, L. L., and W. Han, 2012: Intraseasonal-to-Interannual Variability of South Indian Ocean Sea Level and Thermocline: Remote versus Local Forcing. *J. Phys. Oceanogr.*, **42**, 602–627.

Vecchi, G.A., and D.E. Harrison, 2004: Interannual Indian rainfall variability and Indian Ocean sea surface temperature anomalies. *Earth Climate: The Ocean-Atmosphere Interaction, Geophys. Monogr. Ser.*, 147, American Geophysical Union,., 247-260.

Verschell, M. A., J. C. Kindle, and J. J. O'Brien, 1995: Effects of Indo–Pacific throughflow on the upper tropical Pacific and Indian Oceans. *J. Geophys. Res.*, **100,** 18409–18420.

Vialard, J., and Coauthors, 2009: Cirene: Air-sea interactions in the Seychelles-Chagos thermocline ridge region. *Bull. Am. Meteorol. Soc.*, **90**, 45–61.

Wainwright, L.,G. Meyers, S. Wijffels, and L. Pigot, 2008: Change in the Indonesian Throughflow with the climatic shift of 1976/77. *Geophys. Res. Lett.*, **35**, L11608, doi:10.1029/2008GL033974.

Wang, B., R. Wu, R. Lukas, 2000: Annual adjustment of the thermocline in the Tropical Pacific Ocean. *J. Clim.*, **13**, 596-615.

Wang, L., C. J. Koblinsky, and S. Howden, 2001: Annual Rossby wave in the Southern Indian Ocean: Why does it "appear" to break down in the middle ocean?. *J. Phys. Oceanogr*., **31**, 54–74.

Webster, P. J., A. M. Moore, J. P. Loschnigg, and R. R. Leben, 1999: Coupled oceanic-atmospheric dynamics in the Indian Ocean during 1997–98. *Nature*, **401**, 356–360.

White W.B, 2000: Evidence for Coupled Rossby Waves in the Annual Cycle of the Indo–Pacific Ocean. *J. Phys. Oceanogr.*, **31,** 2944-2957.

Wijffels, S, J. Sprintall, M. Fieux and N. Bray, 2002: The Throughflow in the Southeast Indian Ocean. Part 1: Water mass variability. *Deep-Sea Research, Part II*,**49**, 1341-1362.

Wijffels, S. E., and G. Meyers, 2004. An intersection of oceanic waveguides – variability in the Indonesian Throughflow region. *J. Phys. Oceanogr.*, **34**, 1232-1253.

Willis, J. K., D. Roemmich, and B. Cornuelle, 2004: Interannual variability in upper ocean heat content, temperature, and thermosteric expansion on global scales, *J. Geophys. Res*., **109**, C12036, doi:10.1029/2003JC002260

Woodberry, K. E., M. E. Luther, and J. J. O'Brien, 1989: The Wind-Driven Seasonal Circulation in the Southern Tropical Indian Ocean. *J. Geophys. Res.*, **94**, 17,985–18,002, doi:10.1029/JC094iC12p17985.

Wyrtki, K. ,1987: Indonesian Throughflow and the associated pressure gradient. *J. Geophys. Res.*, **92**, 12,941–12,946.

Xie, P. and P. A. Arkin, 1996: Analysis of global monthly precipitation using gauge observations, satellite estimates, and numerical model predictions. *J. Clim.*, **9**, 840-858.

Xie, S.-P., H. Annamalai, F. A. Schott, and J. P. McCreary, 2002: Structure and Mechanisms of South Indian Ocean Climate Variability. *J. Climate*, **15**, 864–878.

Yamanaka, G., 2008: Discrepancies between observed and ocean general circulation model-simulated anomalies in recent SSTs of the tropical Indian Ocean by apparent trends in atmospheric reanalysis data. *Geophys. Res. Lett.*, **35**, L18603, doi:10.1029/2008GL034737.

Yang, J., L. Yu, C. J. Koblinsky, and D. Adamec, 1998: Dynamics of the seasonal variations in the Indian Ocean from TOPEX/POSEIDON sea surface height and an ocean model. *Geophys. Res. Lett.*, **25**, 1915–1918, doi:10.1029/98GL01401.

Yokoi, T., T. Tozuka, and T. Yamagata, 2008: Seasonal Variation of the Seychelles Dome. *J. Climate*, **21**, 3740–3754. doi: 10.1175/2008JCLI1957.1.

Yu, W., B. Xiang, L. Liu, and N. Liu, 2005: Understanding the origins of interannual thermocline variations in the tropical Indian Ocean. *Geophys. Res. Lett.*, **32**, L24706, doi:10.1029/2005GL024327.

Yu, Z., and J. Potemra, 2006: Generation mechanism for the intraseasonal variability in the Indo-Australian basin. *J. Geophys. Res.*,**111**, C01013, doi:10.1029/2005JC003023.

Zang, X., L-L. Fu, and C. Wunsch, 2002: Observed reflectivity of the western boundary of the equatorial Pacific Ocean. *J. Geophys. Res.*, **107.**3150, doi:1029/2000JC000719.

Zhang, Y., W. B. Rossow, A. A. Lacis, V. Oinas, and M. I. Mishchenko, 2004: Calculation of radiative fluxes from the surface to top of atmosphere based on ISCCP and other global data sets: Refinements of the radiative transfer model and the input data, *J. Geophys. Res.*, **109**, D19105, doi:10.1029/2003JD004457.

Zhou, L., R. Murtugudde, and M. Jochum, 2008: Dynamics of the intraseasonal oscillations in the Indian Ocean South Equatorial Current. *J. Phys. Oceanogr.*, **38**, 121–132.

Zhou, L., and R. Murtugudde, 2010: Influences of Madden-Julian Oscillations on the eastern Indian Ocean and the maritime continent. *Dyn. Atmos. Oceans,* **50**, 257-274.